Holistic approach to design a fuel cell hybrid system for maritime application

(Article begins on next page)

03 May 2024

Final dissertation

Holistic Approach to Design a Fuel Cell Hybrid System for Maritime Application

by
GIANMARCO SAPONARO

Referees:
Prof. Mauro VENTURINI
Prof. Cesare PIANESE

Supervisors:
Prof. Sergio Mario CAMPOREALE
Eng. Gianluca PISCOPO

Politecnico di Bari

Department of Mechanics, Mathematics and Management

Industry 4.0
Ph.D. Program

SSD: ING-IND/09 - Energy systems and power generation

Final dissertation

Holistic Approach to Design a Fuel Cell Hybrid System for Maritime Application

by
Gianmarco Saponaro

Referees:
Prof. Mauro Venturini
(University of Ferrara)
Prof. Cesare Pianese
(University of Salerno)

Supervisors:
Prof. Sergio Mario Camporeale
(Polytechnic University of Bari)

Eng. Gianluca Piscopo
(Isotta Fraschini Motori SpA)

Coordinator of the Ph.D. Program:
Prof.ssa Caterina Ciminelli

Politecnico
di Bari

LIBERATORIA PER L'ARCHIVIAZIONE DELLA TESI DI DOTTORATO

Al Magnifico Rettore
del Politecnico di Bari

Il sottoscritto Gianmarco Saponaro nato a Bari (BA) il 09/01/1992

residente a Bari (BA) in via Petraglione, 22 e-mail gxsaponaro@gmail.com

iscritto al 3° anno di Corso di Dottorato di Ricerca in Industria 4.0 ciclo 36°

ed essendo stato ammesso a sostenere l'esame finale con la prevista discussione della tesi dal titolo:

"Holistic Approach to Design a Fuel Cell Hybrid System for Maritime Application"

DICHIARA

1) di essere consapevole che, ai sensi del D.P.R. n. 445 del 28.12.2000, le dichiarazioni mendaci, la falsità negli atti e l'uso di atti falsi sono puniti ai sensi del codice penale e delle Leggi speciali in materia, e che nel caso ricorressero dette ipotesi, decade fin dall'inizio e senza necessità di nessuna formalità dai benefici conseguenti al provvedimento emanato sulla base di tali dichiarazioni;
2) di essere iscritto al Corso di Dottorato di ricerca Industria 4.0 ciclo 36°, corso attivato ai sensi del *"Regolamento dei Corsi di Dottorato di ricerca del Politecnico di Bari"*, emanato con D.R. n.286 del 01.07.2013;
3) di essere pienamente a conoscenza delle disposizioni contenute nel predetto Regolamento in merito alla procedura di deposito, pubblicazione e autoarchiviazione della tesi di dottorato nell'Archivio Istituzionale ad accesso aperto alla letteratura scientifica;
4) di essere consapevole che attraverso l'autoarchiviazione delle tesi nell'Archivio Istituzionale ad accesso aperto alla letteratura scientifica del Politecnico di Bari (IRIS-POLIBA), l'Ateneo archivierà e renderà consultabile in rete (nel rispetto della Policy di Ateneo di cui al D.R. 642 del 13.11.2015) il testo completo della tesi di dottorato, fatta salva la possibilità di sottoscrizione di apposite licenze per le relative condizioni di utilizzo (di cui al sito http://www.creativecommons.it/Licenze), e fatte salve, altresì, le eventuali esigenze di "embargo", legate a strette considerazioni sulla tutelabilità e sfruttamento industriale/commerciale dei contenuti della tesi, da rappresentarsi mediante compilazione e sottoscrizione del modulo in calce (Richiesta di embargo);
5) che la tesi da depositare in IRIS-POLIBA, in formato digitale (PDF/A) sarà del tutto identica a quelle consegnate/inviate/da inviarsi ai componenti della commissione per l'esame finale e a qualsiasi altra copia depositata presso gli Uffici del Politecnico di Bari in forma cartacea o digitale, ovvero a quella da discutere in sede di esame finale, a quella da depositare, a cura dell'Ateneo, presso le Biblioteche Nazionali Centrali di Roma e Firenze e presso tutti gli Uffici competenti per legge al momento del deposito stesso, e che di conseguenza va esclusa qualsiasi responsabilità del Politecnico di Bari per quanto riguarda eventuali errori, imprecisioni o omissioni nei contenuti della tesi;
6) che il contenuto e l'organizzazione della tesi è opera originale realizzata dal sottoscritto e non compromette in alcun modo i diritti di terzi, ivi compresi quelli relativi alla sicurezza dei dati personali; che pertanto il Politecnico di Bari ed i suoi funzionari sono in ogni caso esenti da responsabilità di qualsivoglia natura: civile, amministrativa e penale e saranno dal sottoscritto tenuti indenni da qualsiasi richiesta o rivendicazione da parte di terzi;
7) che il contenuto della tesi non infrange in alcun modo il diritto d'Autore né gli obblighi connessi alla salvaguardia di diritti morali od economici di altri autori o di altri aventi diritto, sia per testi, immagini, foto, tabelle, o altre parti di cui la tesi è composta.

Bari 23/12/2023   Firma _____

Il/La sottoscritto, con l'autoarchiviazione della propria tesi di dottorato nell'Archivio Istituzionale ad accesso aperto del Politecnico di Bari (POLIBA-IRIS), pur mantenendo su di essa tutti i diritti d'autore, morali ed economici, ai sensi della normativa vigente (Legge 633/1941 e ss.mm.ii.),

CONCEDE

- al Politecnico di Bari il permesso di trasferire l'opera su qualsiasi supporto e di convertirla in qualsiasi formato al fine di una corretta conservazione nel tempo. Il Politecnico di Bari garantisce che non verrà effettuata alcuna modifica al contenuto e alla struttura dell'opera.
- al Politecnico di Bari la possibilità di riprodurre l'opera in più di una copia per fini di sicurezza, back-up e conservazione.

Bari 23/12/2023   Firma _____

In addition, the PhD student participated in several significant company projects in the field of ship propulsion. In particular, he contributed significantly to the development of hybrid propulsion system configurations based on the use of internal combustion engines and fuel cells at Isotta Fraschini Motori S.p.A., promoting advanced and sustainable solutions for the maritime industry.

Isotta Fraschini MOTORI | Politecnico di Bari | Dipartimento Meccanica Matematica Management | MIUR Dipartimento di Eccellenza 2018-2022 2023-2027

Sommario

La tesi presenta la progettazione olistica di un sistema generazione di potenza e propulsione di un sistema ibrido a bordo di traghetti basato su una cella a combustibile a membrana a scambio protonico (PEMFC). Nello scenario di transizione energetica a zero emissioni di carbonio, la tecnologia delle celle a combustibile a idrogeno (FC) è protagonista per i sistemi di alimentazione stazionari e per il trasporto elettrico a medio e lungo raggio. Nelle applicazioni marine, soprattutto per le imbarcazioni che operano nelle zone costiere, le PEMFC rappresentano una solida alternativa alle batterie, in quanto possono fornire una maggiore densità energetica grazie alla separazione tra la PEMFC e l'accumulo di energia (serbatoio di H_2). Attualmente, la penetrazione di questa tecnologia nei sistemi di alimentazione marina è limitata dai costi di produzione delle celle a combustibile e dall'elevata purezza dell'idrogeno come combustibile. Inoltre, le aziende che offrono soluzioni di generazione di energia basate su PEMFC al mercato marino devono progettare il prodotto per soddisfare i requisiti del cliente, che sono diversi per ogni applicazione. Ciò aumenta significativamente i costi e le risorse coinvolte in ogni progetto.

L'obiettivo di questo lavoro è fornire uno strumento efficace per la progettazione preliminare di sistemi PEMFC che consideri la cella a combustibile in una configurazione ibrida, tenendo conto dell'interazione con tutte le altre apparecchiature a bordo. L'approccio olistico, insieme al dimensionamento del sistema FC, fornisce importanti indicazioni per il dimensionamento degli altri componenti del sistema di potenza.

Il framework di simulazione, sviluppato in ambiente Matlab-Simulink, utilizza modelli di diversa complessità per ogni componente del sistema nave, tenendo conto del grado di interazione con la PEMFC. Così, le altre fonti di energia, come le batterie e i motori a combustione interna, sono modellate tenendo conto della dinamica di questi sistemi e dell'efficienza dei convertitori utilizzati per distribuire l'energia alla rete elettrica. Il sistema di gestione dell'energia (EMS) proposto seleziona la modalità operativa, tenendo conto della potenza richiesta dalla nave e della capacità residua della batteria, e scegliendo come utilizzare l'energia disponibile al porto.

La modellazione comprende non solo i sistemi di alimentazione ma anche tutte le caratteristiche della nave, dalla resistenza dello scafo alla potenza dell'elica. Questo è proosto nel caso di un progetto di una nuova nave, per conoscere la potenza necessaria

durante il funzionamento.

Le simulazioni valutano la fattibilità del sistema di alimentazione ibrido PEMFC, tenendo conto delle principali criticità riportate nella letteratura scientifica, come le prestazioni transitorie, il degrado della FC e la gestione termica. Il framework di ottimizzazione trova quindi la soluzione per ottenere le migliori prestazioni in termini di degrado della FC nell'arco di un anno di funzionamento della nave.

Il caso di studio scelto è un traghetto esistente che attualmente è alimentato principalmente da batterie e generatori diesel in una rete DC. I risultati proposti della configurazione del sistema di alimentazione a zero emissioni, basato sulla PEMFC e sulla batteria, mostrano le prestazioni dell'intero sistema durante 5100 ore di funzionamento e, in particolare, l'efficienza della PEMFC e della strategia di gestione termica applicata.

Abstract

This thesis presents the holistic design of a hybrid power system and propulsion system for ferry applications based on a Proton Exchange Membrane Fuel Cell (PEMFC). In the zero carbon energy transition scenario, hydrogen fuel cell (FC) technology is the protagonist for stationary power systems and medium to long range electric transport. In marine applications, especially for vessels operating in coastal areas, PEMFCs are a solid alternative to batteries, as they can provide a higher energy density due to the separation between the PEMFC and the energy storage (H_2 tank). At present, the penetration of this technology into marine power systems is limited by the cost of manufacturing fuel cells and the high purity of hydrogen as a fuel. In addition, companies offering PEMFC-based power generation solutions to the marine market must design the product to meet customer requirements, which are different for each application. This significantly increases the cost and resources involved in each project.

The aim of this work is to provide an effective tool for the preliminary design of PEMFC systems that considers the fuel cell in a hybrid configuration, taking into account the interaction with all other equipment on board. The holistic approach, together with the sizing of the FC system, provides important insights into the sizing of the other power system components.

The simulation framework, developed in the Matlab-Simulink environment, uses models of different complexity for each power system component, taking into account the degree of interaction with the PEMFC. Thus, the other energy sources, such as batteries and internal combustion engines, are modelled taking into account the dynamics of these systems and the efficiency of the converters used to distribute the energy to the electrical grid. The proposed on-line energy management system (EMS) selects the operating mode, taking into account the ship's power requirements and the remaining battery capacity, and chooses how to use the power available on shore.

The modelling included not only the power systems but also all the ship's characteristics, from hull resistance to propeller power. This was done in the case of a new ship design to know the power required during operation.

The simulations assess the feasibility of the hybrid PEMFC power system, taking into account the main criticalities reported in the scientific literature, such as transient performance, FC degradation and thermal management. The optimisation framework

then finds the solution to achieve the best performance in terms of FC stack degradation over one year of ship operation.

The chosen case study is an existing ferry that is currently powered mainly by batteries and diesel generators in an DC network. The proposed results of the zero-emission power system configuration, based on the PEMFC and the battery, show the performance of the whole system during 5100 operating hours, and in particular, the efficiency of the PEMFC and of the applied thermal management strategy.

Contents

List of Figures

List of Tables

List of Symbols

Acronyms

AC	Alternate Current	
BEV	Battery Electric Vehicles	
DC	Direct Current	
DEG	Diesel Engine Generator	
DP	Dynamic Positioning	
EEDI	Energy Efficiency Design Index	
EM	Electric Motor	
EMS	Energy Management System	
FC	Fuel Cell	
FCEV	Fuel Cell Electric Vehicle	
FCHV	Fuel Cell Hybrid Vehicle	
FSDEG	Fixed Speed Diesel Engine Generator	
GDL	Gas Diffusion Layer	
GHG	Green House Gases	
ICE	Internal Combustion Engine	
IMO	International Maritime Organization	
LHV	Lower Heating Value	J/g
MARPOL	International Convention for the Prevention of Pollution from Ships	
MEA	Membrane Electrode Assembly	
MEPC	Marine Environment Protection Committee	
MVAC	Medium Voltage Alternate Current	
DC	Direct Current	
OPRC	Oil Pollution Preparedness, Response and Cooperation	
PEM	Proton Exchange Membrane	
PEMFC	Proton Exchange Membrane Fuel Cell	
PMS	Power Management System	
RES	Renewable Energy Sources	
RPM	Rotation Per Minute	
SFC	Specific Fuel Consumption	g/kWh

SFOC	Specific Fuel Oil Consumption	g/kWh
SOFC	Solid Oxide Fuel Cell	
VSDEG	Variable Speed Diesel Engine Generator	
YSZ	Yttria-Stabilized Zirconia	
ZES	Zero Emissions Ship	

Chapter 1

Introduction

1.1 Motivations

Human activities, mainly through emissions of greenhouse gases (GHG), unequivocally caused global warming. For instance, the global average surface temperature measured in the last decade reached $1.1°C$ above the level of the period 1850-1900. Fig. 1.1 shows the increase in GHG concentrations since around 1750 are clearly caused by GHG emissions from human activities. Land and ocean sinks take up a near-constant proportion, globally about 56% per year, of CO_2 emissions from human activities over the past six decades [1].

The energy transition, characterized by a shift from fossil fuels to renewable energy sources, plays a pivotal role in mitigating the effects of climate change and offers a sustainable solution to global warming; it is imperative that all industrial sectors actively participate in this transition to ensure comprehensive and lasting environmental benefits.
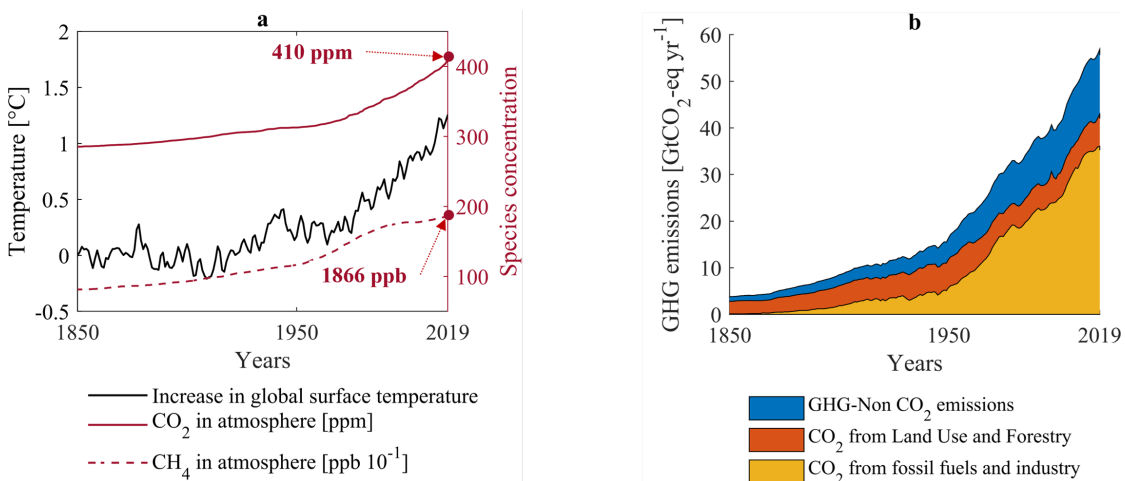
Figure 1.1: **a** - Increase in global surface temperature with the raising trend of GHG emissions as CO_2 and CH_4; **b** - GHG global emissions related to human activities from 1850 to 2019 [1].

Climate change impacts will vary significantly across different regions. Small island states and least-developed countries are especially vulnerable to the effects of climate change and may struggle to handle the impacts of a world that is 2 $^{\circ}C$ warmer than preindustrial levels [2]. This concern led to the Alliance of Small Island States proposing a goal, which was subsequently adopted in the Paris Agreement of 2015 by 196 countries. The agreement aims to keep the rise in global average temperature well below $2^{\circ}C$ above preindustrial levels and to make efforts to limit the increase to $1.5^{\circ}C$ [3]. To adhere to the $1.5^{\circ}C$ limit, profound changes in the economy and energy use and supply will be necessary, including a swift transition to net zero carbon emissions globally, as outlined by Rogelj et al. in 2015 [4].

1.1.1 The Energy Transition in The Maritime Transport Sector

The maritime transport sector is a significant component of the global economy, accounting for almost 90% in volume of worldwide goods transportation [5]. Even though maritime transportation stands as one of the most emission-efficient methods of freight transportation per ton-kilometer, it contributes to GHG emissions per year with approximately 2.9% of total anthropogenic carbon dioxide (CO_2), 11% of sulfur oxides (SO_x), and 15% of nitrogen oxides (NO_x) [6]. The development of global trade and shipping industry means the increase year by year of fuel consumption in global shipping. Hence, projections suggest that by 2050 the shipping industry could contribute to 12-18% of the world human-caused GHG emissions [7].

The energy transition in the maritime transport sector involves the implementation of hybrid and electric power systems and propulsion in ships, the use of on-shore power, and the electrification of sea ports. These actions aim to reduce the carbon footprint of the entire transshipment service and develop a cleaner and more energy-efficient maritime transport sector [8]. The electrification of ships and ports presents new challenges and opportunities for the maritime business, particularly in the context of open electric energy markets. The transition towards 100% renewable energy and zero greenhouse gas emissions in the transport sector is technically feasible and economically viable, with direct and indirect electrification playing a key role, along with the production of new fuels. Ports play a crucial role in enabling the supply of sustainable electrical energy to green ships through shore connection systems, local renewables, and energy storage systems. The cost and emissions efficiency of substituting conventional gasoline-based vehicles with new energy vehicles in the transport sector depends on factors such as electricity mix scenarios and government subsidy policies [9].

1.1.2 The International Maritime Organization Net-Zero Emissions Roadmap

The International Maritime Organization (IMO) is a specialized agency within the United Nations that regulates maritime transport and is responsible for the safety, security, and prevention of marine pollution by ships. It plays a crucial role in the decarbonization of the maritime industry and reducing greenhouse gas emissions from international shipping.

The IMO has been at the forefront of addressing environmental concerns related to the maritime industry. Recognizing the significant impact of shipping on the environment, the IMO has adopted various measures to curb pollution from ships. One of the landmark conventions is the International Convention for the Prevention of Pollution from Ships (MARPOL), which was introduced in 1973. Over the years, MARPOL has been amended to address not just oil pollution but also pollution from chemicals, harmful substances, garbage, sewage, and notably, air pollution and emissions from ships. Annex VI of MARPOL, adopted in 1997 (mandatory since 2011), specifically targets air pollution and emissions. The IMO also implemented the International Convention on Oil Pollution Preparedness, Response and Cooperation (OPRC). During the 70th Meeting of the Marine Environment Protection Committee (MEPC), a roadmap for a comprehensive IMO strategy on GHG reduction from ships was approved. This roadmap, depicted in Fig. 1.2, includes short-term, mid-term, and long-term measures, with the strategy set to be adopted by 2023 [10].

IMO strategy towards decarbonizing defines three distinct stages. The targets include two main milestones: firstly, to cut the average carbon emissions by 40% by the 2030, and secondly, to achieve a 70% reduction by 2050, both compared to the baseline year of 2008. An immediate step to achieve short-term benefits is to lower the carbon footprint of the maritime sector. This effort has been initiated by launching the Energy Efficiency Design Index (EEDI) for new vessels and ship speed reduction as an easy preliminary measure.

1.1.3 The Ferry Industry Sector and Challenges

The ferry industry plays a important part in the global transportation landscape, bridging the gap between islands and mainlands, urban and rural areas, and even between different countries. As an indispensable mode of transport, ferries cater to both passengers and vehicles, offering a combination of convenience, economy, and accessibility. In 2019, it has been estimated that the global ferry industry alone transports more than 4.3 billion passengers per year [12].

Norway is the largest ferry nation in Europe, with 180 ferries operating 112 routes. The country has taken a world-leading position in electric and hybrid car ferries, with plans to have more than 70 fully or hybrid electric ferries by 2022. Ferries play a crucial
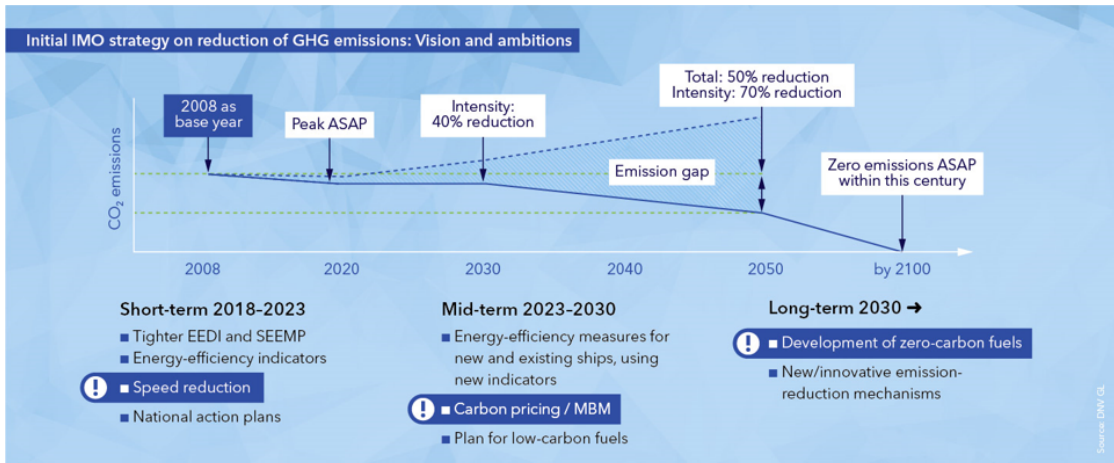
Figure 1.2: The initial IMO strategy on the reduction of GHG emissions from [11]

role in the Norwegian road transport system, connecting communities on islands along the coast. Italy also relies heavily on ferries due to its coastline and numerous islands. The Italian ferry fleet is the second largest in Europe, behind Norway. Electrification of ferries in Italy, along with Greece, Germany, and the UK, has the potential to reduce emissions by up to 800,000 tons of CO_2, corresponding to a 50% decrease in ferry-related emissions in these countries [13].

Nearly 70% of global GHG emissions occur within 400 km of coastlines, which has a potential influence on air quality in coastal areas [14] where it is estimated that about 40% of the world population lives within 100 km of the coastline [15]. There is a necessity to cut down emissions from ships, especially those that operate in coastal waters.

In this scenario, according to the EU-MRV classification, the mandatory monitoring, reporting and verification system established by the European Commission, passenger transport ferries belong to the category of Ro-pax ships. In 2020, this category of transports was responsible for 9.3% of CO_2 emissions from European maritime transport, but, compared to 2019, the carbon dioxide emitted by Ro-pax was reduced by 21%, equivalent to roughly $3x10^9$ kg of CO_2 saved [16]. The fast drop in ferry emissions reflects the significant impact of new power generation technologies on this sector.

To better exploit the energy transition in ferry transports, full-electric vessels should be encouraged to replace older vessels on all routes up to one-hour (long-haul). In addition, the ferry fleet in Europe is on average 35 years old, with 65% of the vessels more than 20 years old, as illustrated in Tab.1.1. This means that more than half of the fleet will be subject to replacement during the current decade [13]. Thus, in order to face legislative constraints, the maritime industry will have to come up with various zero emissions solutions for new ferries and to refit the existing ones.

The electrification of ferries using available technologies such as shore power, hybridization, and electric propulsion for routes of up to one hour can significantly con-

Table 1.1: Age of the European ferry fleet from Siemens 2022 report [13]

Average age of European ferry fleet	35 years
Share of fleet older than 20 years	64.59%
Share of fleet older than 30 years	44.70%
Share of fleet older than 40 years	25.46%

tribute to reducing emissions in the ferry industry [13].

1.2 Objectives

This work aims to create a comprehensive preliminary design tool for proton exchange membrane fuel cell (PEMFC) systems in hybrid ship configurations. It includes the interactions of the fuel cell with other on-board equipment, taking a holistic approach to evaluate not only the fuel cell system but also the other components of the power system.

A simulation platform was developed in Matlab-Simulink to model various elements of the power plant, each with a complexity that reflects its interaction with the PEMFC. This includes modeling additional power sources such as batteries and internal combustion engines, taking into account the dynamic behavior of these systems and the efficiency of the converters that distribute power to the electrical grid. A rule-based online energy management system (EMS) was introduced to dynamically select operating modes, based on the ship's power demand and battery status, and to manage the distribution of available shore power.

The scope of modeling extends to the full range of ship characteristics, including hull strength and propeller power requirements, which is particularly useful in the context of new ship design to estimate operational power requirements.

The simulations assess the feasibility of the PEMFC hybrid power system, considering key challenges identified in scientific research, such as transient responses, fuel cell degradation, and thermal management. The optimization component of the framework seeks to minimize the degradation of the fuel cell stack, with the goal of achieving optimal performance for one year of ship operation.

PEMFCs are a very expensive technology that currently bases its long-term operation on the use of rare materials such as Platinum. Limiting cell degradation means making the best use of the important resources used. Therefore through this work a study, based on experimental datasets, of fuel cell degradation in the context of coastal vessels is proposed.

1.3   Thesis Structure

The thesis is organized in seven chapters, as follows:

- **Chapter 1** introduces the research theme project with its motivations and objectives;

- **Chapter 2** describes the evolution of ship powertrains and related challenges. It introduce the role of PEM Fuel Cell technology in the maritime industry and reviews the technical literature about numerical and experimental investigations;

- **Chapter 3** characterizes the fuel cell technology from an electro-chemical and thermodynamic points of view;

- **Chapter 4** gives an overview about the holistic approach to the preliminary design and presents the proposed methodology;

- **Chapter 5** illustrates the proposed model for the PEM Fuel Cell system and its calibration and validation. Moreover, it reports the modelling methodology exploited to implement the energy storage and the variable speed diesel engine generator. Finally, the proposed online energy management strategy, for PEMFC and related energy storage, is depicted;

- **Chapter 6** describes the real case study and the mission profile, presents the optimization framework and the results of the simulation campaign about the feasibility of the proposed power system for the case study application;

- **Chapter 7** summarizes the conclusions of the thesis and recommendations for future works.

Chapter 2

Background

Ship design has traditionally been a slow and conservative process. Since the 1950's the design procedure relays on the "ship design spiral", Fig. 2.1, presented by J.H. Evans in 1959 and still mentioned in many currently used literature [17]. However, there have been criticisms of its effectiveness and accuracy. One criticism is that it assumes a relatively smooth process toward a balanced solution, which may not always be true in the ship design process, which is often iterative and involves requirements from different contexts.
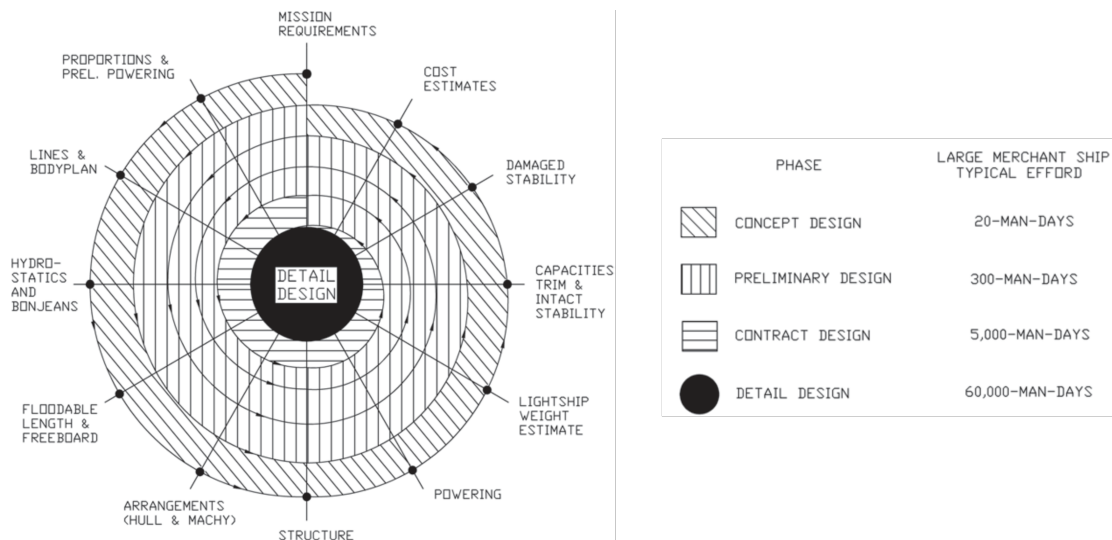
Figure 2.1: The Design spiral, J.H. Evans 1959 [17]

The introduction of digital modelling and optimization concepts and methodologies is enabling more intelligent and efficient ship and power system design processes. These methods aim to achieve predictive evaluations with improved performance and increased efficiency, while reducing user dependency. Additionally, the shipbuilding industry is experiencing a wave of new technologies, driven by factors such as acoustic quietness, multi-mission requirements, safety, and fuel costs.

In this work, the design of the whole ship is not presented, but the integration of PEMFC as the main power source. By analyzing the preliminary design stage the "Powering" section of the ship design spiral. To introduce the fuel cell on board, it is necessary to know the hotel load and propulsive load requirements of the vessel. Hence, to know which power source would provide for which loads in the evolution of naval powertrains. To ensure more efficient fuel cell and battery sizing.

2.1   The Evolution of Ship Powertrains

This section describes the main layouts used in the shipbuilding industry and future trends. The powertrain of any ship consists of three systems, which perform different functions but are strongly interconnected. The propulsive layout includes the engine, which provides mechanical work to the drivetrain; the gearbox, which acts as a mechanical coupling between the drive shaft and the propeller shaft; and the propeller, which uses the input power to provide the thrust required for the motion of the vessel. The power generation system converts the chemical energy from the fuel on board into electrical energy. Finally, the energy storage system includes all those storing technologies installed on board. These can be used to meet peak power demand and store the excess power produced or to be a primary energy source for the ship.

Fig. 2.2 shows the main technologies exploited in each section of the vessel powertrain. The automotive reference powertrain classification uses the definitions of: mechanical propulsion, full electric propulsion, series hybrid (electric coupling), parallel hybrid (mechanical coupling). Employing this nomenclature in the marine industry could cause misunderstandings or mistakes. In contrast, using the proposed classification it is possible to define any layout from the mix of technologies used for the three macro-systems, depicted in Fig. 2.2: propulsion, power generation, energy storage.

The different configurations discussed below are all solutions available for future ships, thanks to the development of zero or ultra-low emission technologies. The use of new low-carbon fuels and the continually increasing research into the efficiency of combustion systems are key to renewing the use of internal combustion engines and turbogas plants in the machinery of vessels [18] [19].

Conventional Propulsion

The mechanical or conventional propulsion system on ships is arranged according to the typical architecture as shown in Fig. 2.3. The propulsion architecture consists of gas turbines or diesel engines, which are prime mover. The torque generated is driven to the propeller directly through the shaft line or indirectly through the gearbox. On large merchant ships and marine vessels, propellers are usually driven directly by low-speed two-stroke diesel engines with engine speed in the range of (100-170 RPM). On the
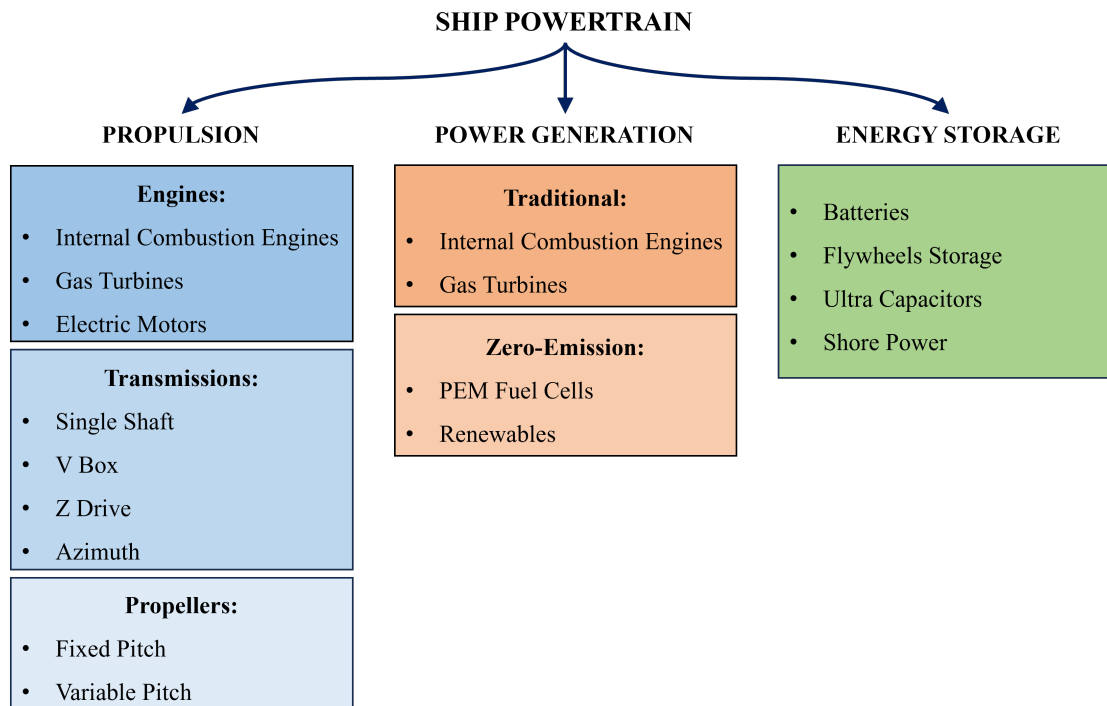
Figure 2.2: Classification of powertrain technologies for ships based on functions

other hand, on smaller ships, the speed is reduced according to the ratios of gearbox because these ships are usually equipped by high-speed or medium-speed four-stroke diesel engines.

The power generation system is arranged as shown in Fig. 2.3. In particular, diesel engines or gas turbines generators supply the electricity to the microgrid onboard. Then, the AC network has the function of generating and distributing electricity to the hotel loads, such as pump and fan motors, drying and ventilation systems, control and communication devices.

As reported by Karakitsos and Theotokatos in 2016 [20] study around the 95% of marine vessels are equipped with diesel engines, serving as both their main and auxiliary power sources. Mechanical propulsion architecture is a valid option for fixed-route freighters or fast-service seafarers due to the benefits of full-load fuel consumption [21]. Additionally, there are applications like tug boats that require the ICE propulsion due to the high torque demanded in bollard pull conditions.

Electric Propulsion

The architecture of an electric propulsion system is shown in Fig. 2.4. The generator set, that could include ICEs or gas turbines, is used to supply and distribute the electricity to the AC ship electric grid. After that, the electric grid powers electric propulsion motor and hotel loads loads.
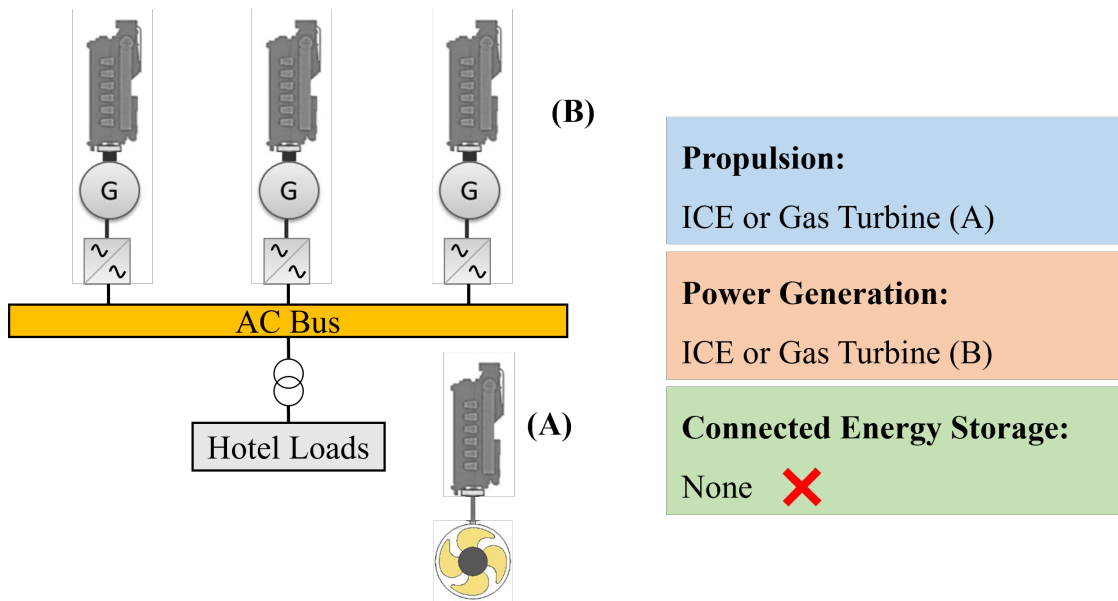
Figure 2.3: Conventional ship propulsion architecture
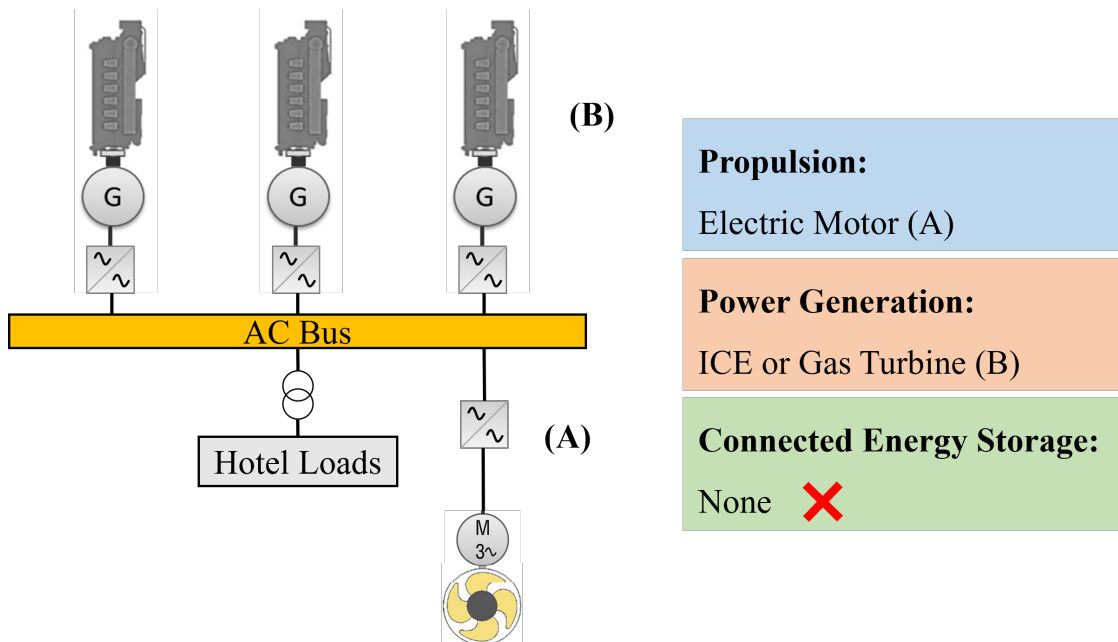
Figure 2.4: Typical Electric Propulsion system layout

Electric propulsion is a fuel-efficient propulsion solution when the hotel load is a significant fraction of the propulsion power requirement and the operating profile is is not predictable, because the generator power, used for both propulsion and auxiliary systems, is obtained optimizing the demand in order to run the engines at low consumption operating point. To achieve this, a power management system (PMS) matches the amount of running engines with the required combined propulsion and hotel load power, this control strategy ensures engines do not run inefficiently in partial loads.

Comparing with conventional one, electric propulsion has reduced maintenance cost, as engines are switched off when they are not required. This selection can reduce the radiated noise emitted from the power generation system. To this aim, the design of motor and power converter has to be optimised for minimal torque fluctuation.

Electrical propulsion, while promising in many aspects, does face a set of challenges. One of the primary concerns is the increased losses attributed to the extra conversion stages present in power converters and electric motors. These losses subsequently cause a rise in the Specific Fuel Consumption (SFC), which is especially noticeable when the ship is operating near its top speed. Moreover, in scenarios where high power is required by propulsion, such as sensitive Dynamic Positioning (DP) operations, it's common to run redundant engines. However, these engines often operate at partial load, which results in inefficient fuel consumption and fault risk [22]. Additionally, all onboard loads are subjected to the electrical network voltage and frequency. This means that any swings in voltage or frequency, particularly under fault conditions, can compromise the system reliability and availability by causing systems to shut off. This vulnerability is especially pronounced in power systems that heavily rely on variable speed drives. Sulligoi [23] proposed a description of the phenomena and methods to analyse the risk with two modelling strategies.

Hybrid Propulsion

The typical hybrid propulsion system, as shown in Fig. 2.5, consist of ICE or gas turbine as power generation system connected to the AC shipboard. The electrical grid supplies the hotel loads the propulsive electric motor (EM). The ICE in parallel hybrid configuration with the EM (mechanical coupling) provides the torque to the propeller.

Electric drives used in ship propulsion have brought in addition to their high efficiency, further benefits such as the possibility of designing more sophisticated and flexible propulsion systems between different applications. Thus, the installation of an internal combustion engine in the propulsive plant is limited to applications where is demanded a huge amount of torque. Hybrid propulsion systems are considered optimal for ships operating in separate modes for a considerable period. This architecture was used on offshore ships, as a valid propulsive solution for the dynamic positioning during platform operations, tug boats, during bollard pull operations, and military vessels.
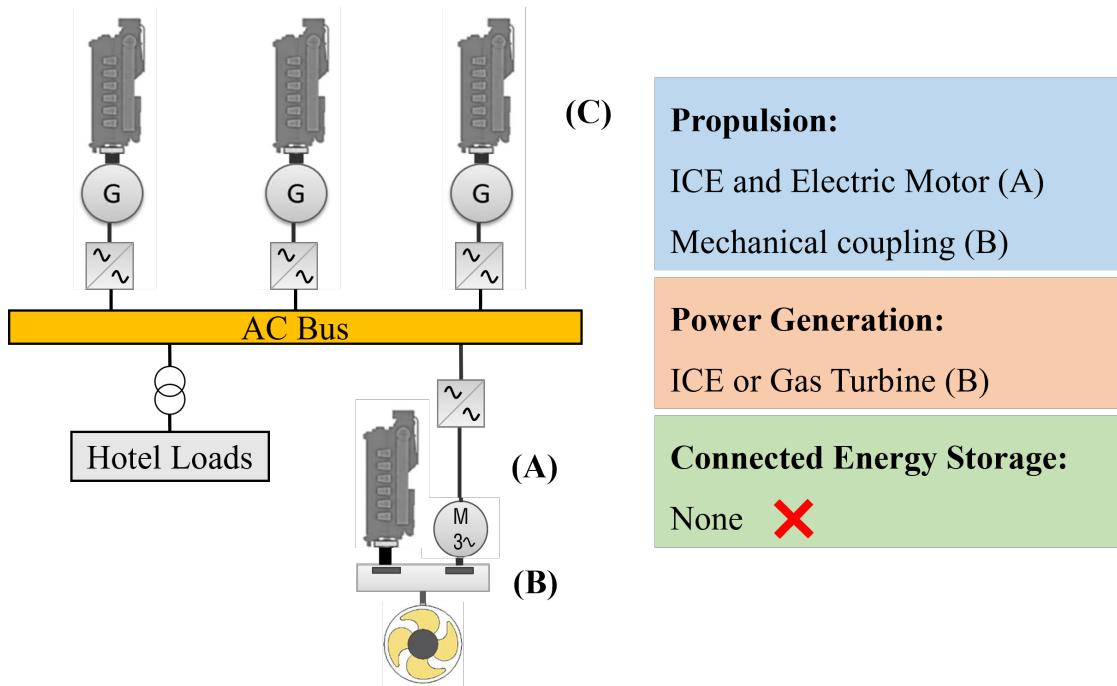
Figure 2.5: Architecture of hybrid propulsion system

When an electric drive operates in parallel with a mechanical drive, it can help boost the ship's maximum speed and lower the engine's heat stress, leading to reduced NO_x emissions. Topaloglou et al. [24] introduced a control approach that adjusts the electric motor's torque to decrease the main engine's air excess ratio. This ratio represents the available air in the engine cylinder during combustion, serving as an indicator of engine heat stress. The suggested method adjusts the electric drive's torque to keep the desired value, determined by a fixed map based on engine torque, speed, and charge pressure. In acceleration tests at the National University of Athens, this approach resulted in a 16% drop in NO_x emissions and increased the minimum air excess ratio from 1.85 to 2.15, indicating a substantial reduction in engine heat stress during acceleration. This method highlights the enhanced performance achievable when the electric drive operates concurrently with the main diesel engine.

The electric motor works as a shaft generator if the primary engine has enough load capacity. For instance, the propulsion system of the FREEM frigate of the Italian Navy consists of a gas turbine. This design allows the engine to provide maximum power at any shaft speed. Therefore, sufficient load margin is always available, unless the ship is sailing at top speed in off-design conditions. Given this setup, using the electric motor as a shaft generator is a practical choice for this configuration proposed by Sulligoi in [25].

Electric Propulsion with Energy Storage

The ship electric propulsion system with an energy storage system connected to the shipboard is one of the most exploited powertrain layout, for current ships, thanks to the reliability of the combustion system associated with the energy storage, usually batteries, capability and the option to recharging in ports in cold ironing mode. The simple scheme is showed in Fig. 2.6.
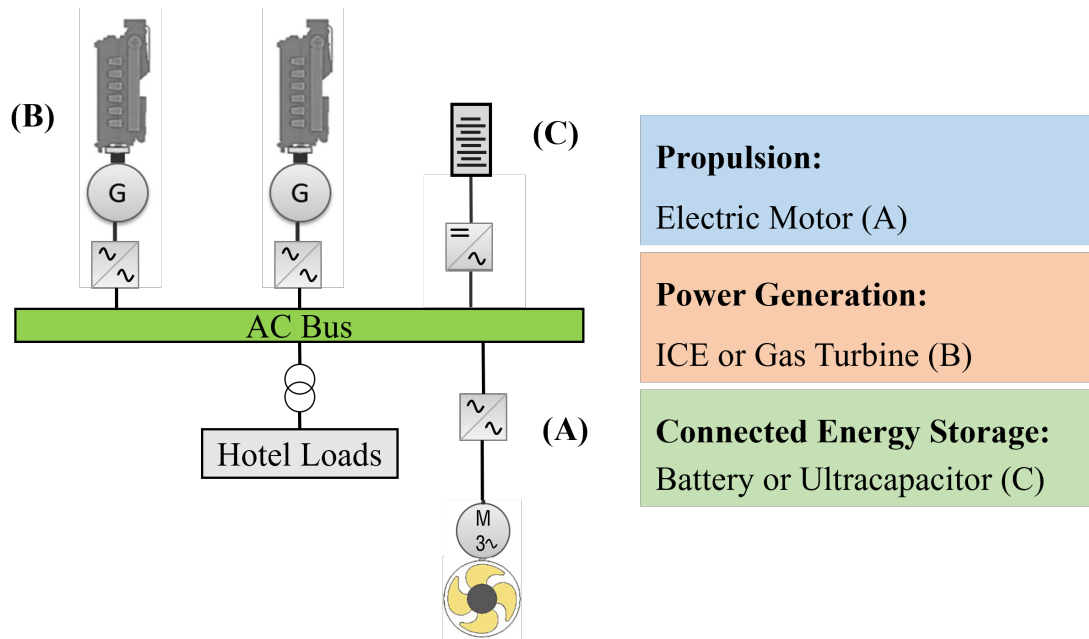
Figure 2.6: Electric Propulsion layout with connected Energy Storage System (ESS)

Although batteries were applied later than technologies with electric propulsion systems on ships, their popularity has spread widely. The battery-stored power allows the main ICE generators to work at high efficient conditions and may even allow engine shutdown, especially under low load operations [26]. At the same time, the energy storage can be charged when the engines are operating at rated power with lower fuel consumption and CO_2 and NO_x emissions [27]. This approach brings multiple benefits, such as better fuel efficiency, lower noise and vibrations, reduced emissions, and enhanced comfort. It also allows ships to operate temporarily without the typical disturbances from engines, like emissions, noise, and vibrations, as highlighted by [28] and [29].

Dedes et al. [30] proposed an electric propulsion with battery energy storage for bulk carriers can save 2% to 3% of the fuel and reduce 5% to 7% of CO_2 and NO_x emissions, compared with the performance without battery. This is thanks to the load balancing capability of the battery power reserve, they can be charged from other power sources, contributing to reduce fuel consumption and local emissions.

Moreover, batteries can provide backup power during breakdowns of diesel generators. As a result, faulty diesel engines may be absent, resulting in a reduction in the

number of diesel engines that must be fitted to the vessel [31]. Lastly, Wang et al. [32] confirm the economic advantages that electric propulsion systems with energy storage best suit tugs and ferries. Those studies are all about storing battery power with control rules [33]. If the batteries aren't charged from land-based grids, then the fuel efficiency of the hybrid propulsion system is assessed. However, it's essential to note that the outcomes of such research largely hinge on the ship's operational history.

There are more than 2000 ports in the world, and 80% of global trade is carried out through port transportation. The improvement of the energy structure during docking can greatly improve the port environment and reduce the pollution caused by ships. During docking at the port, the power required by ships is around 2-5 MW, without considering cruise vessels. It is fundamental to favor the green transition that ports offers not only refuelling service but the capability to power the docked ships with clean energy sources, such as renewables (RES) and hydrogen stationary fuel cells. Although the operation is simple and the work is stable, it is still not environmentally friendly, which does not fundamentally change the pressure on the environment caused by the ship when it is docked [34].

Electrical Propulsion with DC Hybrid Power Supply

Energy saving, high efficiency, low emission, and low noise are the main characteristics required for the next generation of power systems for ships. Therefore, in accordance with countries' strategies to reduce pollutant emissions, the penetration of renewable energies and carbon-free technologies installed on vessels has increased in recent years. In addition, because all of these solutions produce direct current (DC) electricity, their development has moved in parallel with the study of DC grids on board of ships. Hybrid power system ships are undergoing a transition from an alternating current (AC) network to a medium and high voltage direct current (DC) network [35]. According to guidelines published by the Institute of Electrical and Electronics Engineers (IEEE), the ship system with a DC bus voltage between 1 and $35kV$ is defined as a medium-voltage DC system (MVDC) [36].

Submarines pioneered the application of DC systems to electric propulsion system architecture. However, barriers to fault protection and electrical system stability have limited its scope of application. The problem was solved until power electronic technologies and intelligent circuit diagrams protecting against incidents were introduced [37].

DC grids compared with the AC have the following advantages [22] [38] [39]:

- Efficient system integration, eliminating the need to distribute power in switchboards and transformers, as well as reducing the size and weight of a power system;

- Remove the frequency constraint to adjust the connection between the generator and the load motor, so that a diesel generator can operate on the optimal energy

consumption curve;

- No transmission of reactive power, and a decrease of cable weight;

- A DC network has a superior technical compatibility, facilitating access to various energy sources, and significantly improving system selectivity, power supply continuity, and economy;

- compared with electromagnetic relays, a DC grid exploits power electronic devices for security protection, which can provide better fault isolation and facilitate a system maintenance.

The main challenge for MVDC grids on ships is the lack of standardized equipment and system-level stability [40]. MVDC distribution networks are still not as mature as MVAC distribution systems when it comes to fault detection and isolation [41]. To ensure the reliability of shipboard microgrids, protection systems need to provide selectivity in fault detection, location, and isolation [42]. Different existing fault detection, location, and isolation schemes, from traditional to modern techniques, are being compared to highlight their advantages and disadvantages [43].

Fig. 2.7 shows the simple scheme of electrical propulsion with DC hybrid power supply architecture. The diesel engine generator (DEG) power is transferred to the DC bus after an AC/DC. To play the role of peak shaving and renge extender, the storage battery unit, or supercapacitor, is connected to the DC bus through a two-way DC/DC. Fuel cells and renewables are respectively imported into the DC bus after boosting through a one-way DC/DC [7]. The DC bus unifies the collected electrical energy of the same voltage into AC by a DC/AC inverter to drive the propulsion motor and supply electricity.

In recent years, an interest in variable speed drives as generation units has grown for some commercial boats to achieve a better exploitation of hybrid plants (DEGs with RES and storage system) using Variable Speed Diesel Engine Generators (VSDEG) connected to a DC-grid [44]. In this way, the limit of working at the fixed frequency of the AC grid is overcome allowing to optimize the engine operating point according to the required load by adjusting its speed [45] [46]. It results in different considerable advantages over Fixed Speed DEGs (FSDEGs): fuel saving (around 20% on average depending on the load profile [47]); pollutant and noise emissions reduction [48] [49]; maintenance costs reduction and engine life extension (increased time between overhauls by up to 20% [50]);

The development of control strategies and grid stability techniques allowed further evolution of the ship's powertrain layout, achieving further levels in system flexibility, customization and efficiency reducing GHG emissions. Fig. 2.8 shows the series-parallel hybrid electric propulsion with DC hybrid power supply, basically a hybrid propulsion with all the already mentioned DC grid benefits where is implemented a waste energy
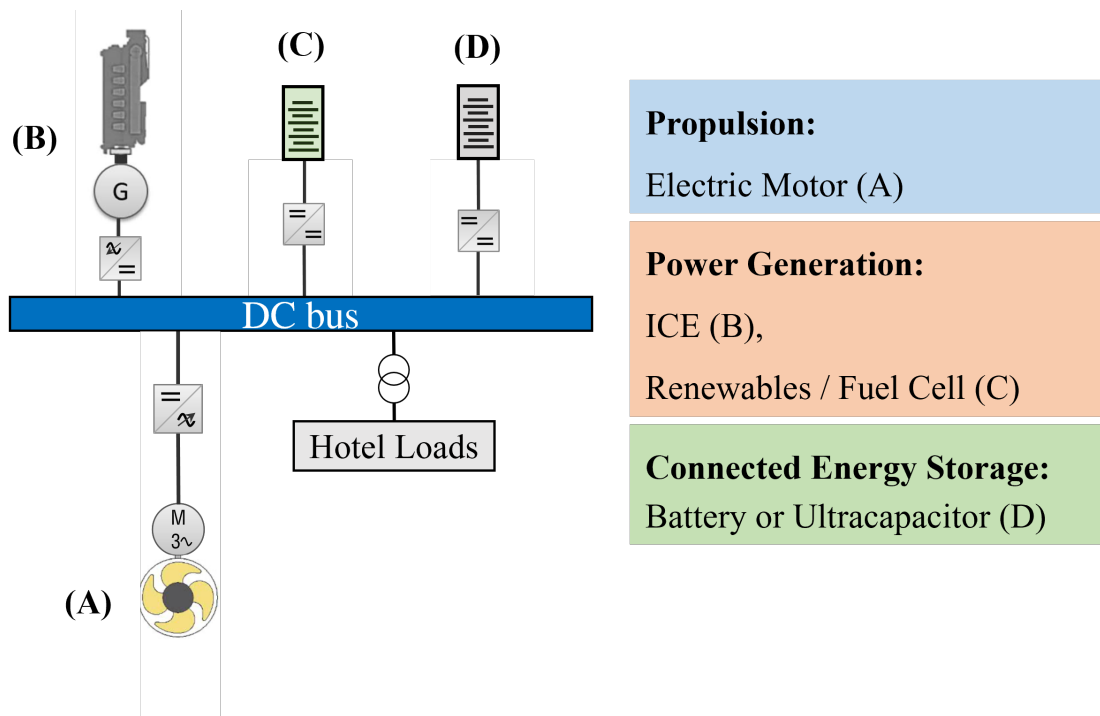
Figure 2.7: Scheme of electric propulsion with DC hybrid power supply

recovery on the shaft of the ICE prime mover [51]. As depicted in Fig. 2.8, the connection between the ICE drive and the shipboard is similar to the VSDEG solution. The propulsive engine speed depends on the input speed required by the gearbox while the engine load is optimized in order to achieve low SFC. The share of generated power exceeding the propulsive load is converted to electrical energy and rectified to be managed by the DC bus, then stored in the battery or used for electrical loads.

Zero Emissions Ship

A zero emissions ship (ZES) refers to a ship that does not produce any greenhouse gas emissions during its operation. It is a concept aimed at reducing the environmental impact of the shipping industry. Fig. 2.9 presents a simple scheme for this powertrain configuration. The electric propulsion plant and hotel loads are powered by renewable energy systems and hydrogen fuel cells. The challenge of zero pollutant emissions cannot be achieved by exploiting batteries alone to power the ship due to the energy density of the storage that, for medium to long distances, would make the weight of the battery and the time lost during stops for recharging unaffordable.

The IMO, through the Initial IMO Strategy to Reduce GHG Emissions [10], guides to identify the energy sources and technologies available and under research to canalize the efforts of getting a true ZES. The development of a ZES consider options to retrofit existing ships because the replacement process is not enough to overcome the inefficient
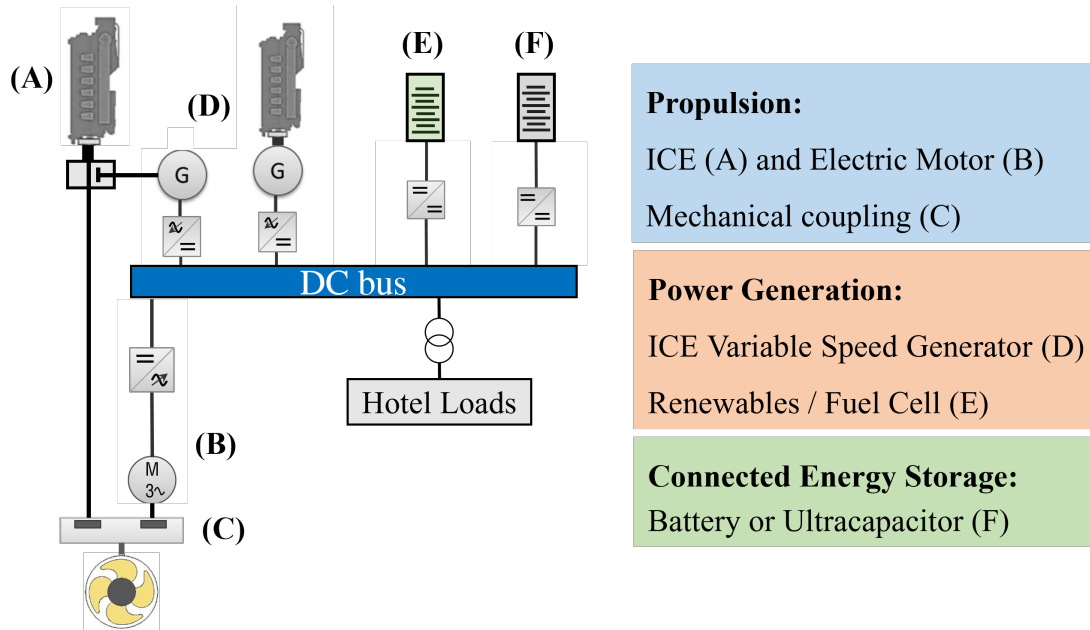
Figure 2.8: Scheme of series-parallel hybrid electric propulsion with DC hybrid power supply

Propulsion:

ICE (A) and Electric Motor (B)

Mechanical coupling (C)

Power Generation:

ICE Variable Speed Generator (D)

Renewables / Fuel Cell (E)

Connected Energy Storage:

Battery or Ultracapacitor (F)
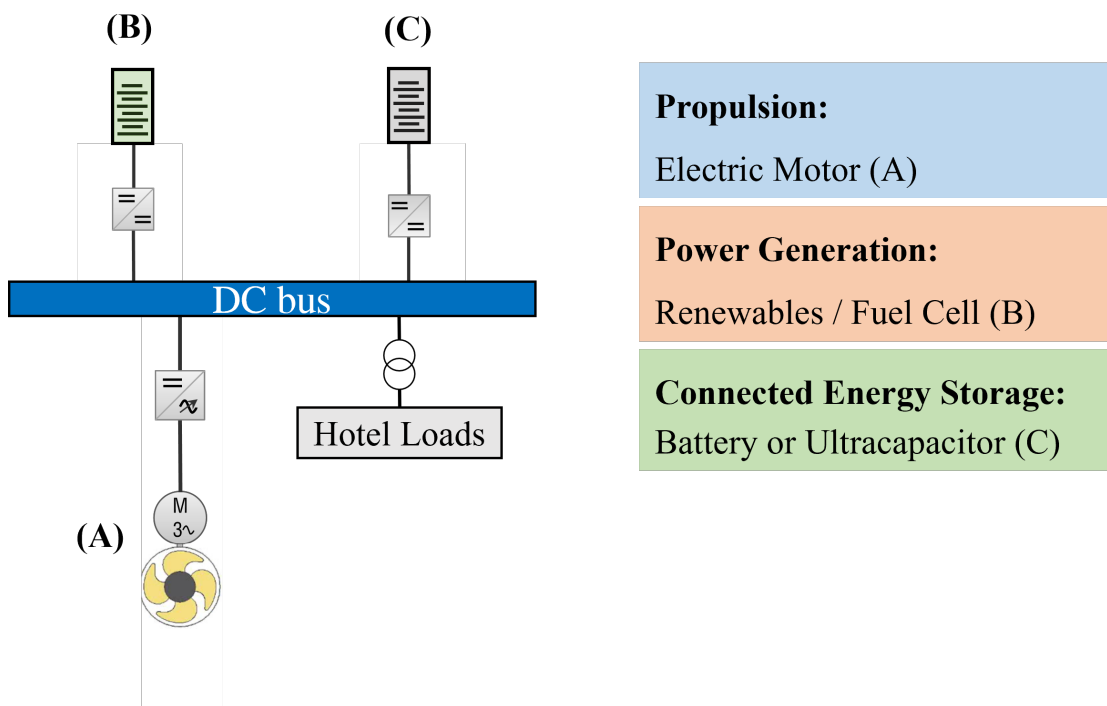
Figure 2.9: Scheme of zero emission ship powertrain

Propulsion:

Electric Motor (A)

Power Generation:

Renewables / Fuel Cell (B)

Connected Energy Storage:

Battery or Ultracapacitor (C)

existing ocean-going fleet, which is almost complete based on the consumption of fossil fuels [52]. ZESs are a viable option for vessels operating in coastal areas, such as ferries or Ro-Ro pax vessels in general. These vessels operate for most of their life in areas subject to restrictions on emissions produced.

Both traditional and hybrid-electric ships can benefit from the design and implementation of Renewable Energy Sources (RESs). Advances in technology and accessible solutions are prompting the shipping industry to consider RESs as a step towards achieving emission-free and carbon-neutral maritime transport. In the shipping context, the primary renewable energy sources explored include solar energy [53] [54], wind energy [55] [56], wave energy [57], and biofuels [58], often integrated into hybrid systems [59]. Photovoltaic cells aim to provide extra electrical energy for a ship's propulsion or other onboard electrical needs. While solar energy can be useful for the ship's auxiliary power needs, its contribution to propulsion is limited. The output power is very limited because it is directly related to the available surface where the PV can be implemented and a low power level by the square meter (a few hundred W/m^2). The power output of solar panels is subject to fluctuations due to factors such as weather conditions, geographical location, panel orientation, and thermal losses [60]. This inconsistency in power generation can pose a challenge for ships that require a constant energy supply. As a solution, ships often employ energy storage systems like batteries in conjunction with solar panels. This arrangement is typically part of a more comprehensive hybrid system onboard ships. Lan et al., for example, designed a hybrid system combining PV, diesel, and batteries, aiming to maximize system size and diesel engine efficiency while accounting for environmental factors [61]. Moreover, the ship's physical movements are also affecting the PV-ESS system efficiency, for instance, the swinging effect is studied by Wen et al. [62]. Generating consistent power from PV panels in marine conditions is challenging. Environmental factors like salt spray and seawater can significantly reduce their efficiency. Zhang and Yuan [63] found that the combined impact of these factors can lead to a 6% reduction in power. Given the limited capacity of solar panels and the need for regular cleaning to maintain efficiency, their use on ships is mainly as auxiliary or supplementary power sources. Fig. 2.10 shows the full PV powered catamaran Turanor PlanetSolar. The boat is registered in Switzerland and was financed by a German entrepreneur. It is covered in over 500 square meters of solar panels rated at 93 kW, its hull is capable of hosting 200 persons, the shape of the boat means that it is able to reach speeds of up to fourteen knots.

Wind energy can be harnessed in different ways to support a ship's propulsion and decrease the main power system's workload. Common methods to include Flettner rotors, kites, wind turbines, and wing sails. Flettner rotors, invented in the 1920s, utilize the Magnus effect. When wind flows over the rotating rotor, it creates a thrust force perpendicular to the wind's direction [64]. These rotors can produce power even if the ship's speed surpasses the wind's speed and are more influenced by wind direction
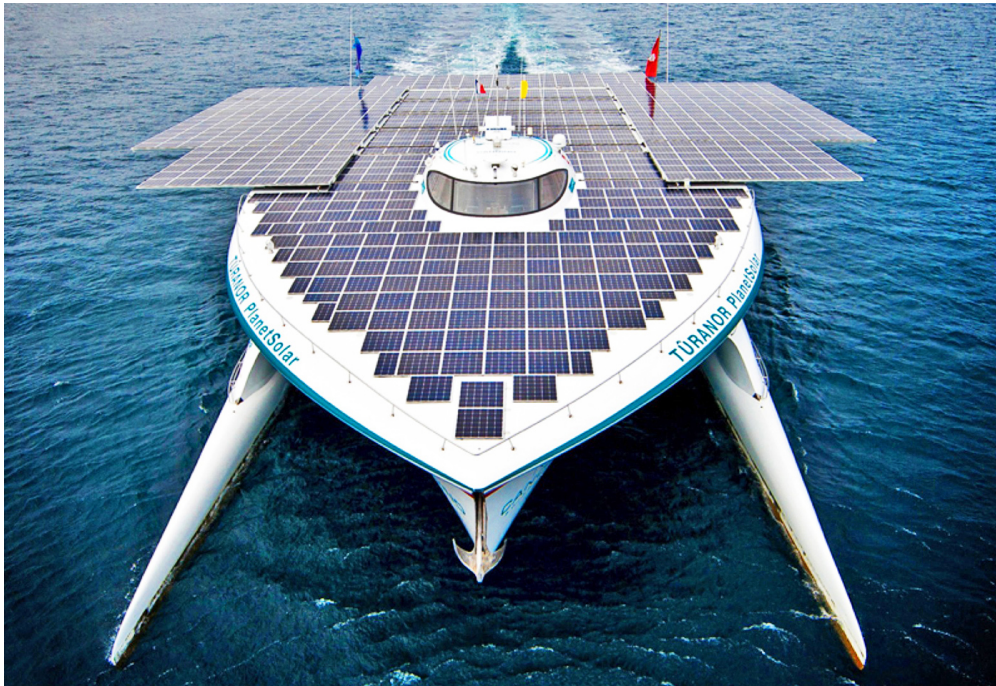
Figure 2.10: Turanor PlanetSolar fully photovoltaic-powered ship.

than its speed. Simulations indicate that Flettner rotors can reduce fuel usage by up to 20% [65]. A modern application of this technology is the E-Ship-1 project from 2010, Fig. 2.11 shows the vessel employed in the transport of off-shore wind turbine blades. This ship combines two 3.5 MW diesel engines with four Flettner rotors, allowing it to achieve speeds of 17.5 knots [66].

Soft sails and kites are more traditional methods, directly harnessing wind power. Their effectiveness depends on wind strength and direction, and they can be used on most ships without needing extra space. An example of kite use on an ocean-going vessel is illustrated in [122]. Kite systems can achieve up to 50% efficiency in specific conditions like a Beaufort-7 wind scale, contingent on atmospheric and oceanic conditions [67]. Wind turbines offer another approach. A comprehensive comparison between horizontal and vertical axis wind turbines is provided in [65]. Vertical axis turbines have several benefits, such as a simpler design, reduced costs, and easier ship installation due to a lower center of mass, enhancing stability. However, despite these marine benefits, horizontal axis turbines generally have superior efficiency and a higher power generation capacity.

Hybrid configuration of fuel cells (FC) and batteries is known as an efficient combination of clean energy devices to supply the auxiliary loads and providing propulsion power to Zero Emissions Ferry Ships (ZEFSs). Energy produced by FCs is the the main energy resource while batteries can responds to the fast dynamics of the loads that FCs are not capable to cover [68]. Moreover, energy from Photovoltaic system (PV) and cold

Figure 2.11: E-Ship-1, with 4 Flettner rotors, during the trafport of off-shore wind turbine blades

ironing at the harbours can be considered as optional resources along with the Energy Management System (EMS) to improve the efficiency of these ships. However, when changing the application from the ZEFS to larger ocean-going ships, several technological and logistic challenges emerge, such as: energy density, weight of power generation devices and converters and port interface support, which must be taken into consideration, before its implementation. In this field of applications, hybrid propulsion systems exhibit many advantages, but a concern need further development from marine industry.

2.2   The Role of PEM Fuel Cells in Ship Power Systems

Fig. 2.12, based on the perspective of the European Commission Directorates-General for Energy and Transport [69], depicts the potential applications of fuel cells. Fuel cells are an emerging technology, suitable for providing heat and electricity for stationary purpose, as well as powering electric vehicles. The best fuel cells operate on pure hydrogen. However, other fuels like natural gas, methanol, or gasoline can be reformed to produce the required hydrogen.

In trasport sector, Proton Exchange Membrane Fuel Cell (PEMFC) are the selected typology of electro-chemical cell that best meet the power demand in transport applications, mainly because of the capability to handle transient performance. The research and development of power generation systems based on PEMFC is leading the carbon-free transition in automotive industry more than other sectors. The state of the art presents numerous works on the investigation of the main criticalities of PEMFCs for
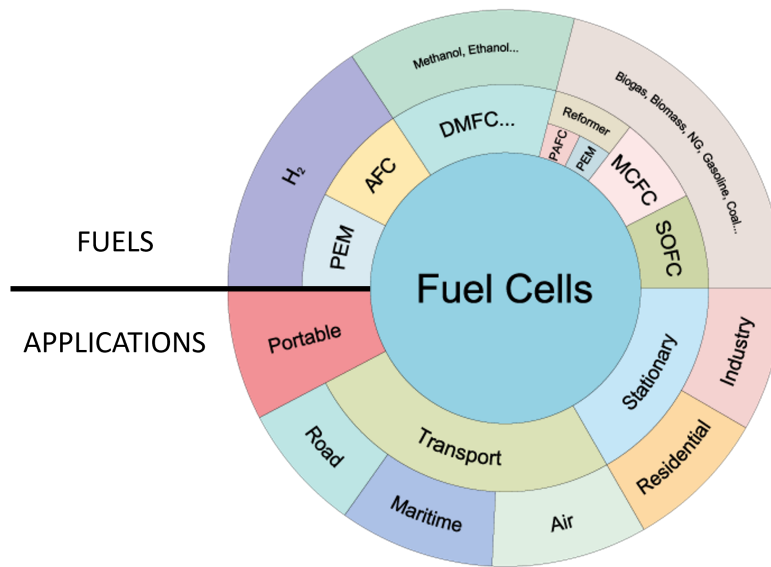
Figure 2.12: Scheme of Fuel Cells role in power generation and transport applications

automotive applications. Kim M.J. et al. [70] formulated a combined power management/design optimization problem for the performance optimization of Fuel Cell Hybrid Vehicles (FCHVs). Fletcher T. et al. in [71] proposed a system level model in order to estimate the effect of the energy management strategy (EMS) on the fuel cell degradation and use it to produce an optimal strategy for a low-speed hybrid vehicle. Ahluwalia R. et al. [72] provides a novel techno-economic comparison of hydrogen fuel cell & battery hybrid powertrains to traditional diesel powertrains for three hallmark off-road vehicles: tractors, wheel loaders, and excavators. A data driven fuel cell lifetime prediction model for an electric city bus was presented in [73].

The railway industry has a strong interest in finding sustainable solutions to power trains that run in non-electrified areas, or support off-grid maintenance work [74]. Li Q. et al. in [75] proposed an energy management system of high-power hybrid tramway in order to guarantee a safe operating condition with transient free for the PEMFC. Despite this technology's potential in the railway sector, its corresponding state of the art does not yet reflect its full capabilities.

In the maritime transport sector, PEMFCs can be best exploited in ferries, as an alternative to batteries or in combination with them. [14] proposes a holistic design methodology for coastal hybrid ships to optimize its plug-in hybrid fuel cell and battery propulsion system via two case studies, in this work power source degradations and optimal energy management between multiple power sources are considered in the optimization. In [76], the economic feasibility of a fuel cell powered ferry vs diesel and biodiesel today, and in a future scenario, was evaluated based on a real world operation profile. In [77] the problem of simultaneous optimal energy management and component sizing for a zero-emission ferry ship is investigated.

The PEM Fuel Cells as Alternative to Batteries

The upcoming regulations to achieve zero-emission passenger transport require challenges for designing new ferries powertrains. Relying only on batteries, particularly to cover medium/long distances, is not feasible due to the limited storage energy density, around $0.2kWh/kg$ depending on type of battery. In comparison, PEMFC system has an energy density of $39.7kWh/kg$ [78]. It would be more efficient and cost-effective to set up the batteries in hybrid configurations, optimizing the loadings on other power sources (e.g., fuel cells or internal combustion engines). Therefore, it is essential to explore other options featuring higher energy storage densities and recharging/refueling rates.

A Ragone plot is a graph used to evaluate and compare the efficiency of different energy sources. In such a chart the specific energy (Wh/kg) is plotted versus the specific power (W/kg). Typically, both axes use a logarithmic scale. This kind of plot was first introduced to compare the performance of batteries. Nevertheless, it is suitable for comparing any kinds of energy storage devices. Fig. 2.13, proposed by [79], shows the Ragone plot of principal power generation and energy storage devices. This tool is very effective during the preliminary design of the power system, because it makes it easy to identify the best resource available to meet the reference application demands.
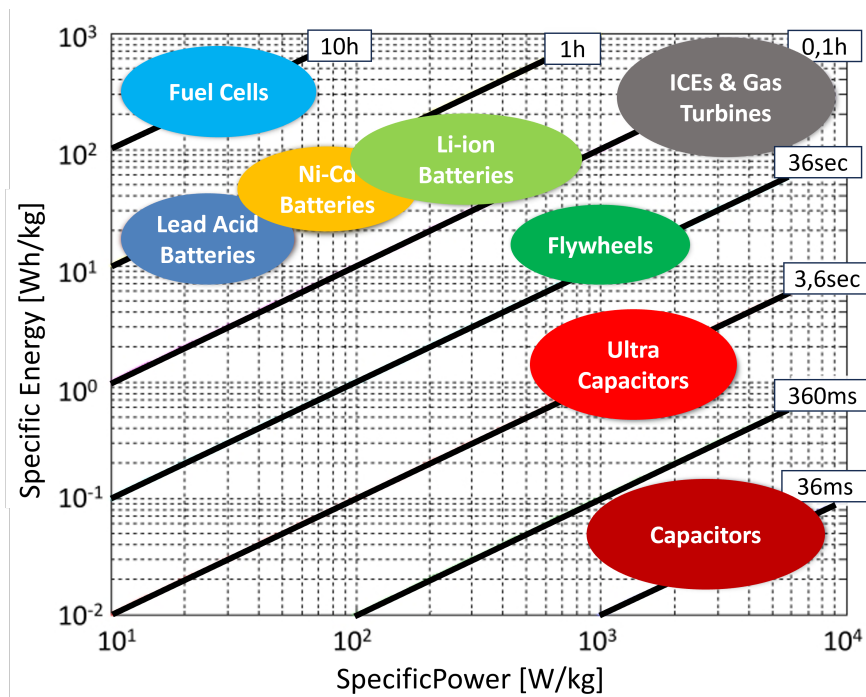
Figure 2.13: The Ragone plot of main power generation and energy storage devices [79]

In recent years, several alternatives to traditional batteries have emerged for powering shipboard loads. These include flywheel batteries, renewable systems, and hydrogen fueled technology. Currently, hydrogen is the main protagonist of the global energy

future, being a carbon free fuel. Indeed, the research on propulsion systems based on hydrogen combustion is promoting the development of zero emission solutions exploiting gas turbines [80] and direct injection combustion engines [81] [82]. Nevertheless, hydrogen-fueled fuel cells may be the technology that best meets ferry vessel requirements. Fuel cells convert chemical energy directly into electrical energy, omitting the indirect route via thermal energy in combustion engines. This reduces NO_x formation, noise and vibrations while maintaining high efficiencies. Fuel cells are modular in nature and power production can be distributed over the ship, reducing electricity transport losses and improving redundancy. FC systems have good partial load characteristics and a high volumetric energy density compared to batteries. Although the volumetric power density is low compared to batteries and internal combustion engines, the energy storage density is significantly higher [83]. Two of the most efficient and researched types of fuel cells are the Proton Exchange Membrane Fuel Cell (PEMFC) and the Solid Oxide Fuel Cell (SOFC). The PEMFC showed a rapid development in recent decades and has achieved high power densities and good transient performance. Its membrane consists of a proton-conducting wetted solid polymer. However, the necessity of a wet membrane while the gas-diffusion pores have to remain dry dictates an operational temperature of 65-85°C and complicates water management. At low temperatures, the use of platinum is required to catalyze the electrochemical reaction. Another disadvantage of the low operational temperature is the limited tolerance to fuel impurities. In particular, carbon monoxide (CO) deactivates the catalyst because of its strong surface adsorption at low temperatures [83].

The SOFC has also been heavily investigated in recent decades and various classes have been developed with operating temperatures ranging from 500 to 1000°C. The low-temperature classes are mainly applied in stand-alone fuel cell products with electrical efficiencies up to 60%, while high-temperature SOFCs are targeted for combined operation with gas turbines where efficiencies over 70% are projected [83] [51]. Despite being a promising type, their limited development state, mechanical vulnerability, and high cost have so far limited widespread adoption of SOFC technology [83]. PEMFCs have a higher efficiency percentage (53–60%) compared to SOFCs (35–43%). This could be explained by the high working temperatures of SOFCs which involve longer start-up times and mechanical and chemical compatibility issues. Despite this shortcoming, SOFCs have higher stack size power output (up to $2000kW$) when compared to PEMFCs (up to $150kW$) [83].

There has been an increasing interest in utilizing PEMFC for ship applications after the adoption by parallel industries such as road transport. Compared to other fuel cell types, PEMFC offers better power density and transient performance, but lower efficiency and less fuel flexibility. When used in transport applications, PEMFC is typically used with batteries or supercapacitors to provide better overall efficiency and capability for managing power transients [78]. Compared to lithium-ion batteries, the

degradation in PEM fuel cell systems during downtimes is significantly lower than during operation [84]. Due to the separation of energy storage and power supply in a Fuel Cell Electric Vehicle (FCEV) by the external hydrogen tank, FCEVs are in competition with Battery Electric Vehicles (BEV) in marine and heavy-duty transports for long-haul applications.

The PEM Fuel Cells Economic Scenario

The economic scenario behind PEM fuel cells is influenced by several factors, including the cost of hydrogen, the materials used in production, and technological advancements. Fig. 2.14 shows the results, proposed by [85], of the Forecast breakdown of renewable hydrogen production costs worldwide from 2020 to 2030, in two different scenarios. The cost of producing renewable hydrogen is predicted to drop in the coming years. In 2020, the average cost of renewable hydrogen was six U.S. dollars per kilogram, while in the best-case scenario, it was 5.4 U.S. dollars per kilogram. By 2030, these costs are anticipated to fall to 2.3 and 1.4 U.S. dollars per kilogram, respectively. In the average scenario, wind energy - generally offshore power - is used to produce hydrogen, while the optimal scenario assumes a combination of wind and solar energies.
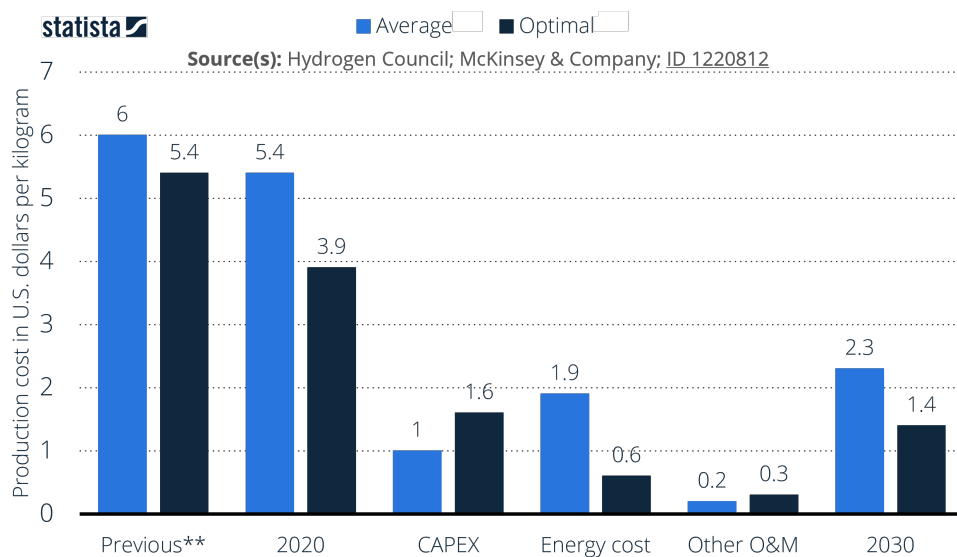
Figure 2.14: The forecast breakdown of renewable hydrogen production costs worldwide from 2020 to 2030 by [85].

The cost of manufacturing PEMFCs is one of the most critical factors against their diffusion. Cigolotti V. et al. in [86] proposes an analysis on large-scale production. Fig. 2.15 shows the results of the analysis, summarizing the breakdown for 1000 units produced per year and 50000 units produced per year. As production scales up, the cost per unit decreases significantly. For a $1kW$ size, the total stack cost can be slashed by over 50%, going from \$1052.34 per kW to \$460.09 per kW. This cost reduction due to

larger production scales is more pronounced for smaller sizes; for instance, there's a 27% decrease for a $5kW$ size. In every scenario examined, the Membrane Electrode Assembly (MEA) consistently accounted for the largest portion of the overall cost. The bipolar plate rates have almost an equal share coming from the anode and cathode sides, while the anode/cooling gaskets contribute more than the cathode gasket to the overall gasket rate" specify the acronyms
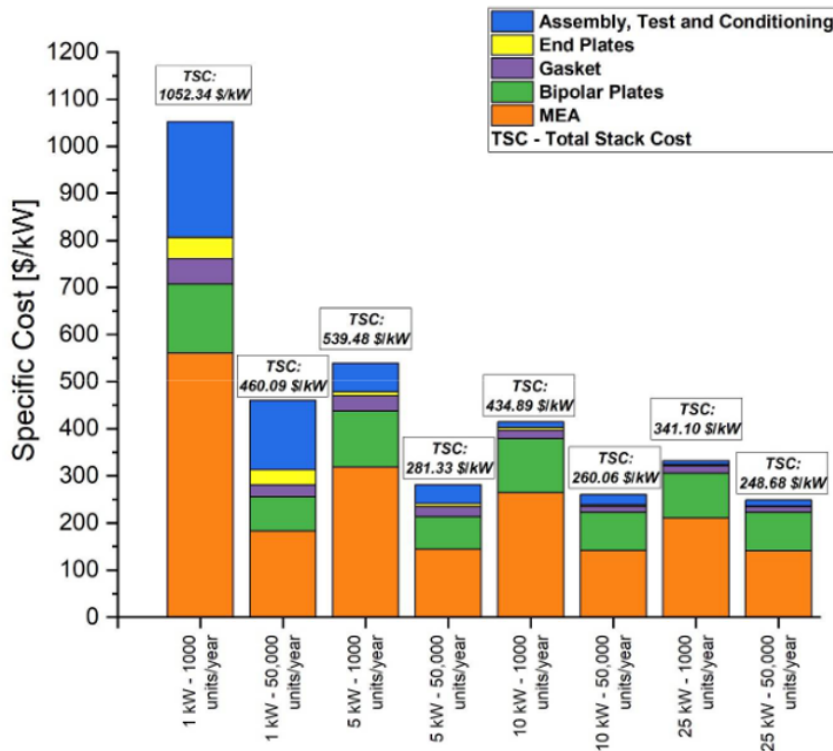
Figure 2.15: PEM Fuel Cell stack potential cost breakdown. Results proposed by [86].

The degradation of the PEMFC system is a current research topic, with scientific and especially economic implications. In fact, the study of degradation mechanisms and lifetime prediction of a PEMFC is being developed both from the perspective of the fuel cell and its applications. PEMFC residual life prediction method, validated via experiment, and economic lifetime is studied in [87]. In [88] the method of predicting the lifetime of PEMFCs using the current degradation law enhances the use of degradation information in current density. This is a practical approach for evaluating and predicting the lifetime of not-stationary fuel cells.

2.3 Modeling and Numerical Investigations

The recent scientific literature on Proton Exchange Membrane Fuel Cells (PEMFCs) presents several papers with both modeling and experiment-based approaches. Mathe-

matical models can aid in the development and control of a PEMFC system by reducing development time and cost through system prototyping and testing. Furthermore, models can also be exploited for diagnostic purposes, to identify the main unhealthy behaviors and their causes to define and improve suited control strategies [89]. Additionally, the use of mathematical models can facilitate a holistic design approach for PEMFC systems. Different hypotheses and modelling approaches adopted in low computational cost PEMFC system models were reviewed in [90]. In [91] using analytical order reduction and approximation methods, the fluxes and source terms in conventional 1D conservation equations are reduced to six computing nodes at the interfaces between each cell component. In the work shown in [92] and [93], two models were developed in the MATLAB-Simulink environment, the first focusing on single-cell modelling, making the model computationally feasible to be integrated into a system-level model, while the second proposes stack modelling and comparison with experimental results.

2.4   Experimental Analyses

Gadducci E. et al. in [94] reports the results of an experimental assessment of a 240 kW real-scale test rig complete with auxiliaries, made up of 8 PEMFC stacks. The experiments presented focused on the response of the FC system to static, dynamic, and typical maritime operative load profiles. Furthermore, the Gadducci E. et al. study gives important suggestions and criteria for the design, construction, and control of similar fuel cell complete systems for maritime applications. Yin L. et al. in [95] described the 5 kW PEMFC laboratory set-up and the related control system. The proposed results concern the improvement of the performance by optimizing air flow rate at fuel cell inlet.

Experimental works on thermal management of Low Temperature PEMFC (LT-PEMFC) include a proposed methodology for fault diagnosis of the thermal management system to ensure the system reliability by [96]. Xu J. et al. in [97] modeled the vehicle integrated thermal management system and proposed control strategies. Yan W. et al. [98] applied different cathode flow channel configurations to improve fuel cell performance. Oruganti P.S. et al. in [99] shows, through simulation, the effect of thermal management on component sizing, while in [100] study, by a reduced order model, the behavior of the cooling system for a Fuel Cell Electric Vehicle (FCEV) under reference duty cycle. A comparison between experimental results and simulations is shown in [101], in which the case study was a test bed of a flow extension system using a commercially available 30 kW stack. Fig. 2.16 shows an overview of the used test bench components by Hoeflinger J. et al. in [101].
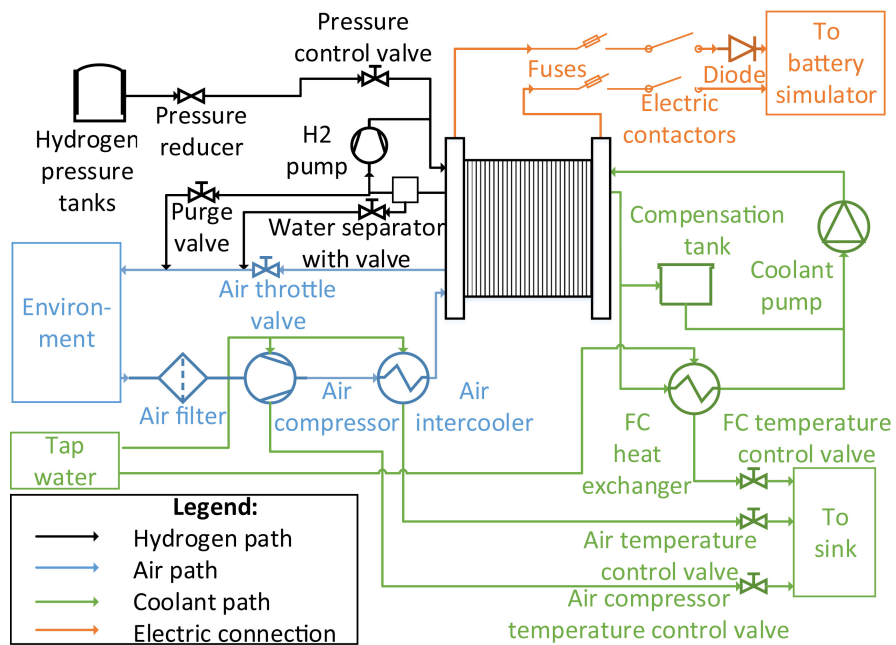
Figure 2.16: Schematic diagram of the fuel cell test bench proposed by [101].

Chapter 3

The Fuel Cell Technology

Fuel cells convert chemical energy directly into electricity, making them more efficient than combustion engines. Unlike engines, fuel cells can be entirely solid-state, with no moving parts, leading to potentially longer-lasting and more reliable systems. This yields the potential for highly reliable and long-lasting systems. A lack of moving parts also means that fuel cells are silent.

A unique advantage of fuel cells over batteries is the separation of power and capacity scaling. In fuel cells, the power output is determined by the cell size, while the capacity depends on the fuel storage size. In contrast, the power output of batteries is related to the capacity, making scaling challenging, especially for larger sizes. Fuel cells can efficiently be scaled from small sizes (e.g. like a smart phone) to large sizes for power plants. They can also offer higher energy storage than batteries and can be quickly recharged by refueling. On the other hand, batteries either need replacement or a lengthy recharge period. In summary, Fig. 3.1 visually compares the features of fuel cells, batteries, and internal combustion engines, highlighting their respective advantages and limitations.
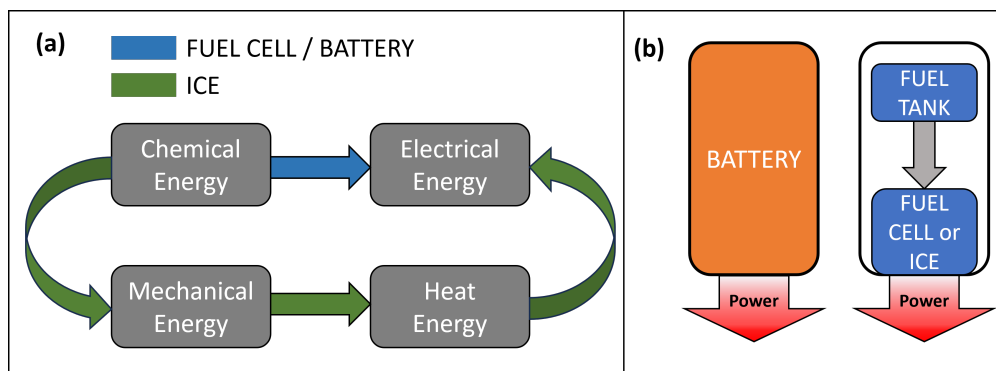
Figure 3.1: (a) Fuel cells and batteries produce electricity directly from chemical energy. In contrast, combustion engines first convert chemical energy into heat, then mechanical energy, and finally electricity. (b) The battery is both the energy storage and the energy conversion device. In contrast, fuel cells and combustion engines allow independent scaling between power and capacity.

Tab3.1 summarize the principal aspect of the five major types of fuel cells, differentiated from one another by their electrolyte.

Table 3.1: Description of Major Fuel Cell Types.

	PEMFC	PAFC	AFC	MCFC	SOFC
Electrolyte	Polymer membrane	Liquid H_3PO_4	Liquid KOH	Molten carbonate	Ceramic
Charge carrier	H^+	H^+	OH^-	CO_3^{2-}	O^{2-}
Operating temperature	$80°C$	$200°C$	$60\text{-}220°C$	$650°C$	$600\text{-}1000°C$
Catalyst	Platinum	Platinum	Platinum	Nickel	Perovskites (ceramic)
Cell components	Carbon based	Carbon based	Carbon based	Stainless based	Ceramic based
Fuel compatibility	H_2, methanol	H_2	H_2	H_2, CH_4	H_2, CH_4, CO

Despite all five fuel cell types are based on the same underlying electrochemical principles, they all operate at different temperature regimens, incorporate different materials, and often differ in their fuel tolerance and performance characteristics, as shown in Tab.3.1. The research focuses on PEMFCs or SOFCs, as promising devices to enanche the hydrogen transition. We will briefly contrast these two fuel cell types [102].

- **PEMFCs** employ a thin polymer membrane as an electrolyte. The most common PEMFC electrolyte is a membrane material called Nafion. Protons are the ionic charge carrier in a PEMFC membrane. PEMFCs are attractive for many applications because they operate at low temperature and have high power density.

- **SOFCs** employ a thin ceramic membrane as an electrolyte. Oxygen ions (O^{2-})are the ionic charge carrier in an SOFC membrane. The most common SOFC electrolyte is an oxide material called yttria-stabilized zirconia (YSZ). To function properly, SOFCs must operate at high temperatures ($>600°C$). They are attractive for stationary applications because they are highly efficient and fuel-flexible.

The current produced by a fuel cell scales with the size of the reaction area where the reactants, the electrode, and the electrolyte meet. To provide large reaction surfaces that maximize surface-to-volume ratios, fuel cells are usually made into thin, planar structures, as shown in Fig. 3.2.

The electrodes are highly porous to increase the reaction surface area further and ensure good gas access. One side of the planar structure is provisioned with fuel (the anode electrode), while the other side is provisioned with oxidant (the cathode electrode).
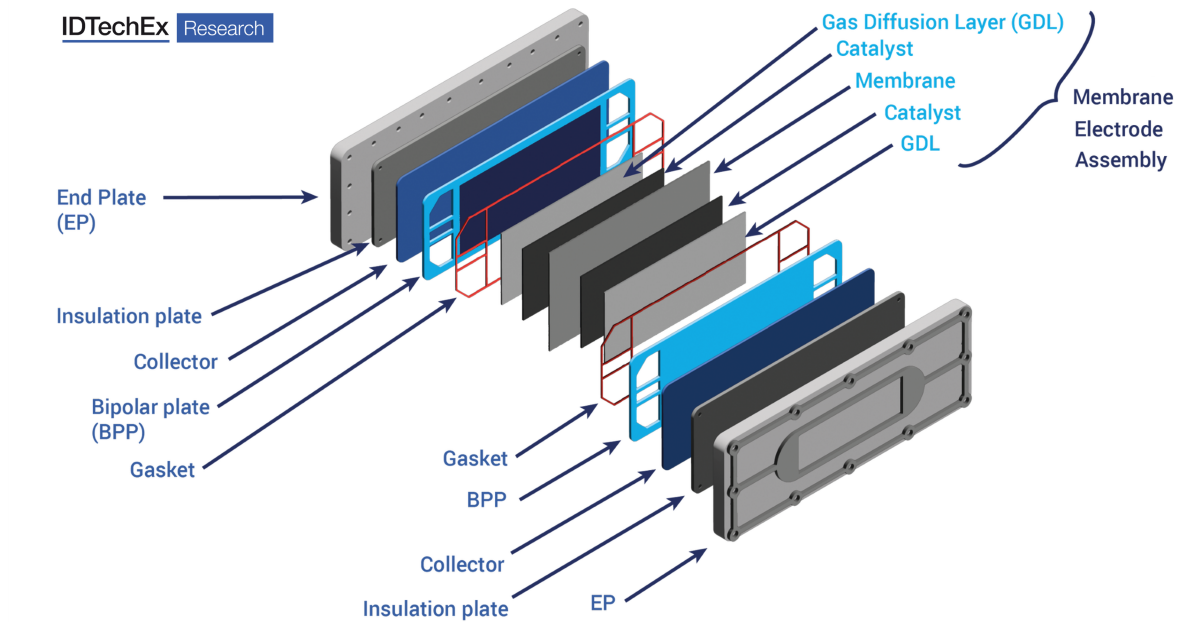
Figure 3.2: Exploded Proton Exchange Membrane Fuel Cell (PEMFC) (*www.idtechex.com*).

A thin electrolyte layer spatially separates the fuel and oxidant electrodes and ensures that the two individual half-reactions occur in isolation from one another.

Fig. 3.2, presented in [103], shows the main components of a PEM cell and in particular highlights the elements of the Membrane Electrode Assembly (MEA). MEA plays a crucial role in PEM fuel cells, and their design and performance have been extensively studied. Mathematical models and simulations have been developed to optimize performance, and various electrode configurations have been analyzed. Tab.3.2 provides a summary of the materials, purpose, and critical issues related to each element of the MEA.

The performance degradation of MEA at $80°C$ after 100 hours of operation was mainly due to carbon corrosion, Pt agglomeration and dissolution, drying and cracking of the membrane [104]. MEA replacement in PEM fuel cells can be facilitated by using bipolar plates with keys and through holes, allowing for easy disassembly and reassembly.

The performance of a fuel cell device can be summarized with a graph of its current–voltage characteristics. This graph, called the polarization curve, shows the voltage output of the fuel cell for a given current output. An example of a typical polarization curve for a PEMFC is shown in Fig. 3.3. Because an FC with a larger active area produces more electricity, polarization curves are normalized by fuel cell area to make results comparable.

An ideal fuel cell would supply any amount of current while maintaining a constant

Table 3.2: The principal characteristics of MEA components in a PEMFC

	Proton Exchange Membrane (PEM)	Catalyst Layer	Gas Diffusion Layer (GDL)
Materials	Fluoropolymer--copolymer, Nafion.	Platinum or platinum alloy supported on carbon black.	Carbon black.
Functions	Is a selective barrier, only protons to pass through while blocking electrons, ensuring that electrons travel through an external circuit, generating electricity.	Support the reactions. At the anode, it assists in splitting hydrogen molecules, at the cathode, it aids in reducing oxygen molecules.	Distributes reactant gases uniformly over the catalyst layer. Provides a pathway for electrons to travel along the external circuit. Facilitates water management by moving H_2O away from the catalyst layer.
Criticalities	The membrane must remain hydrated for optimal proton conductivity. It's susceptible to drying out, which can reduce performance. It can degrade over time, if exposed to contaminants or if the cell operates at high temperatures.	Platinum, being expensive, contributes significantly to the cost of PEMFCs. The catalyst can also degrade over time reducing the fuel cell's efficiency and lifespan.	Water management is crucial. If the GDL becomes too saturated, it can hinder gas diffusion, leading to reduced performance. Conversely, if it's too dry, it can cause the PEM to dehydrate.

voltage determined by thermodynamics. In practice, however, the actual voltage output of a real fuel cell is less than the ideal thermodynamically predicted voltage due to variation from standard conditions. Furthermore, the more current that is drawn from a real fuel cell, the lower the voltage output of the cell, limiting the total power that can be delivered. Therefore, as fuel cell voltage decreases, the electric power produced per unit of fuel also decreases. In this way, fuel cell voltage can be seen as a measure of fuel cell efficiency. The electric potential losses related to the increase of the produced current are called overpotential. The overpotential losses are caused by three different reasons connected to three phenomena:

- **Activation losses** - due reaction kinetics;

- **Ohmnic losses** - from ionic and electronic conduction;

- **Concentration losses** - due mass transport.

The three major losses each contribute to the characteristic shape of the fuel cell
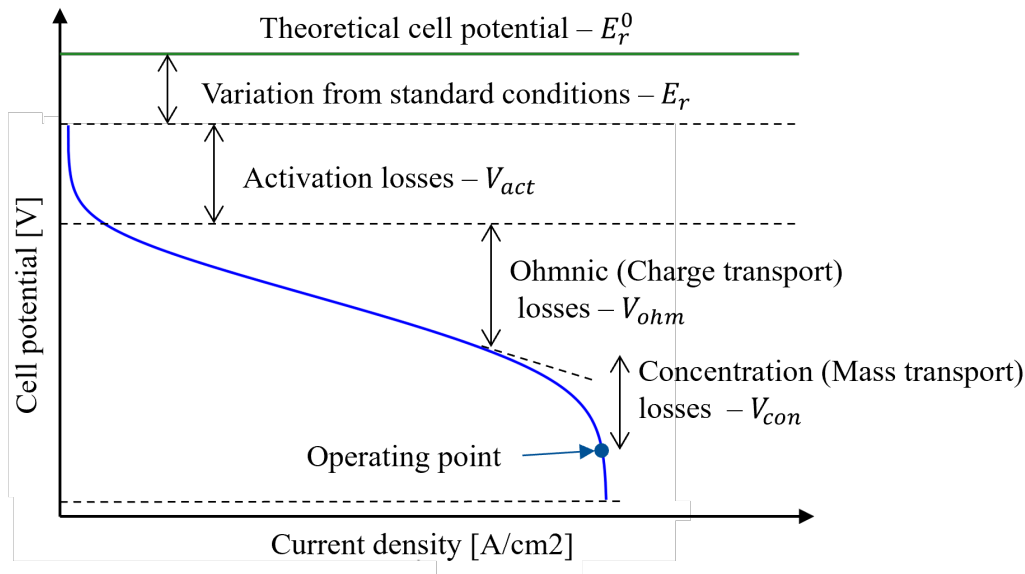
Figure 3.3: Typical PEMFC polarization curve.

polarization curve. As shown in Fig. 3.3, the activation losses mostly affect the initial part of the curve, the ohmic losses are most apparent in the middle section of the curve, and the concentration losses are most significant in the tail of the i–V curve.

3.1 Hydrogen Fuel Cell Thermodynamics

The Gibbs free (G) energy sets the magnitude of the reversible voltage for an electrochemical reaction. For example, in a hydrogen–oxygen fuel cell, the reaction is Eq.(3.1).

$$H_2 + \tfrac{1}{2}O_2 \rightleftharpoons H_2O \qquad (3.1)$$
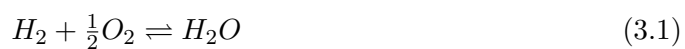
The Gibbs free-energy change is $–237 kJ/mol$ (ΔG) under standard conditions for liquid water product. The reversible voltage generated by a hydrogen-oxygen fuel cell under standard conditions is shown in Eq.(3.2), where n is the number of moles of electrons transferred and F is Faraday's constant ($96'485\ C\ mol^{-1}$).

$$E_r^0 = -\frac{\Delta G^0}{nF} = 1.229V \qquad (3.2)$$

However, most feasible fuel cell reactions have reversible cell voltages in the range of 0.8–$1.5V$. In Tab.3.3 are reported the theoretical potential for different reactions.

Fuel cells are frequently operated under conditions that greatly vary from the standard conditions. Reversible voltage varies with temperature and pressure conditions and also with reactant concentrations. Starting from the Gibbs free energy differential expression in Eq.(3.3) and Eq.(3.2) it is possible to write the variation in G with temperature as in Eq.(3.4).

Table 3.3: Selected List of Standard Electrode Potentials.

Electrode Reaction	E_r^0 [V]
$Fe^{2+} + 2e^- \rightleftharpoons Fe$	-0.440
$CO_2 + 2H^+ + 2e^- \rightleftharpoons CHOOH(aq)$	-0.196
$2H^+ + 2e^- \rightleftharpoons H_2$	+0.000
$CO_2 + 6H^+ + 6e^- \rightleftharpoons CH_3OH + H_2O$	+0.03
$O_2 + 4H^+ + 4e^- \rightleftharpoons 2H_2O$	+1.229

$$dG = -SdT + Vdp \tag{3.3}$$

$$\left(\frac{dE_r}{dT}\right)_p = -\frac{S}{nF} \tag{3.4}$$

Like temperature effects, the pressure effects on cell voltage may also be calculated starting from the differential expression for the Gibbs free energy as in Eq.(3.5):

$$\left(\frac{dE_r}{dp}\right)_T = -\frac{\Delta v}{nF} \tag{3.5}$$

the variation of the reversible cell voltage with pressure is related to the volume change of the reaction Δv. If the volume change of the reaction is negative, hence, fewer moles of gas are generated by the reaction than consumed, then the cell voltage will increase with increasing pressure. This is an example of Le Chatelier's principle: Increasing the pressure of the system favors the reaction direction that relieves the stress on the system. Usually, only gas species produce an appreciable volume change. Assuming that the ideal gas law applies, we can write Eq.(3.6), where Δn represents the change in the total number of moles of gas upon reaction.

$$\left(\frac{dE_r}{dp}\right)_T = -\frac{\Delta n RT}{nFp} \tag{3.6}$$

To understand how the reversible voltage varies with concentration, consider an arbitrary chemical reaction placed on a molar basis for species A in the form of Eq.(3.7). Considering a single mole for the species A:

$$A + bB \rightleftharpoons cC + dD \tag{3.7}$$

where A and B are reactants, C and D are products, and b, c, and d represent the number of moles of B, C, and D, respectively. On a molar basis for species A, ΔG for this reaction may be calculated from the chemical potentials of the various species participating in the reaction. Recognizing that the lumped standard-state chemical potential terms represent the standard-state molar free-energy change for the reaction,

ΔG^0, the equation can be simplified to a final form Eq.(3.8), where a is the reaction activity of the species:
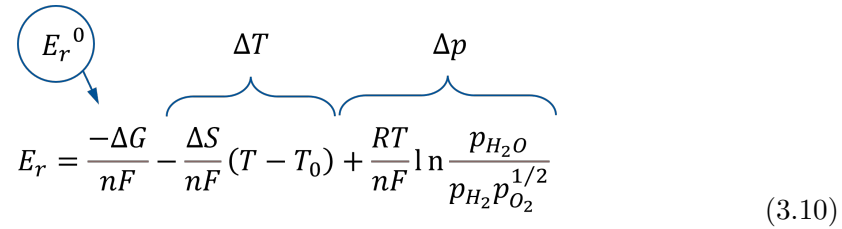
$$\Delta G = \Delta G^0 + RT \ln \frac{a_C^c a_D^d}{a_A^1 a_B^b} \tag{3.8}$$

Now considering the hydrogen-oxygen reaction in Eq.(3.1), it is possible to write the Nernst equation replacing the activities of hydrogen and oxygen gases by their unitless partial pressures ($a_{H_2} = p_{H_2}$, $a_{O_2} = p_{O_2}$), Eq.(3.9).

$$E_r|_T = E_r^0 + RT \ln \frac{p_{H_2O}}{p_{H_2} p_{O_2}^{1/2}} \tag{3.9}$$

From this equation, it is apparent that pressurizing the fuel cell in order to increase the reactant gas partial pressures will increase the reversible voltage. However, because the pressure terms appear within a natural logarithm, the voltage improvements are slight.

Considering the contribution of Eq.(3.4), Eq.(3.6) and Eq.(3.9) is derived the esteem of cell voltage E_r under not standard conditions described in Eq.(3.10)

$$E_r = \frac{-\Delta G}{nF} - \underbrace{\frac{\Delta S}{nF}(T - T_0)}_{\Delta T} + \underbrace{\frac{RT}{nF} \ln \frac{p_{H_2O}}{p_{H_2} p_{O_2}^{1/2}}}_{\Delta p} \tag{3.10}$$

3.2 Hydrogen Fuel Cell Reaction Kinetics

The rate of an electrochemical reaction, or any reaction for that matter, is finite. This means that the current produced by an electrochemical reaction is limited. Reaction rates are finite even if they are spontaneous because an energy barrier (called an activation energy) impedes the conversion of reactants into products. The probability that reactant species can make it over this barrier determines the rate at which the reaction occurs. Suppose the electron transfer step between chemisorbed hydrogen and the metal electrode surface limits the overall reaction. This step is represented in Eq.(3.11).

$$M \cdots H = (M + e^-) + H^+ \tag{3.11}$$

In this equation, $M \cdots H$ represents a hydrogen atom chemisorbed on the metal surface and $(M + e^-)$ represents a liberated metal surface site and a free electron in the metal. In Fig. 3.4, we see a physical representation of a reaction step, while Fig. 3.5 shows its energy aspects.
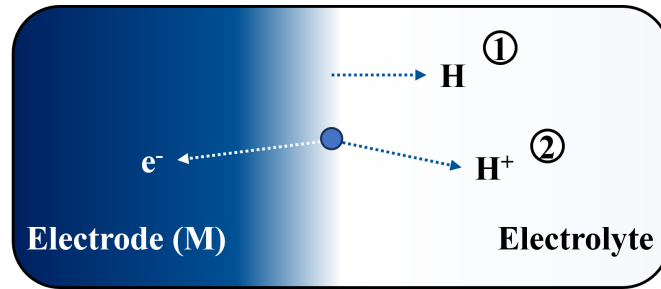
Figure 3.4: Schematic of chemisorbed hydrogen charge transfer reaction. The reactant state, a chemisorbed hydrogen atom is shown at 1 ($M \cdot \cdot \cdot$). Completion of the charge transfer reaction, as shown at 2, liberates a free electron into the metal and a free proton into the electrolyte (($M + e^-$) + H^+).

Curve 1, in Fig. 3.5, Represents the energy of hydrogen atoms (H) attached to a metal electrode. The energy rises as the hydrogen moves away from the electrode. Hydrogen atoms prefer being close to the metal because it stabilizes them. When close, they bond partially with the metal, reducing their energy. Pulling them away breaks this bond, increasing their energy.

In Fig. 3.5, curve 2 shows the energy of a hydrogen ion (H^+) in the electrolyte. As this ion approaches the electrode, its energy goes up due to repulsion between the ion and the electrode. It's not favorable for the H^+ ion to be close to the metal surface because of this repulsion. The ion's energy is lowest when it's deep in the electrolyte, away from the metal.
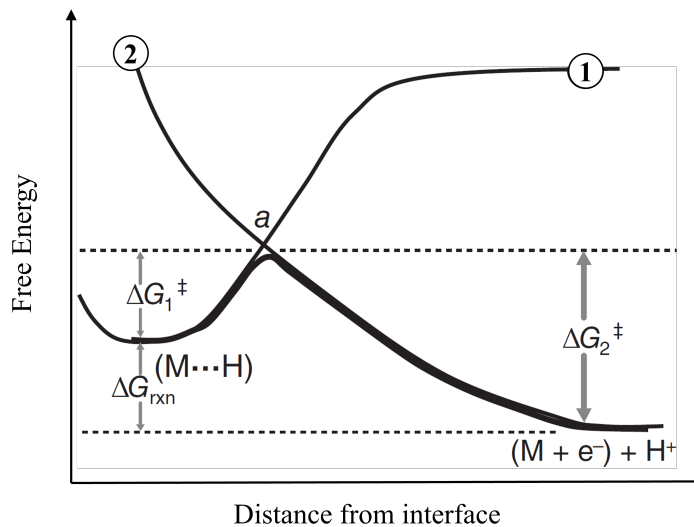
Figure 3.5: Schematic of the energetics of chemisorbed hydrogen charge transfer reaction. Curve 1 shows the free energy of the reactant state ($M \cdots$). Curve 2 shows the free energy of the product state (($M + e^-$) + H^+).

The dark solid line in Fig. 3.5 indicates the path of least energy for converting

attached hydrogen to H^+ and $(M + e^-)$. This path has a peak energy point, meaning there's an energy barrier to overcome. This peak happens because moving away from stable starting and ending points increases energy, as shown by Curve 1 and 2. The peak, labeled a, is the activated state. Once a molecule reaches this state, it can easily transform into a product or revert to a reactant.

For fuel cells, we are interested in the current produced by an electrochemical reaction. At thermodynamic equilibrium, we recognize that the forward and reverse current densities must balance so that there is no net current density, Eq.(3.12).

$$j_{forward} = j_{reverse} = j_0 \tag{3.12}$$

j_0 is the exchange current density for the reaction. Although at equilibrium the net reaction rate is zero, both forward and reverse reactions are taking place at a rate which is characterized by j_0; this is called dynamic equilibrium.

Products in a reaction have a lower energy than the reactants, which means the reaction tends to move forward more easily than it reverses. So, it is expected the forward reaction to be faster than the reverse one. But, as the forward reaction progresses, electrons (e^-) start to gather in the metal electrode, and hydrogen ions (H^+) build up in the electrolyte. This accumulation creates a potential difference, or voltage, across the reaction area, which you can see in Fig. 3.6b.
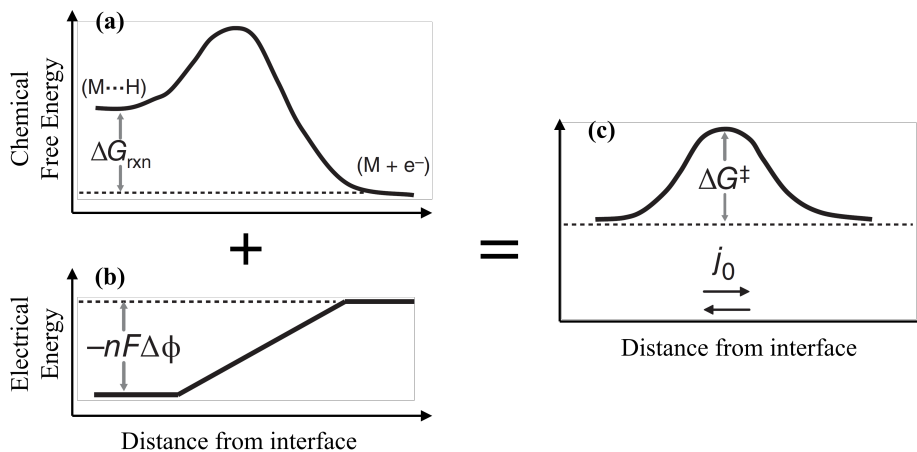
Figure 3.6: At equilibrium, the chemical free-energy difference (a) across a reaction interface is balanced by an electrical potential difference (b), resulting in a zero net reaction rate (c).

This voltage acts as a balancing force. While the chemical reactions naturally favor the forward direction, the growing voltage pushes back, trying to slow it down. The combined effect of this chemical push and electrical pull is shown in Fig. 3.6c. Here, the two forces balance out, making the forward and reverse reactions happen at the same rate. This balanced reaction speed is represented by the exchange current density (j_0).

The potential difference ($\Delta\phi$) is like a weight that ensures both reactions eventually move at the same pace.

The situation for the oxygen reaction at a fuel cell cathode. As in the hydrogen reaction, a difference in chemical free energy between the reactant and product states at the cathode will lead to an electrical potential difference. At equilibrium, the two force contributions balance, leading to a dynamic equilibrium with zero net reaction. As shown in Fig. 3.7 the sum of the interfacial electrical potential differences at the anode and cathode yields the overall thermodynamic equilibrium voltage for the fuel cell.
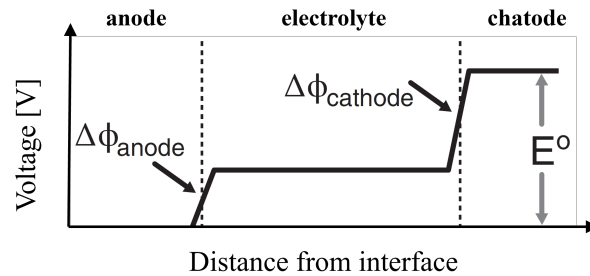
Figure 3.7: Theoretical shape of the fuel cell voltage profile.

The anode ($\Delta\phi_{anode}$) and cathode ($\Delta\phi_{cathode}$) interfacial potentials shown in Fig. 3.7 are called Galvani potentials. For reasons we will not discuss, the exact magnitude of these Galvani potentials are yet unknowable. The Galvani potentials at the anode and cathode of a fuel cell must sum to give the overall thermodynamic cell voltage E_0.

A distinguishing feature of electrochemical reactions is the ability to manipulate the size of the activation barrier by varying the cell potential. By not using the full potential (Galvani potential) across the reaction, it is possible to change the energy balance in favor of the forward reaction. This means that by giving up some of the cell's maximum possible voltage, you can get a steady current from your fuel cell. To achieve this, the Galvani potentials at both the anode and cathode need to be lowered, though not necessarily by the same amount.

Fig. 3.8 focuses on a nanometer-sized dimension right at the interface between the anode and the electrolyte. Here, the Galvani potential appears to rise gradually across the 1–2 nm thickness of this interface, as shown in Fig. 3.8b. However, when you zoom out and view this on a larger scale this gradual increase looks more like an almost instant voltage jump.

When the Galvani potentials decrease at both the anode and cathode (a necessary step to push the reactions forward), the overall voltage of the fuel cell drops as a result.

As shown in Fig. 3.8c, decreasing the Galvani potential by η reduces the forward activation barrier and increases the reverse activation barrier. Figure shows that the forward activation barrier is decreased by $\alpha nF\eta$, while the reverse activation barrier is increased by $(1-\alpha)nF\eta$. The value of α depends on the symmetry of the activation
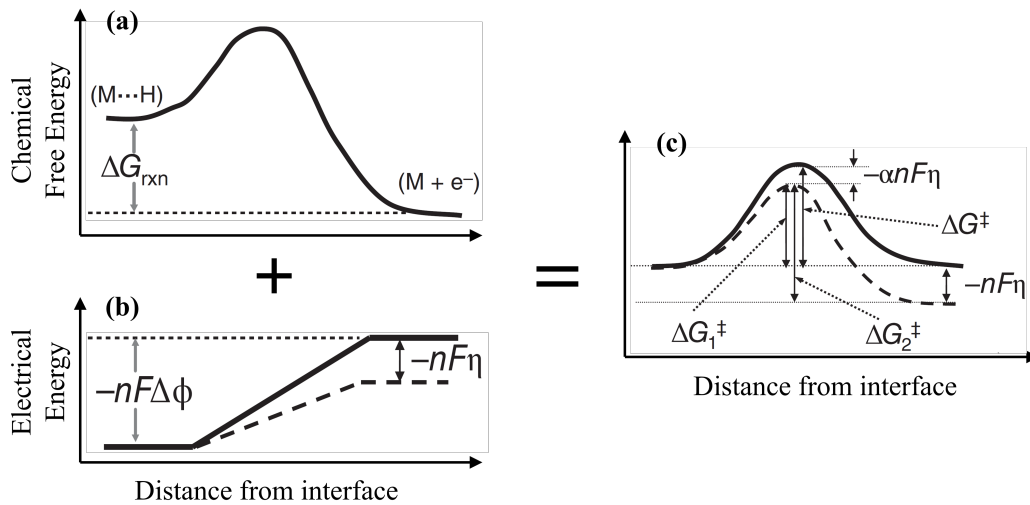
Figure 3.8: When the Galvani potential at the reaction boundary is lowered, it promotes the forward reaction over the reverse one. Even though the system's chemical energy (a) remains unchanged, adjusting the electrical potential (b) disrupts the balance between the energy barriers for the forward and reverse reactions (c). In the given diagram, decreasing the Galvani potential by η makes it easier for the forward reaction to occur while making the reverse reaction more challenging.

barrier. Called the transfer coefficient, α expresses how the change in the electrical potential across the reaction interface changes the sizes of the forward versus reverse activation barriers. The value of α is always between 0 and 1. For symmetric reactions, $\alpha = 0.5$. For most electrochemical reactions the range is from about 0.3 to 0.7 [102].

Fig. 3.8 is a detailed view of the interaction between the anode and the electrolyte. While the figure doesn't show the cathode–electrolyte interface, it would look quite similar to Figure 3.8. However, the voltage change at the cathode might differ in magnitude. For a comprehensive view of both anode and cathode interactions, refer to Fig. 3.9.

At equilibrium, the current densities for the forward and reverse reactions are both given by j_0. Away from equilibrium, The net current is obtained by the difference between the new forward and reverse current densities. By starting from j_0 and taking into account the changes in the forward and reverse activation barriers is possible to write the Butler-Volmer equation in Eq.(3.13).

$$j = j_0(e^{\alpha nF\eta/(RT)} - e^{-(1-\alpha)nF\eta/(RT)}) \qquad (3.13)$$

This equation assumes that the concentrations of reactant and product species at the electrode are unaffected by the presence of a net reaction rate. In reality, however, a net reaction rate will likely affect the surface concentrations of the reactant and product species. For example, if the forward reaction rate increases dramatically while the reverse reaction rate decreases dramatically, the reactant species surface concentration will tend
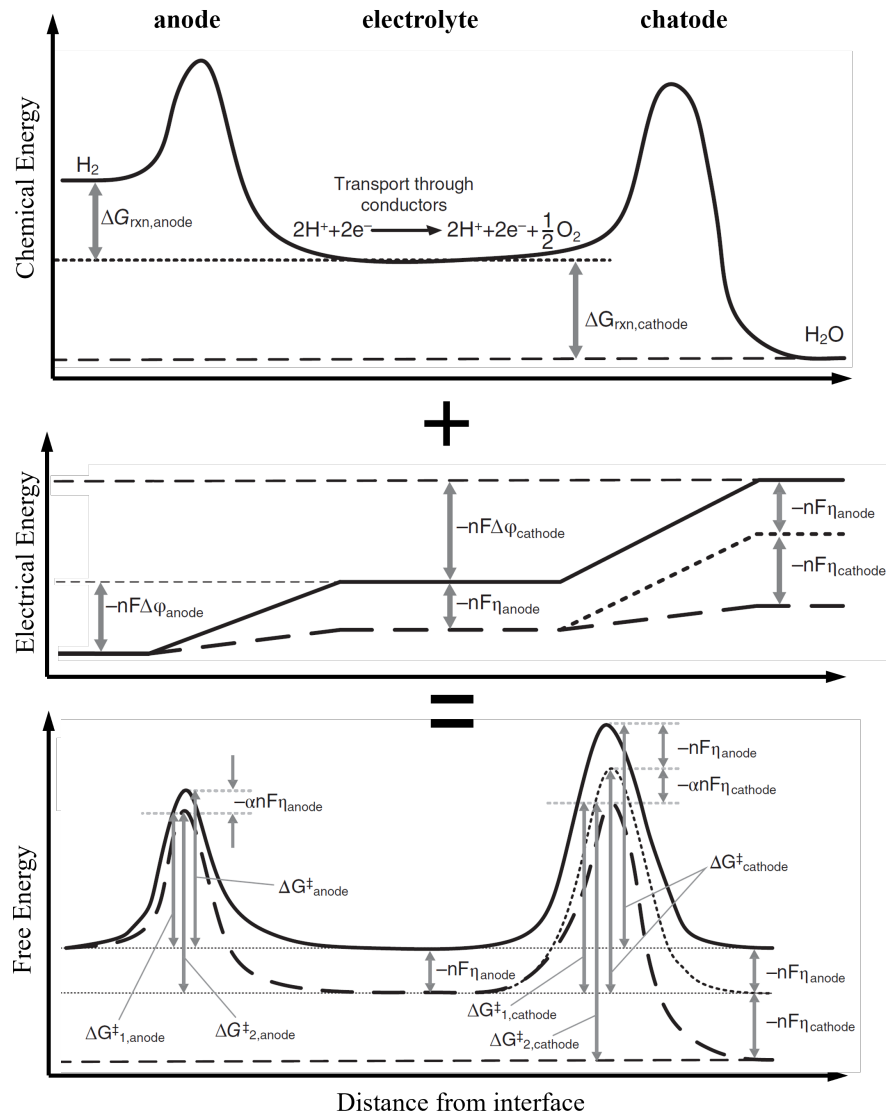
Figure 3.9: The overvoltage at the anode and the cathode modify the activation energy of each electrode according to the current. At steady state, the current at the anode and the cathode should be equal. Overvoltage and species concentrations are determined by satisfying this condition.

to become depleted.

The Butler–Volmer equation is fundamentally applicable only for single-electron transfer events. Nevertheless, it generally serves as an excellent approximation for most single-step electrochemical reactions, and even for multistep electrochemical reactions.

The loss η represents a voltage loss due to activation, it is typically called activation overpotential (V_{act}). For simple electrochemical systems, the Butler–Volmer equation studies variations in kinetic parameters such as α and j_0. As far as fuel cell performance is concerned, reaction kinetics induces a characteristic, exponentially shaped loss on a

fuel cell's polarization curve, as shown in Fig. 3.10.
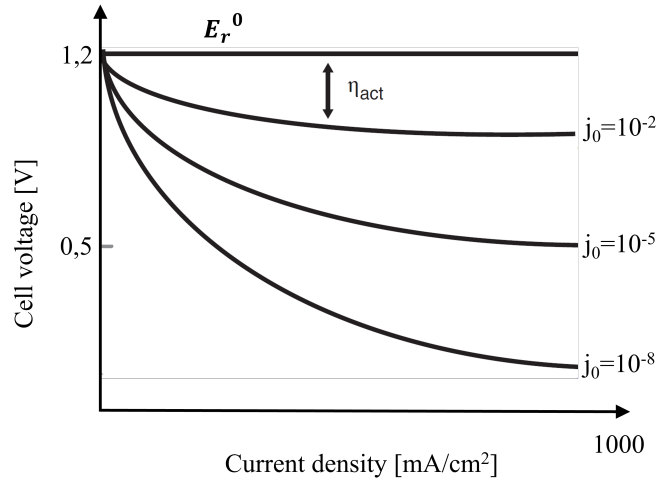
Figure 3.10: Effect of activation overvoltage (V_{act}) on fuel cell performance. Curves calculated for various j_0 values with $\alpha = 0.5$, $n = 2$, and $T = 298.15K$.

This curve was obtained by starting with E_r^0 and then subtracting the overpotential V_{act}. The functional dependence of V_{act} on j was given by the Butler–Volmer Eq.(3.13). The magnitude of the activation loss (V_{act}) depends on the reaction kinetic parameters. The loss especially depends on the size of j_0, as shown in Fig. 3.10.

The Eq.(3.13) can be simplified in the case of operating at $j << j_0$ or $j >> j_0$:

- $j << j_0 \longrightarrow$ Small V_{act}: less than about $15mV$ at room temperature, a Taylor series expansion of the exponential terms can be performed, as in Eq.(3.14). It indicates that current and overvoltage are linearly related for small deviations from equilibrium and are independent of α.

$$j = j_0 \frac{nFV_{act}}{RT} \tag{3.14}$$

- $j >> j_0 \longrightarrow$ Large V_{act}: greater than 50–$100mV$ at room temperature, the second exponential term in the Butler–Volmer equation becomes negligible. The forward-reaction direction dominates, corresponding to a completely irreversible reaction process, described by Eq.(3.15).

$$j = j_0 e^{\alpha nF(V_{act}/RT)} \tag{3.15}$$

Solving Eq.(3.15) in order to obtain V_{act} it is possible to write Eq.(3.16).

$$V_{act} = \frac{RT}{\alpha nF} \ln j_0 + \frac{RT}{\alpha nF} \ln j \tag{3.16}$$

The plot of V_{act} versus $\ln j$ is a straight line. If this equation is generalized in the form

it is known as the Tafel equation (Eq.(3.17), and b is called the Tafel slope. Interestingly, the Tafel equation came before the Butler–Volmer equation. It originated as a rule of thumb drawn from electrochemical studies. Only much later did the Butler–Volmer theory offer a foundational explanation for the Tafel equation.

$$V_{act} = a + b \ln j \tag{3.17}$$

Fuel cells operate in situations where large amounts of net current are produced. This situation corresponds to the case of an irreversible reaction process in which the forward-reaction direction dominates. Therefore, the second simplification of the Butler–Volmer equation (the Tafel equation) proves more useful in most discussions.

Fig. 3.11 displays a typical Tafel plot, which graphs V_{act} against $\ln j$ for an electro-chemical reaction. In areas of high overvoltage, the plot closely follows the linear Tafel equation. But when the overvoltage is low, the plot doesn't align perfectly with the Tafel approximation and instead veers towards Butler–Volmer kinetics. By examining the straight portion of this plot, you can determine values for j_0 and α.
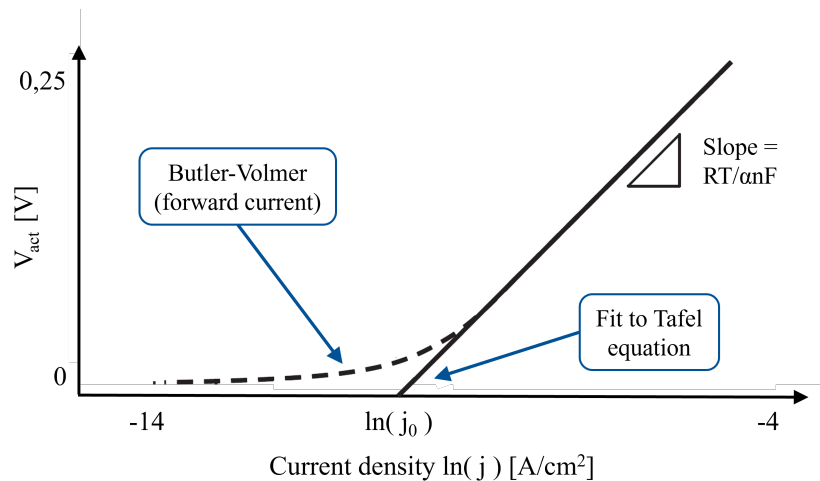
Figure 3.11: The fit of the kinetics to the Tafel approximation in order to determine j_0 and α.

3.3   Hydrogen Fuel Cell Charge and Mass Transport

Fuel Cell Charge Transport

Charged particles mainly come in two forms: electrons and ions. Since both electrons and ions are involved in electrochemical reactions, both types of charge must be transported. The transport of electrons versus ions is fundamentally different, primarily due to the large difference in mass between the two. In most fuel cells, ion charge transport is far more difficult than electron charge transport.

Charge transport requires potential energy to overcome the conductor's internal resistance. Consider the uniform conductor with constant cross-sectional area A and length L. Using the charge transport equation and Ohm's law it is possible to describe the relation between charge and voltage loss (V_{ohm}) due to the internal resistance R_i, as in Eq.(3.18).

$$V_{ohm} = i\left(\frac{L}{A\sigma}\right) = iR_i \tag{3.18}$$

The conductivity (σ) measures the propensity of a material to permit charge flow in response to an electric field. The potential V_{ohm} in represents the voltage that must be applied in order to transport charge at a rate given by i. Because this voltage loss obeys Ohm's law, it is called ohmic loss (V_{ohm}). Rewriting Eq.(3.18) including both the electronic (R_{el}) and ionic (R_{ion}) contributions to fuel cell resistance, we obtain Eq.(3.19).

$$V_{ohm} = iR_i = i(R_{el} + R_{ion}) \tag{3.19}$$

Because ionic charge transport tends to be more difficult than electronic charge transport, the ionic contribution tends to dominate. Fig. 3.12b illustrates the cell voltage decrease between the anode side of the electrolyte and the cathode side of the electrolyte to provide a driving force for charge transport, although overall fuel cell voltage increases from the anode to the cathode.

Fuel cell resistance exhibits several important properties. First, resistance is geometry dependent, as shown in Eq.(3.18). Fuel cell resistance changes based on its size. To compare fuel cells of varying sizes, we use resistances specific to their area. The resistance also depends on the fuel cell's thickness. That's why fuel cell electrolytes are usually made very thin. Moreover, the resistances from different parts of a fuel cell can be added together, just like connecting batteries in a series.

In PEMFC the ionic conduction happens through a polymer electrolyte membrane. The presence of fixed-charge sites and the presence of free-volume in the PEM allows good ionic conduction. n a polymer, there are fixed-charge spots. These spots should have the opposite charge to the ions that move around, ensuring the overall charge in the polymer stays balanced. In a polymer structure, maximizing the concentration of these charge sites is critical to ensuring high conductivity. However, the excessive addition of ionically charged side chains will significantly degrade the mechanical stability of the polymer, making it unsuitable for fuel cell use.

A polymer is not a solid block, but has small gaps or pockets, often referred to as "free volume." These spaces make it easier for ions to move through the polymer. The more gaps, the more the polymer can move and shift on a small scale. These small movements help ions move from one point to another in the polymer. These free-volume effects make polymer membranes high ionic conductive compared to other solid-state
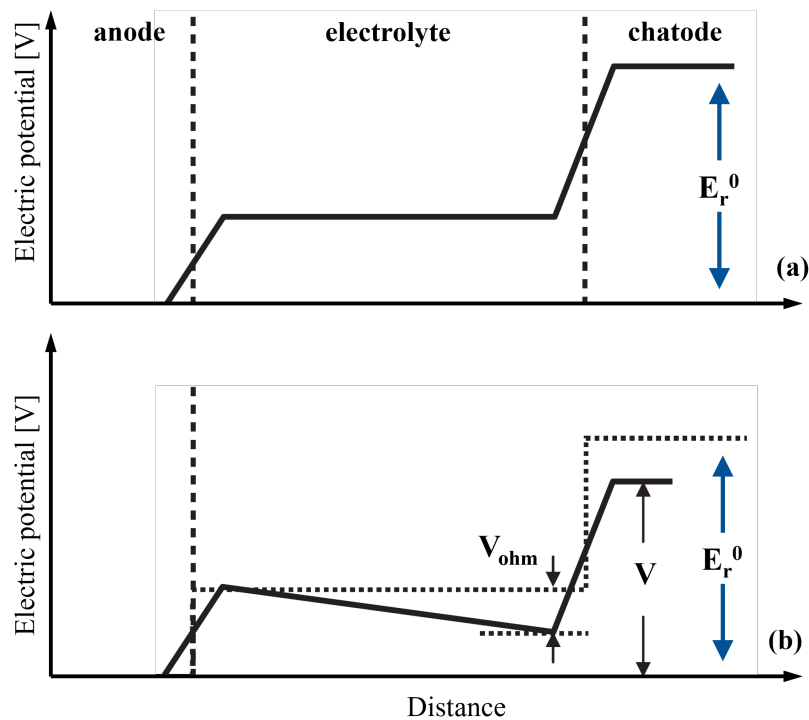
Figure 3.12: (a) The voltage profile of a fuel cell at thermodynamic equilibrium. (b) Effect of ohmic losses on fuel cell voltage profile.

ion-conducting materials, such as ceramics.

Polymer free volume also leads to another transport mechanism, known as the vehicle mechanism. In the vehicle mechanism, ions are transported through free-volume on certain free species, as in a vehicle. Water is a common vehicular species; as water molecules move through the free volumes in a polymer membrane, ions can go along for the ride, moving just like they would in a liquid solution. A popular material called Nafion, which is a type of persulfonated polytetrafluoroethylene (PTFE), uses this vehicle mechanism to achieve very high proton movement. Nafion is especially important for Proton Exchange Membrane Fuel Cells (PEMFCs).

Nafion is a material with a structure similar to Teflon but includes sulfonic acid (SO3–H+) groups. The Teflon part gives it strength, while the sulfonic acid chains allow proton movement. Nafion's structure has tiny interconnected pores lined with sulfonic acid groups. When water is present, protons in these pores form complexes and move away from the sulfonic acid chains. If there's enough water, these protons can move freely, like in a liquid. The Teflon part of Nafion repels water, which actually helps water move faster through the material. However, for Nafion to work this well, it needs to be kept wet, often by adding moisture to the gases used in the fuel cell.

Fuel Cell Mass Transport

The mass transport in the fuel cell happens in two different domains: in the electrodes and in fuel cell flow structures. The difference in length of these domains leads to a difference in transport mechanism. In fuel cells, the flow structures are usually measured in millimeters or centimeters. These structures have clear, defined channels that follow the laws of fluid mechanics. Gas transport in these channels is dominated by fluid flow and convection. On the other hand, fuel cell electrodes are much smaller, with features and gaps that are micrometers or even nanometers in size. These electrodes have a complex, winding design that protects gas molecules from the strong flow found in the larger channels. Sheltered from convective flow, gas transport within the electrodes is dominated by diffusion.

An electrochemical reaction on one side of an electrode and convective mixing on the other side of the electrode set up concentration gradients, leading to diffusive transport across the electrode. The electrochemical reaction leads to reactant depletion and product accumulation at the catalyst layer, as depicted in Fig. 3.13, where c_R^*, c_P^* represent the catalyst layer reactant and product concentrations, respectively, and c_R^0, c_P^0 represent the bulk, flow channel, reactant and product concentrations, respectively. This phenomenon affects fuel cell performance in two ways. The reversible fuel cell voltage decreases as predicted by the Nernst equation and the activation reaction rate losses increases.
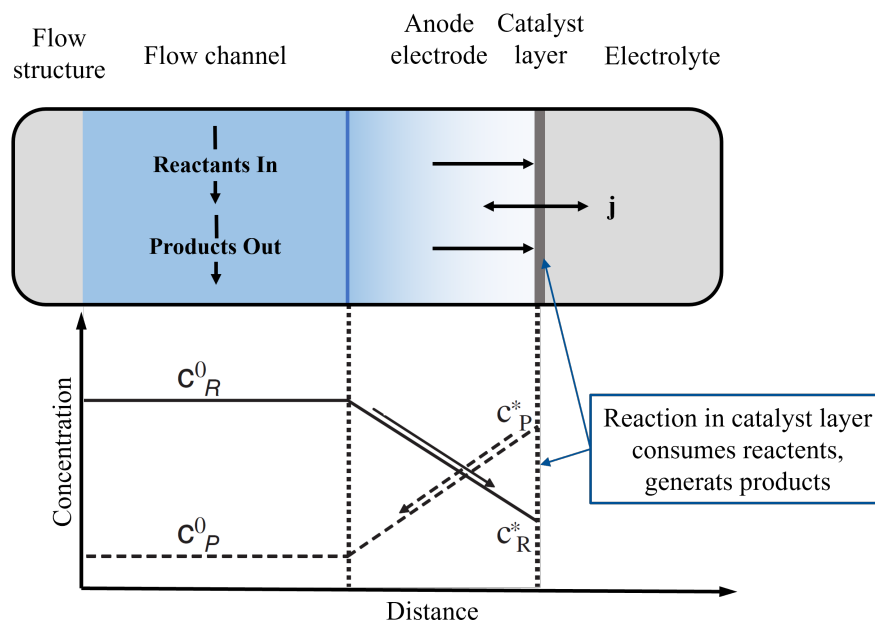
Figure 3.13: Schematic of mass transport situation within a typical fuel cell electrode.

In this context, when the reactant concentration in the catalyst layer drops all the way to zero represents the limiting case for mass transport. Defining δ as the electrode

thickness (usually 100-300μm), and D_{eff} as the effective reactant diffusivity within the catalyst layer (around $10^{-2} cm^2/s$), it is possible to obtain from Eq.(3.20) the value of the limiting current density (j_L). The fuel cell can never sustain a higher current density than that which causes the reactant concentration to fall to zero.

$$j_L = nFD_{eff}\frac{c_R^0}{\delta} \tag{3.20}$$

As mentioned above, the first way that concentration affects fuel cell performance is through the Nernst equation showed in Eq.3.8 and Eq.3.9. For simplicity, we will consider a fuel cell with a single reactant species, neglecting the product accumulation effects. Eq.3.21 describes the Nernst potential changes (V_{con}) due to reactant depletion in the catalyst layer (considering the difference between c_R^0 and c_R^*).

$$V_{con} = \left(E_r^0 - \frac{RT}{nF}\ln\frac{1}{c_R^0}\right) - \left(E_r^0 - \frac{RT}{nF}\ln\frac{1}{c_R^*}\right) = \frac{RT}{nF}\ln\frac{c_R^0}{c_R^*} \tag{3.21}$$

From Eq.(3.20) is possible to find c_R^0 as function of limiting current and derive the same for c_R^*, as depicted in Eq.(3.22).

$$c_R^0 = \frac{j_L\delta}{nFD_{eff}}, \quad c_R^* = c_R^0 - \frac{j\delta}{nFD_{eff}} \tag{3.22}$$

Thus, the ratio c_R^0/c_R^* can be written as in Eq.(3.23) and then substituting this result into Eq.(3.21) is obtained the formulation for V_{con} in case of Nernst potential loss as in Eq.(3.24).

$$\frac{c_R^0}{c_R^*} = \frac{j_L\delta/nFD_{eff}}{j_L\delta/nFD_{eff} - j\delta/nFD_{eff}} = \frac{j_L}{j_L - j} \tag{3.23}$$

$$V_{con,Nernst} = \frac{RT}{nF}\ln\frac{j_L}{j_L - j} \tag{3.24}$$

Another way concentration impacts fuel cell performance is by influencing the reaction speed. This is because the speed of the reaction is linked to the reactant and product concentrations at the reaction sites. In the high-current-density region, where the concentration effects become most pronounced the second term in the Butler–Volmer equation, Eq.(3.13), drops out and the expression simplifies to Eq.(3.25).

$$j = j_0\left(\frac{c_R^0}{c_R^*}e^{\alpha nFV_{act}/(RT)}\right) \tag{3.25}$$

As for Nernst potential loss, it is calculated he incremental voltage loss due to reactant depletion in the catalyst layer (V_{con}). In other terms, how much the activation overvoltage changes for c_R^0 and c_R^*. The Eq.(3.26) shows the V_{con} from Butler-Volmer formulation (BV).
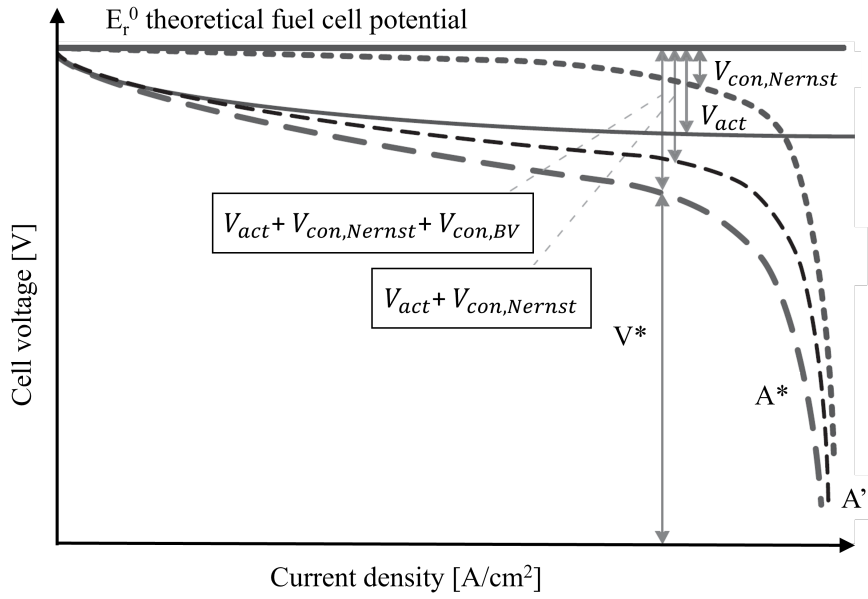
Figure 3.14: Concentration loss due to Nernstian effects and activation effects on the fuel cell polarization curve.

$$V_{con,BV} = \frac{RT}{\alpha nF} \ln \frac{c_R^0}{c_R^*} \tag{3.26}$$

Considering again the ratio c_R^0/c_R^* and substituting in V_{conc} expression is obtained Eq.(3.27) that provides almost the same final result as before. Where α is the transfer coefficient defined previously.

$$V_{con,BV} = \frac{RT}{\alpha nF} \ln \frac{j_L}{j_L - j} \tag{3.27}$$

The total loss due to reactant concentration is obtained by adding the contribution from reactant depletion and reaction kinetics as shown in Eq.(3.28).

$$V_{con} = V_{con,Nernst} + V_{con,BV} = \frac{RT}{nF} \left(1 + \frac{1}{\alpha}\right) \ln \frac{j_L}{j_L - j} \tag{3.28}$$

Fig. 3.14 shows the concentration loss due Nernstian effects and activation effects on the fuel cell polarization curve. The new activation curve A^* accounts for additional kinetic losses due to the decreasing catalyst surface concentration with increasing current density. The difference between A^* and A' represents the concentration loss induced by reaction activation $V_{con,BV}$.

Fuel cell flow structures are designed to distribute reactants across a fuel cell. Perhaps the simplest flow-structure would be a single-chamber, the entire fuel cell anode in a single compartment, then introduce H_2 gas. This design would lead to poor fuel cell performance. The H_2 would tend to stagnate inside the chamber, leading to poor

reactant distribution and high mass transport losses.

In real fuel cells, to avoid these issues, they use detailed flow structures with many tiny channels. These channels ensure that reactants keep moving, promoting even distribution and mixing. This design also offers more points for collecting the electrical current from the fuel cell.

To create these structures, designs are often stamped or carved into a plate. The channels, which can be numerous, are designed in intricate patterns, ensuring gas flows smoothly from one end to the other. To understand how gas moves in these complex designs, computer simulations, like computational fluid dynamics (CFD) modeling, are used.

Chapter 4

The Holistic Approach to Preliminary Design

Holistic design is a design approach that considers the system being designed as an interconnected whole which is also part of something larger. Holistic concepts can be applied to architecture as well as the design of mechanical devices, the power system design, and so forth. This approach seeks to identify and address potential interactions, synergies, and conflicts between components to achieve optimal performance, efficiency, and reliability. This approach is rooted in the teachings of Aristotle in his work Metaphysics (384–322 B.C.), emphasizing the interconnection of all things. The term Holism is derived from the Greek word *holos*, which translates to *whole* or *entire*. It suggests that a system, whether it's physical, biological, chemical, or any other type, should be perceived as a complete entity rather than just individual components. This concept is evident in nonlinear mathematical systems and is a foundational principle in systems theory.

Transitioning to a truly net-zero energy system is a hugely complex task. A comprehensive strategy is essential, examining how our infrastructure interacts with and consumes energy. This strategy should also evaluate how energy is generated, transferred and utilized. Reconfiguring the grids and systems and rethinking how we match supply and demand involves a holistic view of the inter-relationship between how energy is sourced, transferred and utilized.

Hybrid power generation systems are designed to share the load with the utility grid and transmit power to remote areas, combining different power sources such as photovoltaic systems (PV), wind turbines, gas turbines, storage batteries, diesel generators, and fuel cells (FC). The importance of hybrid power generation systems lies in their ability to classify and combine these power sources in various configurations. A holistic approach to hybrid power system design involves different combinations of power sources and their integration to meet specific energy requirements. This approach requires a comprehensive understanding of the characteristics and capabilities of each

power source, as well as their integration and control within the hybrid power system.

Association of Southeast Asian Nations (ASEAN) are signatories to the Paris Agreement and have pledged to reduce their greenhouse gas emissions to limit the rise in atmospheric temperature to less than $2°C$ from pre-industrial times. In Lau H.C. (2023) [105] discusses an ASEAN project to identify technologies with the greatest potential to reduce carbon emissions in the power sectors of ten ASEAN countries and to derive relevant policy insights. Decarbonization technologies are screened for each country using a holistic criterion which includes sustainability, affordability, security, reliability, readiness and impact. A broader perspective on decarbonization is offered by suggesting policy guidelines that can be applied across multiple nations.

4.1   The Holistic Approach to Ship Conceptual Design

In ship design, it's essential to view it as a comprehensive system made up of various interconnected subsystems. These include areas like cargo storage and handling, power generation, propulsion, crew accommodation, and navigation. Each of these subsystems serves specific functions on the ship. Broadly, these functions can be categorized into two groups: payload functions and inherent ship functions. For ferry ships, payload functions deal with cargo space, handling, and treatment equipment. Inherent functions, on the other hand, focus on safely transporting the cargo from one port to another at a specified speed. Furthermore, effective ship design should consider the entire life cycle of the ship. This life cycle can be broken down into stages: initial concept and preliminary design, detailed contractual design, the actual construction process, the operational phase, and finally, scrapping or recycling. The goal is to optimize the design across all these stages, ensuring the ship is efficient throughout its entire lifespan. It's worth noting that each stage of the ship's life cycle presents its own set of challenges and requires a balanced approach to design, considering various constraints and objectives.

The concept of a holistic approach to ship design was introduced more than 10 years ago by Papanikolaou A. (2010) in [106]. The paper provides an introduction to the holistic approach to ship design optimization, describing the generic ship design optimization problem and discussing its solution by use of GAs and related techniques for design generation, exploration and selection. The methodology is further explained using two specific examples: optimizing the shape of high-speed vessels to minimize power usage and environmental effects from wave wash and improving roll-on roll-off (Ro-Ro) ferries to reduce structural weight, increase transport capacity, and ensure better safety during collisions.

The importance of holistic ship design was established with the European project *HOLIstic optimisation of SHIP design and operation for life cycle* (HOLISHIP) [107]. The HOLISHIP project focused on advanced ship design methods that consider a ship's entire life cycle. It successfully integrated various design factors, as depicted in

Fig. 4.1, including technical requirements, performance metrics, costs, and environmental impacts, from the initial stages of design. To bring this vision to life, the project developed integrated software platforms tailored for design purposes.

Figure 4.1: Diagram of the fields where HOLISHIP focuses its objectives

The efficiency of these platforms was showcased through digital models and real-world case studies, led by industry experts, which covered the design and efficiency of ships, marine tools, and other maritime resources [108].

The methodology and the results of the HOLISHIP project were discussed in several scientific papers as [109] and [110]. Tools and system data from all disciplines are integrated by design synthesis in the platform, which allows a concurrent analysis and optimization of systems and components in contrast to the sequential/iterative approach used in the classical design spiral. The holistic design approach adopted in HOLISHIP, to model the machinery system, is indicated in the following Fig4.2, as reported in the book [111].

In the HOLISHIP context, Skoupas S. et al. (2019) in the work [112] presents a parametric design optimization of two ferry ships. The paper focuses on the holistic optimization of high-speed Ro-Ro Passenger ships, considering various ship systems. These systems include the hullform, internal layout, propulsion, transport capacity, economic viability, intact stability, and damage stability. The NAPA software environment is used to automatically elaborate these ship systems and enable the multi-objective optimiza-

Step 1	**High Level Conceptual Design** Definition of main consumers based on mission requirements and high level vessel design.
Step 2	**Power system concept design and optimization** Definition and optimization of power system architecture, main components and control strategy based on operational profile and KPIs
Step 3	**Power system concept verification** Verification of power system performance based on dynamic simulation of operational scenarios

Figure 4.2: Diagram of design approach involved in the HOLISHIP project

tion of design alternatives. The optimization process takes into account factors such as installed propulsive power, design constraints, and objectives related to each ship system.

4.2 The Proposed Methodology

Scientific research and investment in projects such as HOLISHIP have produced advances in ship design, in terms of methodology and results. The shipbuilding industry and system integrators have the appropriate resources to achieve the goals marked by the energy transition. However, within the shipbuilding framework, there are many companies that militate in this context by providing a more specific service. The clearest examples are companies that design and manufacture power generation or energy storage systems, which are more unrelated to the direct design of the ship than those dedicated to the hull and propeller (much more often integrated by the shipowner). For this reason, several companies supply their products to different sectors, other transportation or stationary. The same approach followed in the HOLISHIP project is very inefficient if the target is only one part of the entire vessel since it considers all components with the same degree of complexity. However, this does not mean that the benefits from the holistic approach cannot be useful in the design of the individual component.

In the maritime sector alone, the diversification of applications is enormous, and in the transportation and power generation sector in general, taking the user's needs into account has become increasingly complex. In addition, customer satisfaction is followed by legislative constraints regarding pollutant emission and efficiency.

The holistic approach to design, in this case of preliminary/conceptual design, is based on taking a bird's eye view of all the interconnections between components and between different systems in order to improve the efficiency of the design process and the final product. In the presented project, the central object is the PEM fuel cell. A very

expensive power generation system, as reported in the previous chapters. Thus, saving resources during design while improving the efficiency of the system, once it is integrated and operative, is a key objective in order to spread this technology and facilitate the transition to zero-carbon solutions.

A similar approach was employed by Harenbrock M. et al. (2020) in [113] to design an innovative cathode air supply for a PEMFC in the automotive sector. The entire fuel cell system is considered holistically in order to optimize acoustic performance, decrease air inlet losses at the cathode, and reduce parasitic losses.

In the early stages of design, basic models are used to select the overall structure and size components. These models are simple and focus on static or near-static conditions. However, as the design progresses and needs verification under various operational scenarios, more detailed models are essential. These models must simulate real-time conditions, including dynamic loads, and should incorporate key control systems.

The proposed methodology focuses on the feasibility study of the PEMFC but considers all the major systems of the vessel and their interconnections. Then, the modeling of each component considers the degree of connection with the FC to assess the level of complexity to be used. Fig. 4.3 summarizes the components considered in the design and the level of complexity employed to integrate them into the model.
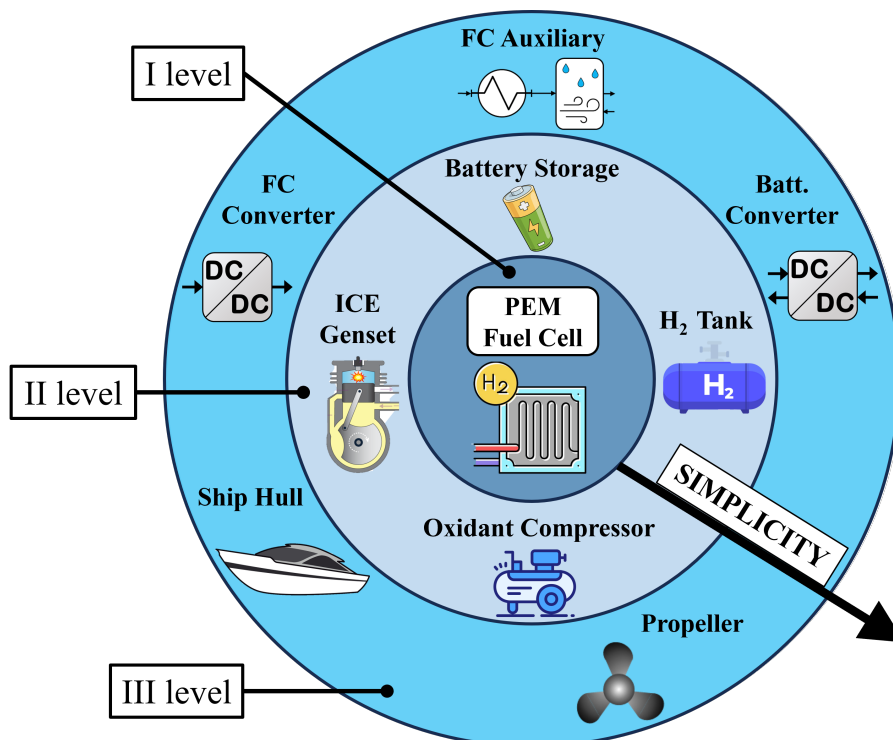
Figure 4.3: The proposed holistic preliminary design concept.

At the first level, the focus of the study is the PEM fuel cell model. This simulates the behavior of the cell from the thermodynamic and electrochemical perspectives. The

model, once calibrated to the polarization curve of a real fuel cell, was validated in static and dynamic performance. The thermal management approach used for the given PEMFC system relies on two main factors: the excess ratio of the oxidizer and the amount of liquid water introduced into the oxidizer. The addition of liquid water is crucial to maintain the humidity of the cell membrane.

The second level is marked by reduced detail in the modeling compared to the first level, prioritizing information that may influence the behavior and integration of the fuel cell into the powertrain, but still managing to provide important insights into the optimal sizing of these components. The compressor model allows for the estimation of the power input taking into account the oxidizer used, the operating pressure, the flow rate processed, and the efficiencies related to the compressor and the prime mover connected. This model is at a higher level of complexity than the other PEMFC auxiliaries because it has a more obvious influence on gross performance. The proposed PEMFC model exploits a meta-model in order to predict the degradation of the cell during operation, this succeeds in providing important insights into the sizing of the on-board hydrogen tank. In addition, fuel consumption can be optimized through the proposed optimization framework. The battery storage model allows the storage system to be sized based on actual usage during missions. Battery performance is considered as a function of the State of Charge (SOC), or residual capacity, differentiating between a charge and discharge curve. The simulation framework includes the possibility of adding or replacing the battery with a Variable Speed Diesel Engine Generator (VSDEG). The VSDEG model takes into account the dynamics of the diesel engine and was validated on experimental data of the VL1716C2-MLL engine produced by Isotta Fraschini Motori SpA. Engine performance has been optimized by varying the frequency at which to deliver power in order to improve specific fuel consumption. In addition, the model features a fuel consumption estimation algorithm based on the experimental fuel consumption data for the operating limit curve.

The third level is the external one, and within it are considered elements that are certainly important, such as the converter between the fuel cell and the ship's electrical grid, but that influence the performance of the fuel cell just through their operating efficiency. These components are: the unidirectional converter of the FC, the bidirectional converter of the battery, and the remaining auxiliary systems of the FC (intercooler downstream of the compressor and the oxidizer humidity control system) considered as losses function of the power delivered by the powertrain.

Finally, the simulation framework includes the possibility of conducting the study for a refit or for a new vessel. Indeed, the model, in the case of refit of an existing vessel, requests as input the overall power profile required during the mission as a function of time. In the case of a new design, this data history would not be available, so an estimation of the power system power requirement is proposed by modeling the displacement hull and propeller. The resistance to hull motion is calculated as a function
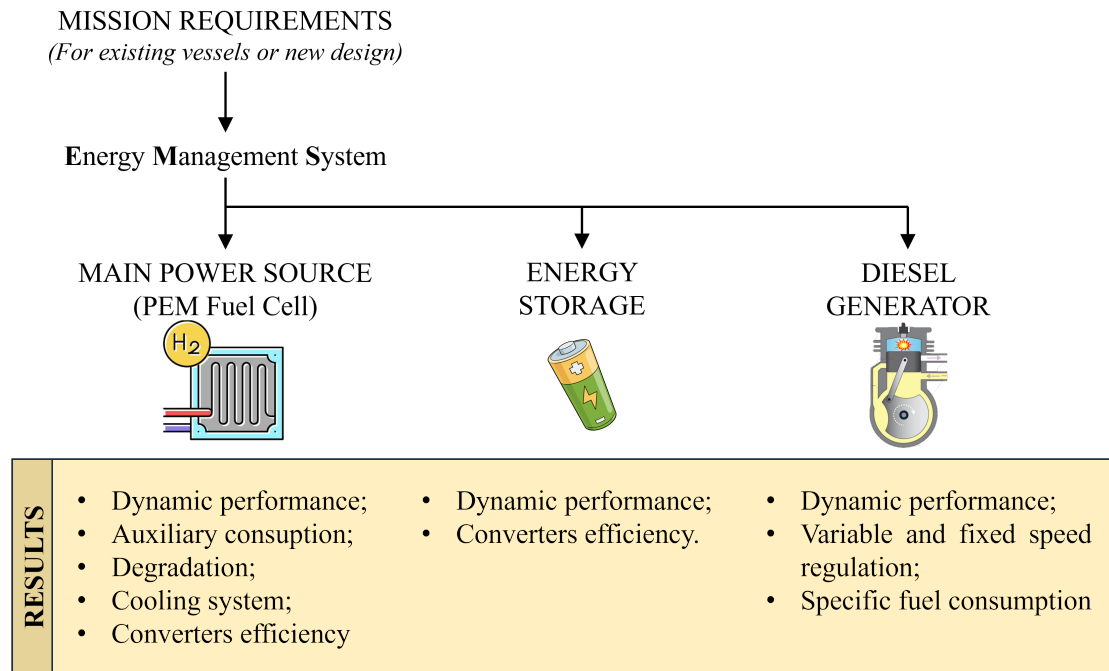
Figure 4.4: The schematic of the simulation environment related to the proposed design methodology.

of ship speed from geometric data using the systematic series of Admiral Taylor and naval architect Gertler (1919). Whereas, the estimation of propeller torque and thrust coefficients considers the basics of propeller system design and exploits Wageningen's B propeller series (1960). Thus, the model allows propulsive load estimation even for a new ship design. The proposed modeling for new ship design integration is presented in Appendix A.

The Energy Management System (EMS) is also important to be included in the sizing of various components. EMS allows the integration of multiple renewable energy sources and backup systems, which helps overcome the drawbacks of intermittency and ensures a continuous supply of power. EMS helps optimize the size of components and adopt an energy management strategy, leading to a decrease in the overall cost of the system and minimizing negative effects.

When modeling a machinery component, it's vital to focus on properties relevant to the specific design task. For instance, energy efficiency and loss factors are crucial for basic optimization, while dynamic simulations might prioritize properties like machinery inertia and available control system sensors.

The design process also requires a clear understanding of the ship's operational profile. Some ships have straightforward profiles, like constant-speed sailing and port maneuvers. Others, like offshore vessels, have complex profiles involving various tasks like towing, positioning, and idling. This profile outlines the ship's primary tasks and the time spent on each, considering factors like speed, operational areas, and weather condi-

tions. It's also essential to determine the energy consumption for each task. Depending on the ship type, this profile can be time-dependent or summarized over a year. When incorporating energy storage and shore power, it's vital to assess the profile in real-time to maximize the benefits of energy storage in optimization.

Fig. 4.4 describes the developed simulation environment. Mission requirements, in terms of power demand, can be provided as input or obtained through propulsion system and hull simulation. The Energy Management System considers the fuel cell as the main power source and uses energy storage or the diesel engine to meet the power demand.

Being able to quickly simulate long periods of fuel cell utilization, while operating on board, allows the fuel cell configuration to be designed and implemented for different applications, while maintaining very high system efficiency.

Chapter 5

The Proposed Model

This chapter describes the methodology used to model the different components of the ferry power system. Fig. 5.1 shows the schematic of the proposed zero-emission ferry. The main power source is the PEM fuel cell system. The battery energy storage operates to obtain a peak shaving of the FC power demand and ensures electrical power to the ship grid allowing the correct dynamic operation of the PEMFC stacks. The online Energy Management Systems (EMS) select the operative mode taking into account the vessel's power demand and the battery SOC and choose when and how to exploit the power available to the shore (cold-ironing mode). The electrical drives connected to the propellers and the hotel loads represent the power demand of the studied system.

This chapter discusses the modeling of the variable speed diesel generator (VSDEG), although optional in the model. VSDEG technology is crucial for the efficient integration of new ICE generators into the ship's direct current (DC) network. The results shown present the operational advantages of using VSDEGs instead of fixed-speed generators in terms of efficiency and fuel consumption. However, because the case study examined does not involve the use of diesel generators, in order to be zero-emission, it is not present in the final simulations, but its modeling is reported for possible integration into the powertrain or used to provide indications of emissions and fuel consumption savings.

5.1 The Modeling of PEM Fuel Cell System

The proposed cell reduced-order model simulates the system from an electrochemical and thermodynamic perspective. The model provides also an evaluation of the power absorbed by the oxidizer compressor and auxiliaries. The thermal management strategy applied for the presented PEMFC system is based on the oxidizer stoichiometric excess ratio and the liquid water injected in the oxidizer. The latter is fundamental to ensure the cell membrane humidity. In addition, a degradation estimation model was implemented. PEMFCs have a shorter operational lifetime than marine diesel engines due to various factors that can influence the rate of degradation.
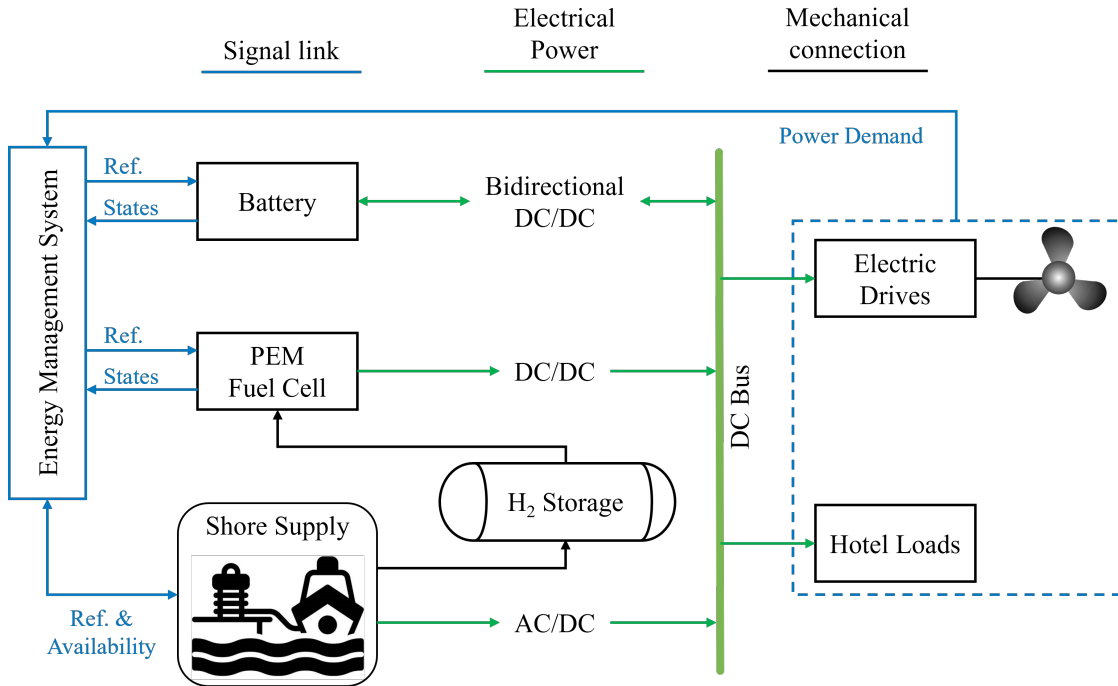
Figure 5.1: The schematic of the proposed zero-emission ferry considering the propulsion system, the power generation system and the energy storage.

The presented PEMFC power system model was developed in the Matlab-Simulink environment. The mathematical model of the single cell and the potential losses (overpotentials) associated with its operation are described, followed by a presentation of the control loop implemented. The proposed model was calibrated on 150kW Ballard FCvelocity PEM fuel cell available data, the Fig. 5.2 shows the single FC stack. Effective data and methodology were extracted from the fuel cell datasheet and the results, proposed by Li et al. in 2015 [75], on the comparison between experiments and simulations.

The performed model calibration involved a sensitivity analysis in order to evaluate the best values for the customizing variables. In order to prove the validity of the PEMFC power unit model the test proposed by Li et al. in 2015 was replicated [75].

Next, the method used to estimate the fuel cell degradation under different operating conditions is illustrated. The mass and energy balance equations are discussed. Finally, models related to the fuel cell stack and the power required by the auxiliaries are presented.

5.1.1 The Single Cell Model

A fuel cell is an electrochemical cell that converts the chemical energy of a fuel into electricity. Hydrogen is oxidized at the anode and oxygen is reduced at the cathode. Protons are transported from the anode to the cathode through the electrolyte membrane, while electrons travel to the cathode over the external circuit. On the cathode, oxygen reacts

P$_{rated}$: 150 kW

Fuel: Gaseous H$_2$ – Commercial grade SAEJ2719

Weight (dry): 404 kg

Length x width x heigth: 1530 x 871 x 495 mm

DC voltage: 465-730 V

Maximum current: 300 A

Nominal operating temperature: 63 °C

Number of cells: 762

Cell active surface: 500 cm^2
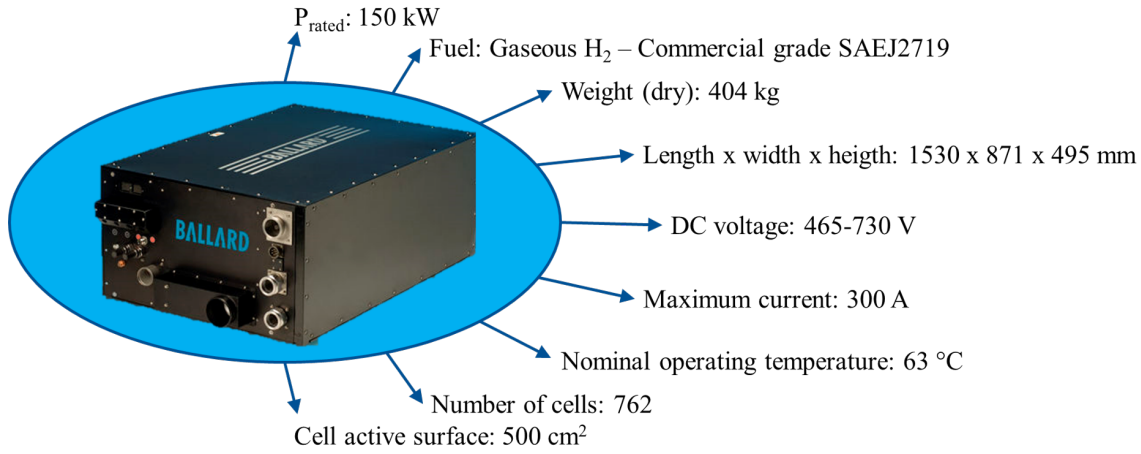
Figure 5.2: The $150kW$ Ballard PEMFC stack $FCvelocity - HD6$.

with protons and electrons to form water and produce heat. Both electrodes contain a catalyst to speed up the electrochemical processes.

A typical PEM fuel cell operates according to the following reactions, shown in Eqs. (5.1), (5.2) and (5.3):

$$\text{Anode: } H_2(g) \rightarrow 2H^+(aq) + 2e^- \tag{5.1}$$

$$\text{Cathode: } \frac{1}{2} O_2(g) + 2H^+(aq) + 2e^- \rightarrow H_2O(l) \tag{5.2}$$

$$\text{Overall: } H_2(g) + \frac{1}{2} O_2(g) \rightarrow H_2O(l) + Electric\ Energy + Waste\ Heat \tag{5.3}$$
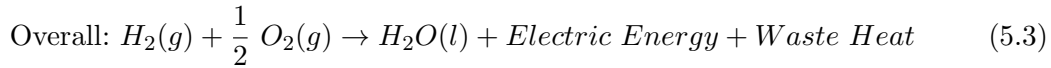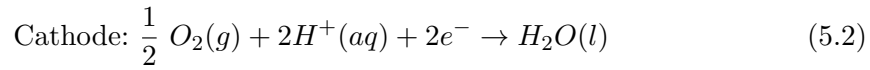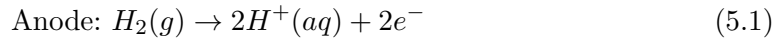
The fuel cell layers are the Proton Exchange Membrane PEM, gas diffusion and catalyst layers. These layers are assembled together and are called the membrane electrode assembly (MEA). A stack with many cells has MEAs positioned between bipolar flow field plates and only one set of end plates. The maximum amount of energy generated in a fuel cell corresponds to the variation in Gibbs free energy, ΔG, then the theoretical potential of the fuel cell, E_r, is shown in Eq.(5.4). E_r^0 is the potential when the fuel cell is not connected to the electrical circuit; when the fuel cell has the circuit closed, there are different kinds of voltage losses caused by several phenomena.

$$E_r^0 = \frac{-\Delta G^0}{nF} \tag{5.4}$$

F is the Faraday's constant and n is the number of electrons involved in the reaction, for the presented reaction is two. E_r at standard conditions of $25°C$ and pressure of $1atm$ is equal to $1.229V$ given by the Nernst equation, Eq.(5.5). The reversible Nernst

potential is a function of pressure and temperature.

$$E_r = E_r^0 - \frac{\Delta S}{nF}(T_{op} - T_{rif}) + \frac{RT_{op}}{nF} \ln\left(\frac{p_{H_2}\ p_{O_2}^{0.5}}{p_{H_2O}}\right) \tag{5.5}$$

Where ΔS is the entropy variation of the system, T_{op} is the operating temperature of the cell, T_{rif} is the reference temperature (298.15K), R is the universal elastic gas constant and the partial pressures (p_{H_2}, p_{O_2}, p_{H_2O}) replace the activities of hydrogen and oxygen gases [102].

As expressed before, there are three kinds of losses (or overpotentials) which make the cell voltage decrease during its operation (i.e. activation, ohmnic and concentration overpotentials). The voltage of the single fuel cell V_{cel} is express by Eq.(5.6).

$$V_{cel} = E_r - V_{act} - V_{ohm} - V_{con} \tag{5.6}$$

In order to activate a reaction, it is necessary to exceed the limit of the activation energy. The Activation losses, V_{act}, represent the difference from the equilibrium that is needed to get the reaction started, and this is mainly due to electrode kinetics; these losses happen at both the anode and cathode side.

At the equilibrium the net reaction rate is zero, both forward and reverse reactions are taking place at a rate which is characterized by the exchange current density, j_0; this is called dynamic equilibrium. When the cell operates at the current density, j, greater than j_0 the forward-reaction direction dominates, corresponding to a completely irreversible reaction process. The Butler–Volmer Eq.(5.7) described in [76] relates j and j_0. In Eq.(5.7), α is the transfer coefficient which expresses how the change in the electrical potential across the reaction interface changes the sizes of the forward versus reverse activation barriers.

$$j = j_0 e^{\alpha nF(V_{act}/RT_{op})} \tag{5.7}$$

The value of the transfer coefficient (α) is always between 0 and 1. For symmetric reactions, $\alpha = 0.5$. For most electrochemical reactions, α ranges from about 0.3 to 0.7 [114]. During operating conditions, the fuel cell produces large amounts of net current. This corresponds to an irreversible reaction process where the forward reaction dominates. By solving Eq.(5.7), we can express the activation overpotential using Eq.(5.8).

$$V_{act} = \frac{RT_{op}}{\alpha nF} \ln\left(\frac{j}{j_0}\right) \tag{5.8}$$

Eq.(5.8) is known as the Tafel equation. The Tafel equation was proposed before the Butler–Volmer equation (it was first developed as an empirical law based on electrochemical observations). It was only much later that the Butler–Volmer kinetic theory provided

an explanation for the Tafel equation from basic principles [102]. The Ohminic losses, V_{ohm}, are related to the resistance in the electrolyte to the flow of electrons through the electrically conductive fuel cell components, such as bipolar plates and gas diffusion layers (contact resistance). The losses can be expressed with Ohm's law in Eq.(5.9), where R_i is the fuel cell equivalent resistance and A is the cell reaction effective surface, typically measured in cm^2.

$$V_{ohm} = jAR_i \tag{5.9}$$

The limiting current density, j_L, of a fuel cell represents the maximum current that can be delivered by the cell. This represents the limiting case for mass transport, and it occurs when the reactant concentration on the surface of the cell falls to zero due to a large current density. The limiting current density is the ultimate mass transport limit for a fuel cell. However, concentration losses can still occur at lower current densities. These concentration differences in the catalyst layer affect fuel cell performance by decreasing the Nernst voltage and increasing the activation loss. Both these effects lead to the same result, which is referred to as the fuel cell's concentration overvoltage, V_{con} [102], [114]. V_{con} was obtained by equation Eq.(5.10).

$$V_{con} = \frac{RT}{nF} \left(1 + \frac{1}{\alpha}\right) \ln \left(\frac{j_L}{j_L - j}\right) \tag{5.10}$$

In order to emulate the real behaviour of a fuel cell, V_{con} is often multiplied by an empirical factor in order to improve the results obtained by the cell model at high current densities [102]. For proposed results this gain factor has been set to one. Finally, from Eq.(5.6) it is possible to obtain the polarization curve that relates the voltage output of the fuel cell for a given current density loading.

Fig. 5.3 shows the control loop for the direct current produced by the fuel cell, i. Therefore, the control system is performed by evaluating the error of the actual cell power delivered, P_{cel}, with respect to the reference cell power demand, $P_{d,cel}$. P_{cel} is obtained from the product between the current and the potential given by the polarization curve.
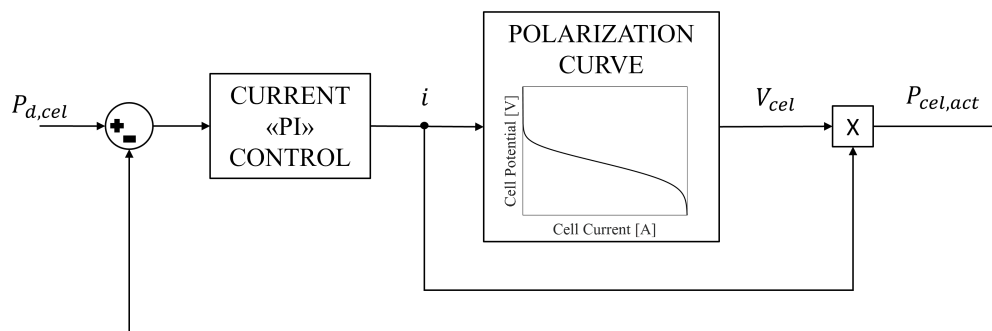
Figure 5.3: Block model structure of the Fuel Cell current control loop.

The Bode plot, a fundamental tool in control system design and analysis, visually represents a system's frequency response by plotting its magnitude and phase against frequency on a logarithmic scale. Comprising two plots, the magnitude plot depicts how much a system amplifies or attenuates input signals at various frequencies, while the phase plot shows the phase shift introduced by the system at those frequencies.The phase and gain margins, derived from the Bode plot, are critical indicators of system stability. Fig. 5.4 shows the Bode plot for the presented closed loop control and the results of the stability analysis in gain and phase margin, both passed.
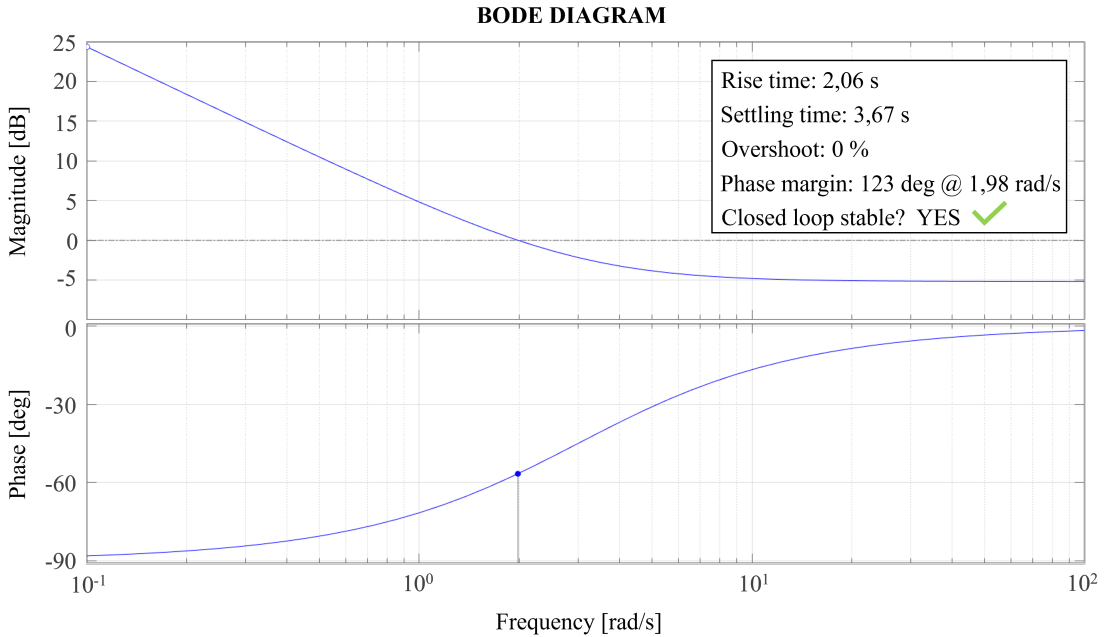
Figure 5.4: The Bode diagram, in Magnitude and Phase, for the current control loop.

The current, i, and the cell voltage, V_{cel}, are observed during the simulation, so that the simulation is terminated if the conditions shown in Fig. 5.5 are not fulfilled. Hence, the current output must not exceed the current threshold I_{Lim} and V_{cel} must be between the values $V_{Lim,low}$ and $V_{Lim,up}$. These threshold values can be set by the user according to the datasheet.

5.1.2 The Degradation Model

The degradation of proton exchange membrane (PEM) fuel cells is a critical challenge in their practical applications. Degradation can occur in various components of the fuel cell, including the electrocatalysts for oxygen reduction reaction (ORR) at the cathode and hydrogen oxidation reaction (HOR) at the anode. Factors such as fuel/air impurities, harmful species during catalyst preparation and use, and catalyst decomposition during operation contribute to degradation [115]. Environmental influences, particularly temperatures below freezing, can also affect the performance and long-term stability of
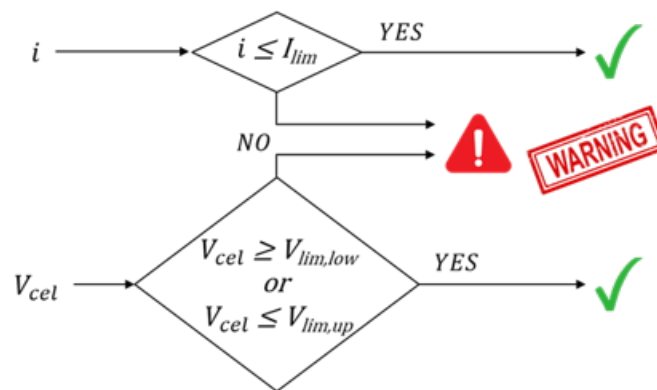
Figure 5.5: Fuel Cell safety performance thresholds.

PEMFCs. These influences can lead to changes in the catalyst layers and a reduction of its thickness, ultimately impacting the fuel cell's performance. In [116], the authors characterize three different MEA, estimating performance and degradation for a stress cycles between 80 and -10$°C$. Fig. 5.6 shows the results presented by Fan L. et al. (2021) in [117] about the degradation of the MEA of a PEMFC under DEAC mode, where the generated water can't be fully removed and then accumulated in the channels, causing a local high voltage to accelerate carbon corrosion or Pt dissolution, thereby influencing the performance of PEMFCs.
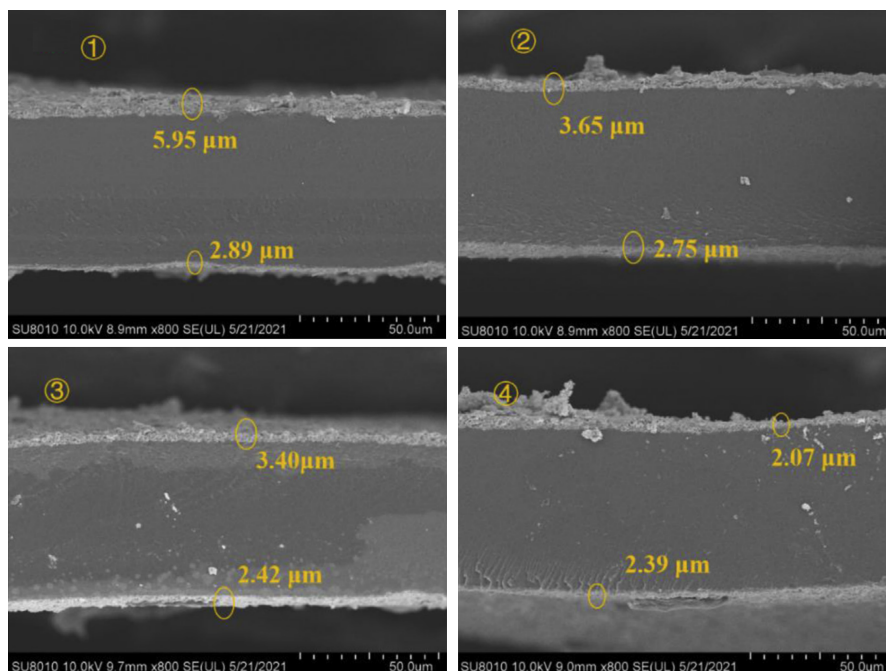
Figure 5.6: SEM images of the MEAs before and after 100 h continuous operation under DEAC mode (Pt black MEA), proposed in [117].

PEMFCs have a shorter operational lifetime than marine diesel engines due to factors such as power transients, cycling, and loading conditions that can influence the rate of

degradation. Given the high production costs of PEMFCs, it is important to consider their degradation characteristics during both the design and operating phases of a ship to achieve optimal cost performance. Quantifying the voltage degradation rate under each operating condition ideally requires extensive testing of individual fuel cells. However, this can be time-consuming. Fortunately, a reasonable estimate can be made using the manufacturer's datasheet and previous literature [14], [87], [71]. The cell degradation, D_{cel}, over one load cycle can be estimate through Eq.(5.11).

$$D_{cel} = D_{low} + D_{high} + D_{transient} + D_{cycle} \tag{5.11}$$

where D_{low}, D_{high}, $D_{transient}$ and D_{cycle} are cell voltage degradation caused by low power operation (less than 80% of rated power), high power operation, power transient and start/stop cycling, respectively. Tab.5.1 describes the PEMFC single-cell degradation rates used in this study. These parameters may differ across different fuel cell types, depending on the design and actual operating parameters.

Table 5.1: PEM fuel cell degradation rates (per cell) for linear degradation estimation (data retrieved by [14]).

Operating Conditions	Deg. Rate	Unit
Low power (0-80% rated power)	10.17	$\mu V/h$
High power (80-100% rated power)	11.74	$\mu V/h$
Transient loading	0.0441	$\mu V/\Delta kW$
Start/stop	23.91	$\mu V/cycle$

The degradation model is implemented by a Matlab function, which requires as input the vector of the power produced by the cell over time along the mission, the sampling time-step and the rated power of the single cell.

5.1.3 The Stack and Auxiliary Model

In order to design the whole fuel cell system, including the cooling system, the proposed model not only estimates the performance of the cell from an electrochemical perspective but manage the reactant and water flow rate to thermal balancing the fuel cell. Therefore, the water mass and power balance between the inlet and outlet of the system are evaluated by Eq.(5.12)(5.13). In Eq.(5.13), P_{cel} is the output electric power produced by the PEMFC.

$$\dot{m}_{H_2O,In}^{Ox} + \dot{m}_{H_2O,Inject} + \dot{m}_{H_2O,gen} = \dot{m}_{H_2O,Out}^{Ox} \tag{5.12}$$

$$\dot{Q}_{H_2,In} + \dot{Q}_{OxIn} + \dot{Q}_{H_2O,In}^{Ox} + \dot{Q}_{H_2O,Inject} = \dot{Q}_{OxOut} + \dot{Q}_{H_2O,Out}^{Ox} + P_{cel} \tag{5.13}$$

The water supplied and that generated inside the PEMFC are expelled as vapor contained in exhaust, Eq.(5.12). From Eq.(5.12)(5.13) it is possible to find the required oxygen stoichiometric ratio and injected liquid water flow rate so that the outlet air is fully saturated and that no additional cooling or heating of the fuel cell is required. It is possible to maintain the desired operating temperature and have just enough water at the air outlet to avoid either flooding with liquid water or drying with dry air. In this configuration, the relative humidity of hydrogen, which is necessary to humidify the membrane from the anode channels, is neglected. Nevertheless, such a fuel cell would result in an extremely simple system, illustrated in Fig. 5.7, without requiring an external humidification and cooling system.
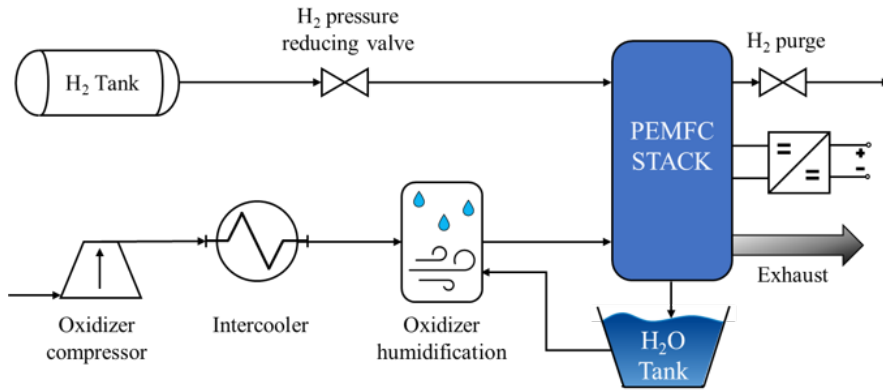
Figure 5.7: PEM Fuel Cell proposed system block diagram.

The presented work does not consider the dynamic on stack humidification. Nevertheless, as described in [118] the humidity regulation at different operating power can optimize the cell dynamic performance. Therefore, the dynamic on stack humidification will be implemented in the proposed model in order to improve the obtained results.

The parameters S_{H_2} and S_{O_2} are defined as the hydrogen and oxygen stoichiometric ratio, respectively. Then it is possible to calculate the flow rate of reactants and the generated water as a function of the current, i, by Eq.(5.14), where M_{H_2}, M_{O_2} and M_{H_2O} are the molar weights.

$$\begin{cases} \dot{m}_{H_2,In} = \dfrac{i}{2F} S_{H_2} M_{H_2} \\\\ \dot{m}_{OxIn} = \dfrac{i}{4F} \dfrac{S_{O_2}}{\chi_{O_2,in}} M_{Ox} \\\\ \dot{m}_{H_2O,gen} = \dfrac{i}{2F} M_{H_2O} \end{cases} \qquad (5.14)$$

The proposed model can simulate PEMFC operation either using pure oxygen or

air as oxidizer. Hence, the molar fraction of oxygen, $\chi_{O_2,in}$, could be set as shown in Eq.(5.15).

$$\chi_{O_2,in} = \begin{cases} 1 & \text{Oxigen as oxidizer} \\ \\ 0.2095 & \text{Air as oxidizer} \end{cases} \tag{5.15}$$

Through the temperature of the reactants at the inlet, T_{in}, and T_{op} the corresponding saturated vapor pressure, p_{vs}, is obtained. These and the relative humidity of the reactants, φ, are used to calculate the mass of vapor present in the oxidant supplied to the cell and that exhausted, respectively $\dot{m}^{Ox}_{H_2O,In}$ and $\dot{m}^{Ox}_{H_2O,Out}$ obtained from Eq.(5.16)(5.17). In the following formulas p_{ca} is the cathode supply pressure and p_{out} is the outlet pressure.

$$\dot{m}^{Ox}_{H_2O,In} = \frac{S_{O_2}}{\chi_{O_2,in}} \frac{M_{H_2O}}{4F} \frac{\varphi p_{vs}(T_{in})}{p_{ca} - \varphi p_{vs}(T_{in})} i \tag{5.16}$$

$$\dot{m}^{Ox}_{H_2O,Out} = \frac{S_{O_2} - \chi_{O_2,in}}{\chi_{O_2,in}} \frac{M_{H_2O}}{4F} \frac{p_{vs}(T_{op})}{p_{out} - p_{vs}(T_{op})} i \tag{5.17}$$

As written above, the proposed model obtains the S_{O_2} and $\dot{m}_{H_2O,Inject}$ values demanded by the fuel cell to sustain its operating condition by solving Eq.(5.12)(5.13). The hydrogen output depends on the S_{H_2} set, while the outlet gas flow rate is calculated in Eq.(5.18).

$$\dot{m}_{OxOut} = \dot{m}_{OxIn} - \frac{i}{4F} M_{O_2} \tag{5.18}$$

Dry air considered components are N_2, O_2, Ar and CO_2. The thermal powers in Eq.(5.13) are obtained from the product of the flow rate by the standard enthalpy of the species.

The main auxiliary system powered by the PEMFC itself is the system that compresses the oxidizer to operating pressure. The power absorbed by the compressor, P_{com}, for each powered cell is estimated from Eq.(5.19).

$$P_{com} = \frac{1}{\eta_c \eta_m} \dot{m}_{OxIn} c_p T \left[\left(\frac{p_{ca}}{p_{amb}} \right)^{\frac{\gamma_a - 1}{\gamma_a}} - 1 \right] \tag{5.19}$$

Where p_{amb} is the upstream pressure, c_p and γ_a are respectively the oxidizer specific heat and specific heat ratio. η_c is the air compressor efficiency, derived from [119], and η_m is the compressor motor efficiency. Fig. 5.8 shows the η_c and η_m values varying the oxidizer flow rate from zero to the maximum deliverable flow rate. The other auxil-
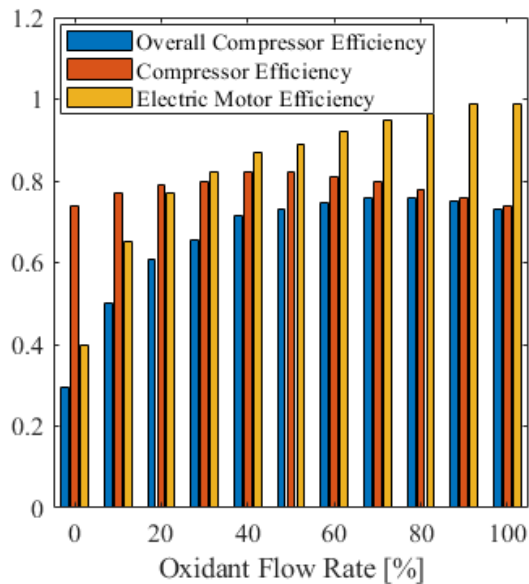
Figure 5.8: Compressor and electric motor efficiency varying the oxidant flow rate.

iary losses, P_{aux}, are estimated as a percentage of the single-cell gross electrical power produced, P_{cel}, taking into account the fuel cell DC-DC converter efficiency reported in Tab.5.2 extracted from [14].

Table 5.2: PEM fuel cell DC-DC converter efficiency as function of gross power delivered.

Power [$\%_{P_{rated}}$]	Converter Efficiency [%]
10	91.9
20	94.8
30	96.1
40	96.3
50	96.3
60	96.5
70	96.1
80	96.1
90	95.8
100	95.4

The stack model presented requires as input the number of cells in series for the single stack, n_{cel}, and the number of stacks, n_{stack}, connected to the DC bus. In the proposed results, each stack is directly connected to the grid, but using the n_{cel} parameter it is possible to simulate the series connection of several stacks.

The gross power demanded to the PEMFC system, P_{gross}, is calculated from Eq.(5.20), where $P_{mission}$ is the power required by the shipboard, therefore the net power extracted

from the plant.

$$P_{gross} = P_{mission} + (P_{com} + P_{aux})n_{stack}n_{cel} \tag{5.20}$$

In addition, the cell power demand, $P_{d,cel}$, is obtained by Eq.(5.21).

$$P_{d,cel} = \frac{P_{gross}}{n_{stack}n_{cel}} \tag{5.21}$$

Finally, the overall system efficiency, η_{FC}, is calculated by Eq.(5.22), considering the system net power $P_{mission}$ and the hydrogen lower heating value (LHV), having gaseous products as exhaust.

$$\eta_{FC} = \frac{P_{mission}}{\dot{m}_{H_2,In}\text{LHV}_{H_2}} \tag{5.22}$$

The thermal management system is characterized by the supplied excess oxidizer S_{O_2} and the mass of injected water $\dot{Q}_{H_2O,Inject}$, parameters calculated as function of the cell operating current. Thus, using equation 23, the efficiency of the proposed solution, η_{cool}, over the life cycle of the PEMFC is evaluated.

$$\eta_{cool} = \frac{\Delta\dot{Q}_{Ox} + \Delta\dot{Q}_{H_2O}}{\dot{Q}_{H_2,In} - P_{cel}} \tag{5.23}$$

Where $\Delta\dot{Q}_{Ox}$ e $\Delta\dot{Q}_{H_2O}$ are the difference between the thermal power of the oxidizer and the water at the inlet and the outlet of the cell, which represent the heat removed from the system. The difference between the hydrogen heating power, $\dot{Q}_{H_2,In}$, and the cell electric power output, P_{cel}, is the heat to dissipate.

5.1.4   Model Calibration and Validation

The PEMFC selected to power the case study ferry is the FCvelocity™-HD6 manufactured by Ballard. The maximum power of each stack is $150kW$, while the main operating parameters are shown in Tab.5.3. Ballard is a leading company in power systems for maritime and heavy-duty applications, and a pioneer in fuel cell systems for vessels.

In order to prove the validity of the PEMFC power unit model the test proposed by [75] was replicated. Tab.5.3 shows the values for α, j_0, j_L and R_i obtained after the calibration made on the experimental data, related to the polarization curve and power output, reported in [75]. The stack dynamic time constant τ_{FC} was obtained, from the analysis of the available experimental data, as corresponding to the time interval when the system reaches 63% of the imposed power step during the test.

Fig. 5.9 presents the result of the model calibration on fuel cell experimental data relative to its characteristic performance. The test covered the whole operating range of the PEMFC up to 300 A, which is the limit value for the working current (I_{Lim}).

Table 5.3: PEMFC Ballard FCvelocity™ HD6 operating parameters from technical literature and customizing variables results for calibration on experimental dataset.

OPERATING PARAMETERS		
Cell active surface – A	500	cm^2
Number of cells – n_{cel}	762	
Operating temperature – T_{op}	330	K
Oxidizer	Dry Air	
Anode supply pressure – p_{an}	2.24	bar
Cathode supply pressure – p_{cat}	2.06	bar
Stack max current – I_{Lim}	300	A
Voltage operating range	465 – 730	V
CUSTOMIZING VARIABLES		
Transfer coefficient – α	0.515	
Exchange current density – j_0	1.9E-7	A/cm^2
Limit current density – j_L	0.8	A/cm^2
Average internal resistance – R_i	0.15	Ωcm^2
Stack dynamic time constant – τ_{FC}	0.9475	s
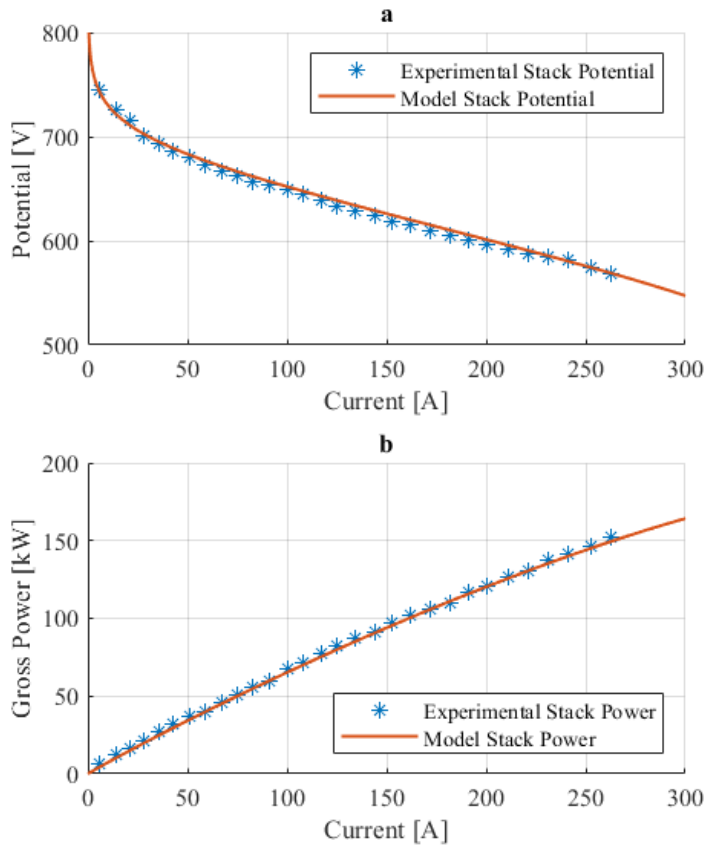
Figure 5.9: Comparison between Ballard FCvelocity™ HD6 experimental data and calibrated proposed model. Figure **a** – Polarization curve, figure **b** – Power output.
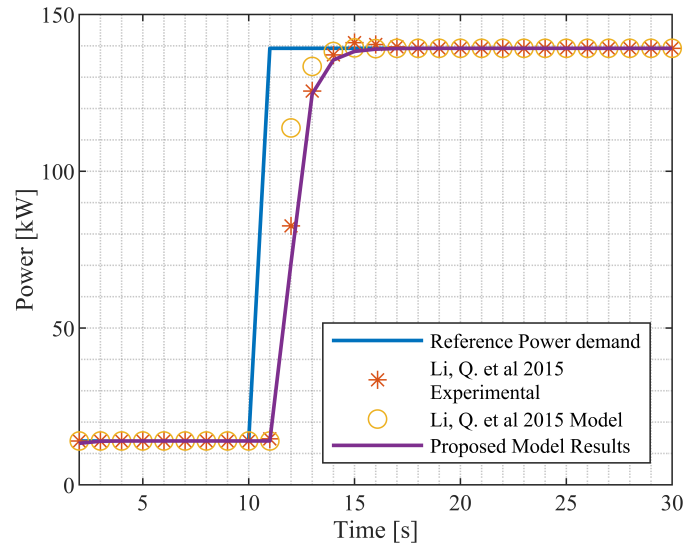
Figure 5.10: Comparison, in terms of power, between experimental and simulations validation test results, conducted by Li Q. et al. 2015 [75], and proposed model.

After calibrating the model, the validation test was performed. Therefore, the performance of the fuel cell in the transient between a power output of $14kW$ and roughly $140kW$ was simulated, setting the computing time step to one second as in the cited work.

Fig. 5.10 illustrate the comparison between the results proposed by Li Q. et al. [75] and the presented model in terms of power output. In detail, the figure shows the dynamic step of the reference power, the experimental and simulation results presented by [75] and the behaviour of the proposed model.

Fig. 5.11 depicts the results of the validation test in terms of stack current and voltage. The proposed model follows the trend shown by the simulations and experiments carried out in [75], demonstrating the validity and reliability, varying the customizing variables, of the developed model.

5.2 The Energy Storage Model

Batteries play a crucial role in hybrid ship powertrains. They are used for energy storage and provide power to the propelling system. The use of lithium-ion batteries is common in these powertrains, as they are the primary battery technology for electric and hybrid vehicles. The batteries need to be kept within a specific temperature range of 15-35 °C to ensure optimal performance and safety. To maintain this temperature range, a controller is used to cool or heat the batteries as needed. The implementation of Li-ion batteries in ship power systems has shown potential for reducing CO_2 emissions. Different types of Li-ion batteries, such as lithium titanate and lithium iron phosphate, have been evaluated, with the latter demonstrating better performance. Overall, batteries are an
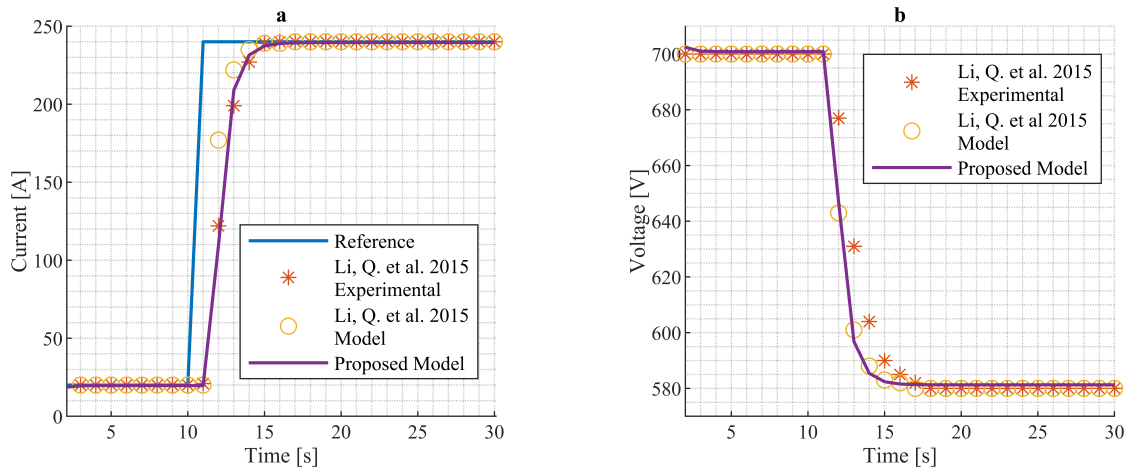
Figure 5.11: Comparison, figure (a) in terms of current & figure, (b) in terms of voltage, between experimental and simulations validation test results, conducted by Li Q. et al. 2015, and proposed model.

essential component in hybrid ship powertrains, providing efficient and environmentally friendly energy storage and propulsion capabilities.

The trend of battery voltage as function of SOC represents the efficiency curve characteristic. Fig. 5.12 reporst the results obtained by Kang J. et al. in 2012 in [120] in terms of prediction of battery voltage during charging and discharging operation, for different current rates.
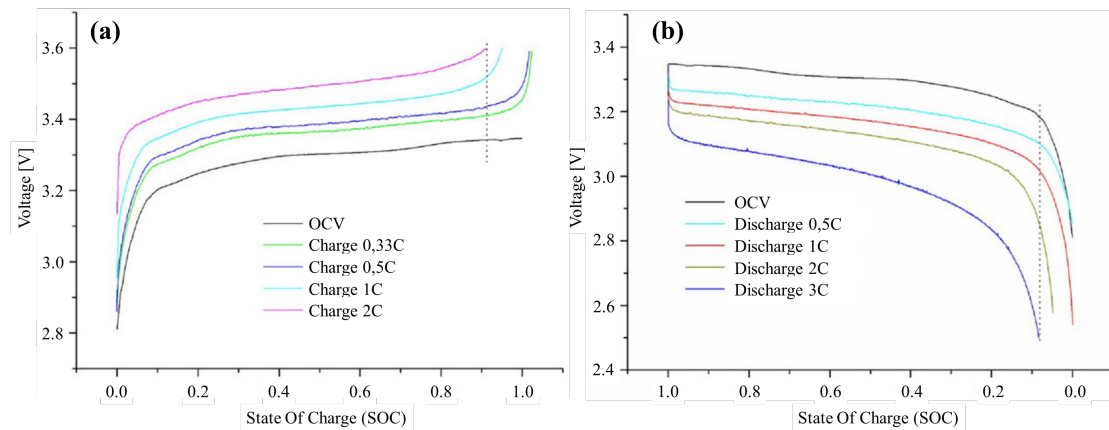
Figure 5.12: (a) The voltages (per cell) varied with SOC under different charge current rates; (b) the voltages (per cell) varied with SOC under different discharge current rates. Presented in [120].

The SOC of the battery represents the Coulombic capacity (Ah) of the storage. Eq.(5.24) to express the change of SOC in a time interval dt, where $Q(i)$ is the ampere-hour capacity of the battery at current rate i.

$$SOC = SOC_0 - \int \frac{i\ dt}{Q(i)} \tag{5.24}$$

For energy system applications the energy capacity (kWh) is more useful than the coulombic capacity (Ah), because is directly associated with operations. Eq.(5.25) defines the energy delivered from the battery, where $V(i, SOC)$ is the actual battery voltage at the defined current rate and SOC.

$$B_c = \int_0^t V(i, SOC)\ i(t)\ dt \tag{5.25}$$

To complete the power generation system model, an energy storage system was integrated. In the model, the battery is considered as an energy storage tank characterized by a capacity, B_c, and a limited charge/discharge rate, C_{rate}. Hence, the battery power output, P_b^{max} is obtained by Eq.(5.26).

$$P_b^{max} = B_c\ C_{rate}^{max} \tag{5.26}$$

In this work, the Corvus Orca Energy is taken as default battery. The capacity of a single battery pack is 124 kWh and the C_{rate} is up to 3 (C_{rate}^{max}). The numerical model takes into account the efficiency of the storage related to the actual State of Charge (SOC), η_b, for a Li-ion battery [121] and the efficiency of the bi-directional DC/DC converter as function of the battery power output (charging/discharging), η_{bc}, taken from [14]. The battery gross power output as function of the net power delivered and remaining capacity is express in Eq.(5.27).

$$P_{b,Gross} = \frac{P_{b,Net}}{\eta_b\ \eta_{bc}} \tag{5.27}$$

The Tab.5.4 reports the values of the efficiency of the battery storage cell DC-DC converter for different battery power levels during charging or discharging operations.

5.3 The Variable Speed Diesel Engine Generator

The Variable Speed Diesel Engine Generator (VSDEG) was mentioned in chapter 2 as one of the main benefits to exploit a DC grid in the shipboard. This section describes the model of diesel engine useful for studying new hybrid solutions for power generation. Although VSDEG is not present in the powertrain configuration case study, this model allows the integration of the generator as an addition or replacement for the battery.

This model was developed using experimental results of bench tests conducted on the VL1716C2-MLL engine by Isotta Fraschini Motori (IFM) SpA, illustrated in Fig. 5.13. Diesel engine dynamics is based on the formulation found in the technical literature on mean value models and then adjusted through experimental data.

Table 5.4: Battery storage cell DC-DC converter efficiency as function of gross power delivered.

Power [$\%_{P_{rated}}$]	Converter charging efficiency [%]	Converter discharging efficiency [%]
8.1	88.2	86.3
17.5	92.5	91.4
27.4	94.4	93.8
37.0	95.5	95.0
47.1	96.2	95.7
57.2	96.5	95.9
67.8	96.6	96.2
78.1	96.7	96.2
89.2	97.1	96.3
100	97.0	96.3
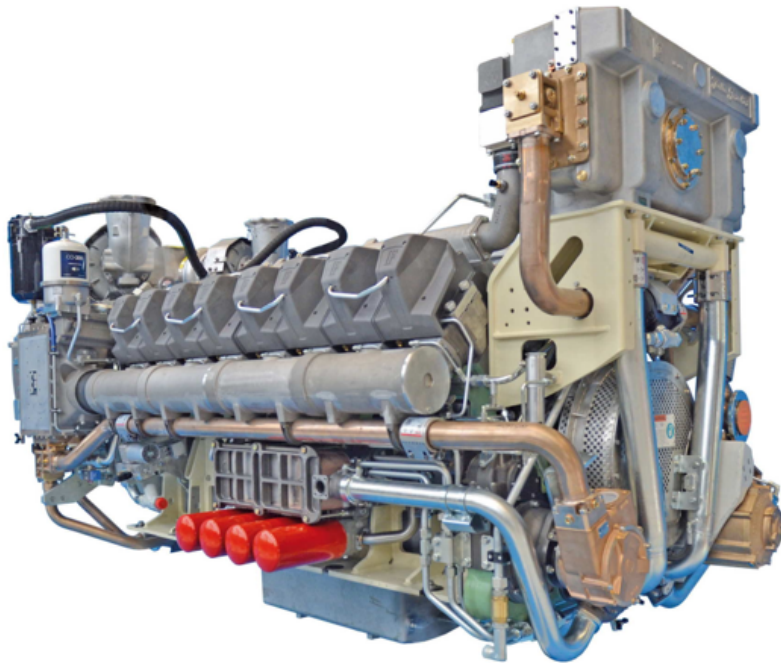
Figure 5.13: Picture of VL1716C2-MLL engine by Isotta Fraschini Motori SpA.

Herein is proposed a VSDEG mean value model with a simple governor strategy to provide the best specific fuel consumption for each applied load. The engine is characterized by a maximum power output of $2MW$ and reaches $1890rpm$ maximum speed. The experimental test results on this engine were made available by the company. The general engine specifications are reported in Tab.5.5. Modeling of the engine dynamic behaviour was based on the transfer functions, available in the technical literature, that

correctly describe the response of an engine to variations in power demand [122] [123].

Table 5.5: VL1716C2-MLL engine technical end performance specification.

DESIGNER & MANUFACTURER	Isotta Fraschini Motori SpA	
TECHNICAL DATA	Value	Unit
No. cylinder & arrangement	16V - 90°	
Bore	170	mm
Stroke	185	mm
Total displacement	67.2	$liters$
Compression ratio	13.2	
Valves per cylinder	4	
PERFORMANCE		
Max speed	1890	rpm
B.M.E.P.	18.9	bar
Emission compliance	IMO MARPOL Tier II	
Mean piston speed	11.65	m/s
Idle speed	700	rpm

The novel contribution of this model is the different interpretation of the control action compared to what can be found in the literature [124] [125] [126]. This variation allowed us to consider the influence of maximum torque that can be delivered by the engine at the current speed, on the control parameters. In addition, the implementation in the model of the esteem of fuel consumption at different load conditions is an original contribution. In the end of the section, a comparison of performance between fixed and variable-speed diesel generator model is presented; this was carried out by simulating a benchmark duty cycle.

5.3.1   The VSDEG Mean Value Model

In the first part of this section, the modeling of the engine and control loop is presented. Then, the proposed fuel consumption calculation method and the engine torque output map obtained through it are reported. A general scheme of the variable speed diesel generation unit equipped with the electric generator and power electronics converter is shown in Fig. 5.14. This paper focuses on the modeling and control of the engine, identified in the red rectangle in the overall schematic.

The engine speed is controlled by an electronic actuator responsible for fuel injection, and its control signal, which is responsible for fuel mass injected per cycle m_f, influences the driving torque T_d. Fuel consumption is obtained from the electronic governor system, and the actual engine speed, ω_{act}, is typically measured by a tooth wheel sensor. In order to characterize the engine, within the model, the performance limit curve and the corresponding fuel consumption have been taken into account. These were obtained by fitting the available experimental data.
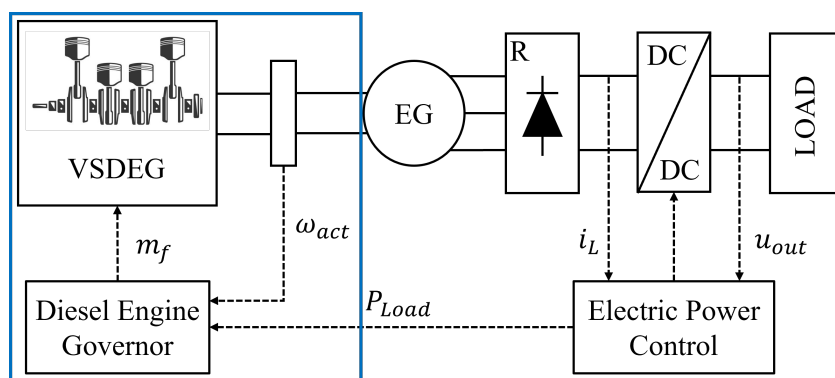
Figure 5.14: General scheme of VSDEG-based power generation unit with the electric generator and power electronics converter. The engine and its governor are in the red rectangle.

The speed controller of a diesel engine is similar for fixed speed and variable speed operation, and the controller parameters depend on the maximum torque, moment of inertia J and engine delays τ_c and τ, defined in Eq.(5.29) and Eq.(5.30). A model of speed control loop for a VSDEG is shown in Fig5.15.
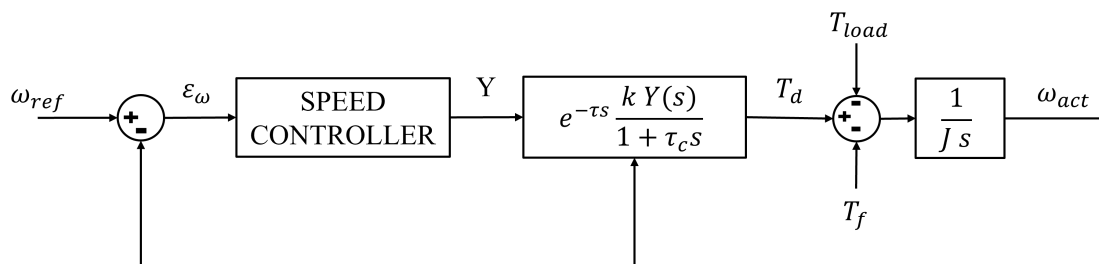
Figure 5.15: Model of the classic speed control loop of a variable speed diesel generator engine.

The governor commands the fuel injection through the control action, Y, called fuel index, that in the Eq.(5.28) represents the fraction of the maximum engine torque then delivered. The relationship between the fuel index and output torque of the engine, T_d, in the Laplace domain is described by Eq.(5.28).

$$T_d(s) = e^{-\tau\ s}\frac{k\ Y(s)}{1 + \tau_c\ s} \tag{5.28}$$

In Eq.(5.28), k is the gain that corresponds to the maximum torque that can be delivered by the engine, τ_c is the time constant corresponding to torque build-up from cylinder firings. While, the time constant τ represents a time delay half the period between consecutive cylinder firings.

The τ_c and τ can be calculated from Eq.(5.29) and Eq.(5.30) [126], where N is the number of cylinders of the engine.
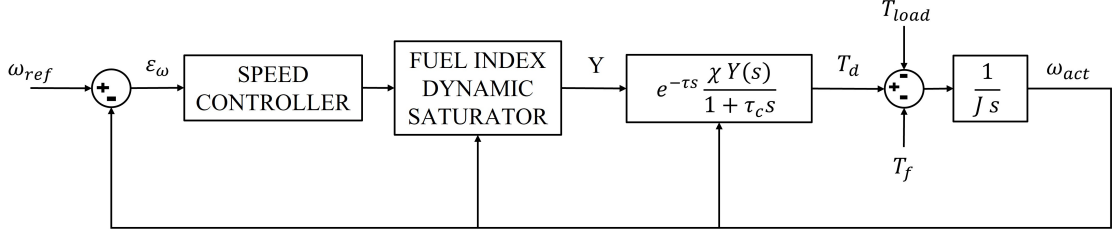
Figure 5.16: Speed control loop model for a variable speed diesel generator with dynamic control action saturator and $\chi(\omega_{act})$ as gain for the fuel index, instead of k.

$$\tau_c \approx \frac{0.9\ [rad]}{\omega_{act}\ [rad/s]} \tag{5.29}$$

$$\tau \approx \frac{\pi\ [rad]}{N\ \omega_{act}\ [rad/s]} \tag{5.30}$$

It should be noted that the behavior of the diesel engine will vary depending on the shaft speed. From Eq.(5.31), proposed in [126], it is shown the maximum value of the fuel index Y_{max} depends on the normalized shaft speed, $\omega_{act}/\omega_{max}$.

$$Y_{max} = \begin{cases} 0.4, & \text{if } \omega_{act}/\omega_{max} \leq 0.4 \\\\ 1, & \text{if } \omega_{act}/\omega_{max} \geq 0.8 \\\\ 1.5\ \omega_{act}/\omega_{max}, & \text{otherwise} \end{cases} \tag{5.31}$$

Once the delivered torque is calculated, the shaft speed ω_{act} is evaluated through the second-order dynamics described by Eq.(5.32), where J is the equivalent moment of inertia, T_d is the delivered torque from the engine, T_{Load} represents the loads connected and T_f is the friction torque.

$$J\ \frac{d\omega_{act}}{dt} = T_d - T_{Load} - T_f \tag{5.32}$$

Instead, Fig. 5.16 shows the schematic of the engine dynamics model here proposed. The model just described and the one proposed have two main differences. The fuel index Y is limited from 0 to $(1 + \Delta)$, where Δ depends on the engine speed and represents the additional power over the engine limit curve, which is needed for acceleration. Moreover, the gain k is replaced by χ in the transfer function. The parameter $\chi(\omega_{act})$ represents the available torque on the engine limit curve, as a function of speed ω_{act}. In this way, the control action will affect the maximum torque available for a given engine speed.

The most significant difference between the proposed model and the ones available in the literature [122] [125] [126] is the method of estimating fuel consumption. The

flowchart of the proposed algorithm is summarized in Fig. 5.17. First of all, the required input parameters are the fuel index, Y, and the engine speed ω_{act}.
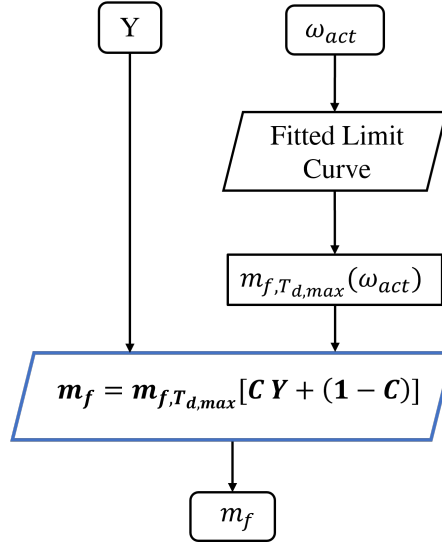
Figure 5.17: Flow-chart for fuel consumption calculation.

Thus, the mass of fuel injected per cycle, m_f, is calculated in Eq.(5.33), where $m_{f,T_{d,max}}$ is the fuel consumption related to the limiting torque for a given speed ω_{act} and C is a constant, which is chosen to minimize the error compared with the experimental data.

$$m_f = m_{f,T_{d,max}} \left[C\, Y + (1 - C) \right] \tag{5.33}$$

The Eq.(5.33) introduces a linear relationship between the fuel index Y and the fraction of fuel injected relative to that injected to yield the limiting torque $(m_f/m_{f,T_{d,max}})$. The engine map shown in Fig. 5.18 was generated using the proposed formulation for calculating fuel consumption. Thanks to this map, it was possible to identify the correct speed in order to minimize the specific fuel consumption (SFOC) for each power required.

The validity of the described method was tested by comparing the amount of fuel injected during the experimental tests with the estimated value predicted by the model. On a validation data-set of sixty-one points, the maximum error was 9.5%, whereas the average error was 1.9%. Only some of the experimental points taken into consideration are shown in Fig. 5.18 for better visualization of the image. For these, the percentage error between the specific fuel consumption related to the experimental tests and that calculated by the model is displayed. As can be seen in Fig. 5.18, the greater prediction error is on the lower load points, whereas the data near the engine limit curve have an error of less than 1%.
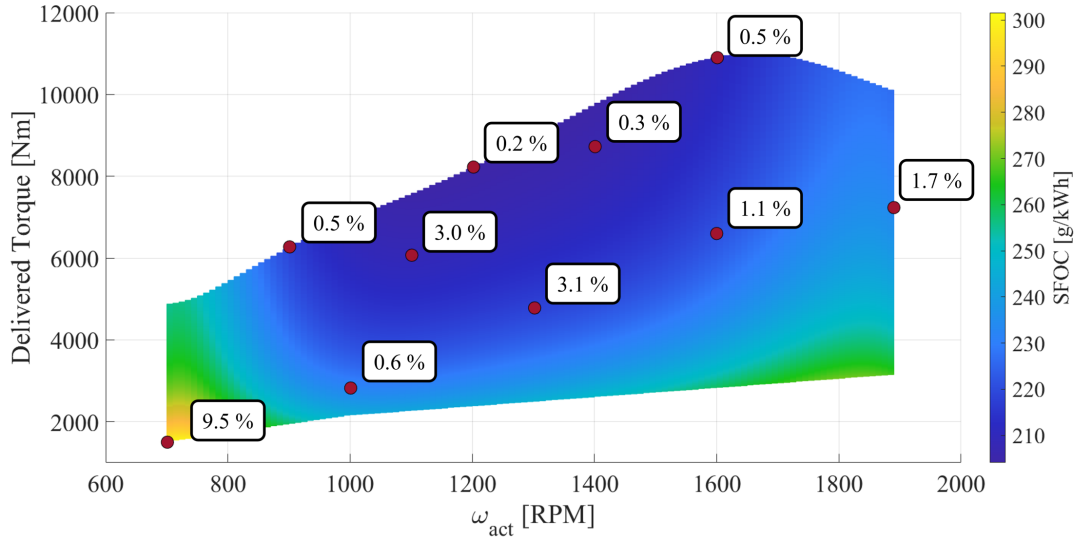
Figure 5.18: Engine delivered torque map with SFOC $[g/kWh]$ by the proposed calculation, showing the relative error in percent for some of the experimental validation data.

5.3.2 The VSDEG Simulations Results

The simulation results were obtained by implementing the optimal speed, ω_{opt}, as reference speed for the model. This optimal speed was calculated in order to optimize the specific fuel consumption for each load connected to the system. Fig. 5.19 illustrates how, during the simulation, the engine speed, ω_{act}, follows the reference speed, ω_{opt}. Nevertheless, many factors, such as fuel quality, temperature, engine installation altitude and others, may cause the selected optimal speed to not perfectly match the load power and the minimum SFOC for a given power demand is not achieved.

The load profile required for the generator and the power delivered are shown in Fig. 5.20. In the first part, every five seconds the required power increases by 10% up to 90%, of the maximum deliverable power. After that, once the engine is brought to deliver the minimum power, it is required to take two more steps, one up to 20% and then up to 90% of the maximum power, respectively. Then the required power will be gradually reduced to 30%. This kind of load profile is widely used in the literature [127] because it allows the correct behavior of the model to be verified for different operating conditions, including the sudden demand for a very high load.

Results regarding the specific fuel consumption, estimated for the described duty cycle, were compared in both the variable and fixed speed modes. Working at variable speed, the engine follows the optimal speed reference ω_{opt}. Whereas, the chosen fixed speed was at 1800 rpm to match the operating speed of a 4-poles electric machine working at $60Hz$.

As can be seen from Fig. 5.21, the variable speed operation reduces the fuel consumption with respect to the fixed speed operation. As can be noticed in the area marked in
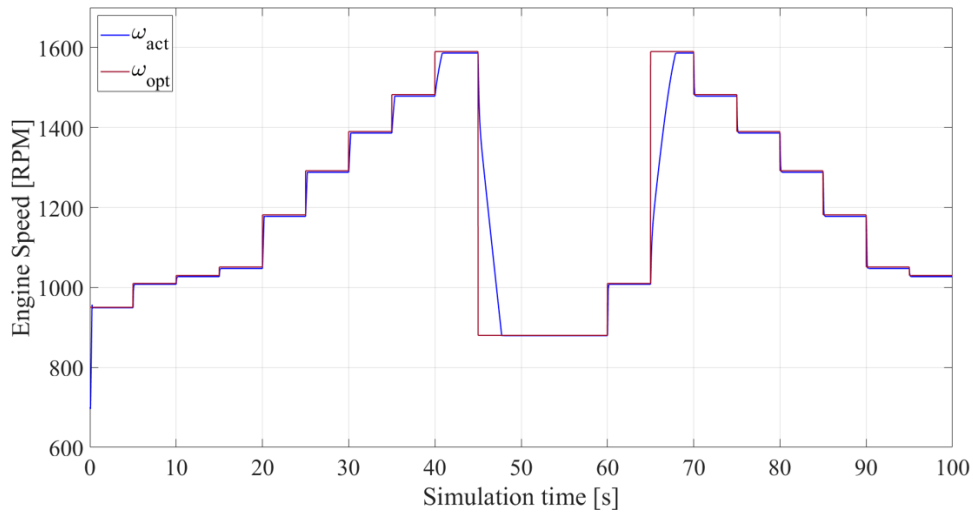
Figure 5.19: Resulting speed response of the engine, in blue, following the optimal speed reference, in red, to reach the applied load.

Fig. 5.21, at the time when the engine has to decelerate, hence does not have to deliver torque, the fuel consumption is cut off.

Tab.5.6 shows the SFOC values at different loads for both VSDEG and FSDEG modes with the relative improvement in percentage. The results are in accordance with those found in the literature [128]. The considerable fuel savings at partial loads is a significant result since, for several naval applications, most of the operating time the power demand is less than 40% of the power installed.

Table 5.6: SFOC improvement according to the applied load for both variable and fixed speed modes.

Power Load [%]	g/kWh for VSDEG (ω_{opt})	g/kWh for FSDEG ($1800rpm$)	SFOC improvement [%]
10	249	366	32
20	221	292	24
30	211	265	20
40	206	251	18
50	204	243	16
60	204	237	14
70	204	233	12
80	206	230	10
90	210	227	8

The results obtained by optimizing the specific fuel consumption at different loads required were compared with those obtained for fixed speed operation, achieving fuel savings of up to 32%.
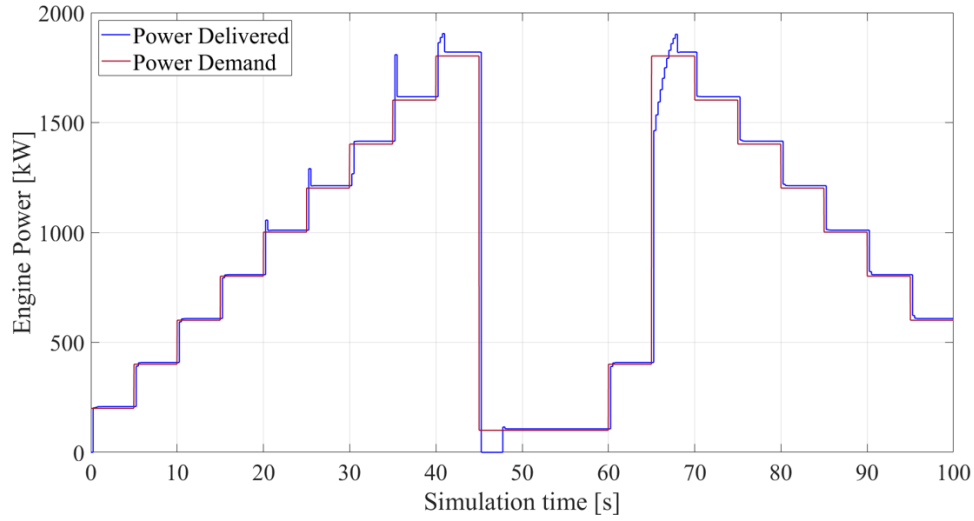
Figure 5.20: Power demanded at the generator, in red, and the engine response, in blue.
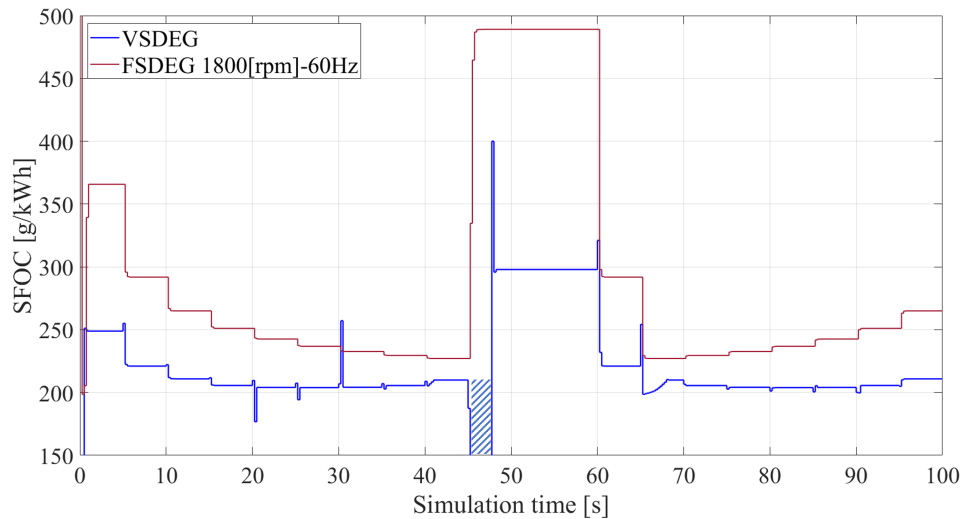
Figure 5.21: Simulation results in term of SFOC $[g/kWh]$ for variable and fixed speed modes.

This work lays the foundation for the future application of more complex generator governance strategies to optimise its operation within model of grid-connected hybrid systems.

5.4   The Energy Management Strategy

Integrating the Energy Management System (EMS) is crucial when determining the size of different components. The EMS facilitates the combination of various renewable energy sources and backup systems, addressing the challenges of inconsistent energy supply

and guaranteeing uninterrupted power. By optimizing component sizes and implementing an effective energy strategy, the EMS reduces the system total cost and limits adverse impacts.

The battery energy storage helps to balance out the peak power needs of the Fuel Cell (FC) and provides consistent electrical supply to the ship's grid, ensuring the PEMFC stacks function efficiently. The real-time Energy Management Systems (EMS) determines the operating mode based on the ship's power needs and the battery's state of charge. It also decides when and how to utilize power from the shore during cold-ironing mode.

P_d^{filter} is the total power demand, limited to the maximum PEMFC net power $P_{FC,Net}^{max}$, passed through a low pass filter. The latter is characterized by a customizable time constant τ_{FC} greater than or equal to the stack dynamic time constant. Higher τ_{FC} means lower cut-off frequency which makes the demand power signal smoother. Hence, the P_d^{filter} can be obtained by Eq.(5.34).

$$P_d^{filter}(s) = \begin{cases} \dfrac{P_d}{1 + \tau_{FC}s}, & \text{if } 0 \leq P_d \leq P_{FC,Net}^{max} \\[4mm] \dfrac{P_{FC,Net}^{max}}{1 + \tau_{FC}s}, & \text{if } P_d > P_{FC,Net}^{max} \end{cases} \tag{5.34}$$

The actual battery state of charge, SOC_{act}, and P_d^{filter} are calculated in the model and used as input for the EMS. Finally, the EMS considers constant values as SOC_M and SOC_m, respectively upper and lower thresholds for the battery capacity, SOC_0, the starting capacity of the storage, and the limit net power output for the PEMFC, $P_{FC,Net}^{max}$, and for the battery, $P_{b,Net}^{max}$. In this work SOC_0 is set to 0.5, SOC_M is 1 and SOC_m is equal to 0.3.

Fig. 5.22 shows the four states, or modes, that represent the governor of the power generation system and the transition constraints based on the parameters just described. The base state is Default Navigation. In this mode, the power P_d^{filter} is requested to the PEMFC system while the exceeding power demand, positive or negative, is given from the energy storage. Therefore, the exceeding power is positive when the fuel cell delivers more than the power adsorbed by the loads and it is used to charge the battery, when negative is drained from the battery.

If, during the mission, the SOC_{act} reaches SOC_M, this condition triggers the Single Direction Batt. state. This basically works as the Default Navigation, but the energy storage can't be charged and is more exploited until the SOC_{act} returns to SOC_0. If the battery capacity goes lower than SOC_m, Low SOC Mode is activated and the fuel cell charges the storage, unless the FC power demand is more than $P_{FC,Net}^{max}$. The last state is the Cold Ironing, that is activated in case of SOC_{act} lower than SOC_M and the shore power P_{Har} is available. In Cold Ironing, the PEMFC only works for the power
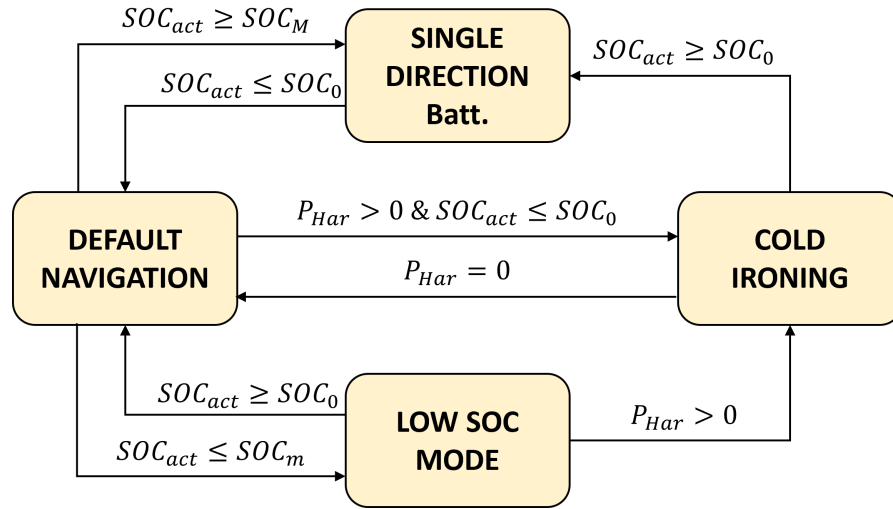
Figure 5.22: Energy management strategy navigation modes and transition constraints.

requirement that the harbour grid cannot meet, meanwhile the storage is charging. This state remains active until shore power is lacking or the battery is full.

The application of online rule-based strategies for fuel cell powertrain management is presented in [129]. The main advantage of online rule-based EMS is that it can be used in real-time, allowing for immediate adjustments based on current operating conditions [130]. This enables better use of engineering resources and improves reliability [131]. Additionally, online EMS can provide warning signals for setting mismatches and contingencies, ensuring the security and stability of the power system [63]. However, online rule-based EMS may not achieve the best behavior compared to optimal-based algorithms. Optimal-based EMS can provide the best performance but requires offline simulations and backward analysis. Rule-based EMS, on the other hand, can be less efficient but can be used online and with forward simulations. Deduction of rule-based EMS from optimal-based analysis can help bridge the gap between the two approaches.

Chapter 6

The Case Study and Results

Norway stands out as one of the leading European nations that heavily relies on maritime transport, particularly for covering short to medium distances. This reliance is evident in the fact that a significant portion of its extra-urban mobility is facilitated through ferries. Given the country's geographical layout and its extensive coastline, ferries play an indispensable role in connecting various regions. Recognizing the environmental implications of conventional sea transport, there is a strong push, both from the Norwegian government and the broader community, towards the adoption and development of innovative, environmentally-friendly solutions. The emphasis is particularly on zero-emission technologies, which are seen as the future of maritime transport in the region.

The specific case study selected for this research project, as illustrated in Fig. 6.1, pertains to a ferry that sails the pristine waters of Norway. In its current operational setup, this ferry employs a combination of batteries, which serve as its primary source of power, complemented by two diesel generators that act as a backup power source. The onboard electrical infrastructure is based on a direct current (DC) system, and it has been designed to seamlessly integrate with the electrical grid at the port, facilitating easy power exchange.

This particular ferry, with its existing configuration, represents an exemplary subject for this research. The presence of a battery-based power system operating within a DC grid offers a unique opportunity. It allows us to conduct a comprehensive feasibility study on the potential integration of a Proton Exchange Membrane Fuel Cell (PEMFC) system. The reliability of this study is further enhanced by the power demand experimental data. Indeed, the power conversion of the case study ferry is the same as the proposed powertrain configuration. This alignment ensures that our findings and recommendations are grounded in real-world operational dynamics, making them both relevant and actionable.

Figure 6.1: The ferry currently powered by batteries and diesel genset, chosen as a case study.

6.1   The Case Study

Fig. 6.2 reports the experimental data relatives to 8.5 h ferry's mission and the sample time of the data-set was of 6 seconds.
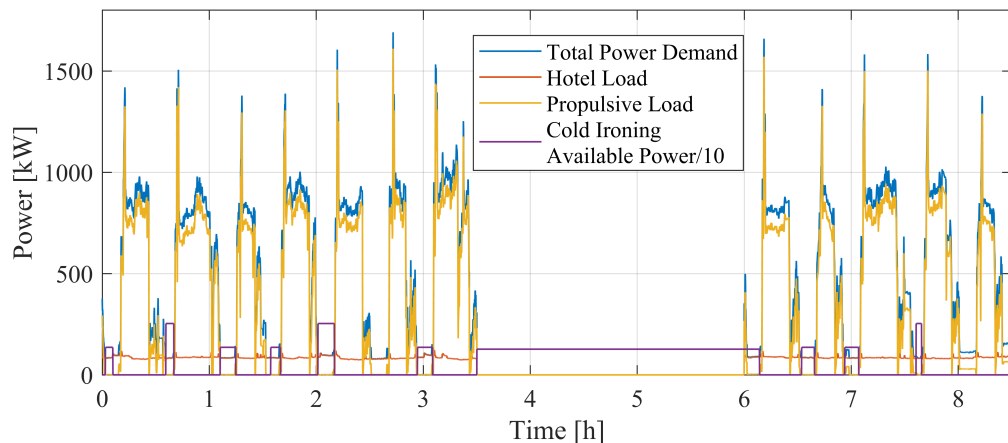
Figure 6.2: Mission hotel/propulsive load profiles and the shore power available.

As discussed in the previous section the case study represents the physical object of the prescriptive digital twin. Thus, all the key data to design and optimize the hybrid PEMFC system are derived from the experimental profiles. The vessel under investigation in this work is a ferry operating in Norway. Currently, the ship has a full-electric propulsion system, whereas two battery packs and two diesel generators, as back-up, are connected to a DC switchboard as energy sources. The case study was characterized starting from the power demand profiles of the two propulsive electric motors and the ferry's hotel load. Moreover, Fig. 6.2 shows both when the shore power is available and the maximum power of the harbour grid. As can be seen in Fig. 6.2, the ferry's mission is interrupted for 2.5h after 3.5h of operation. During the pause, the

fuel cell is switched off and only Cold Ironing mode is allowed.

The presented model performs the simulation with a time step of one second. The detailed sampling rate of experimental data offers the opportunity to investigate the fuel cell system's dynamic performance and to study its coupling capabilities with energy storage such as batteries or supercapacitors. However, the objective of this work is to investigate the feasibility of the PEMFC system to power a long-haul ferry during its entire lifecycle considering the cell degradation rate.

The average target life for a PEM fuel cell system for transports is around 5000 hours, as reported in [132] [133], so the effects of the degradation on the PEMFC system were studied through the model described above, by simulating a cycle of 600 missions, equivalent to 5100 working hours. At the beginning of each mission, the polarization curve was updated to take into account the potential lost during the operations. Also $P_{FC,Net}^{max}$ was updated according to the estimated degradation, in order to improve the robustness of the EMS strategy.

6.2 The Optimization Framework

According to C. Verdouw et al. (2021), [134], the prescriptive digital twin refers to an intelligent digital entity that enhances real-life objects by providing recommendations for corrective and preventive actions. Typically, these recommendations are derived from optimization algorithms. These prescriptive twins utilize the data obtained from monitoring and predictive twins as input to propose appropriate actions, ultimately aiming to achieve favorable outcomes. Decisions on recommended actions are still made by humans, who also trigger remote or on-site execution of interventions.

Fig. 6.3 shows the prescriptive digital twin framework that has been developed. The Physical Object represents the existing ferry, which is characterized by its actual power system and operational mission data, such as performance and efficiency. The Digital Asset simulates a new layout for the ferry's power system using a PEMFC and battery, which must meet the power demands of the Physical Object. The optimization open variables are the number of PEMFC Ballard FCvelocity™ HD6, N_{FC}, the number of Corvus Orca Energy packs, N_b and the low pass filter time constant, τ_{FC}.

The constraints implemented are presented in Eq.(6.1), where $P_{Stack,Net}^{max}$ is the limit net power output of a stack of the Ballard FCvelocity™ HD6 and P_{pack}^{max} is the maximum power of the single Corvus Orca Energy pack.
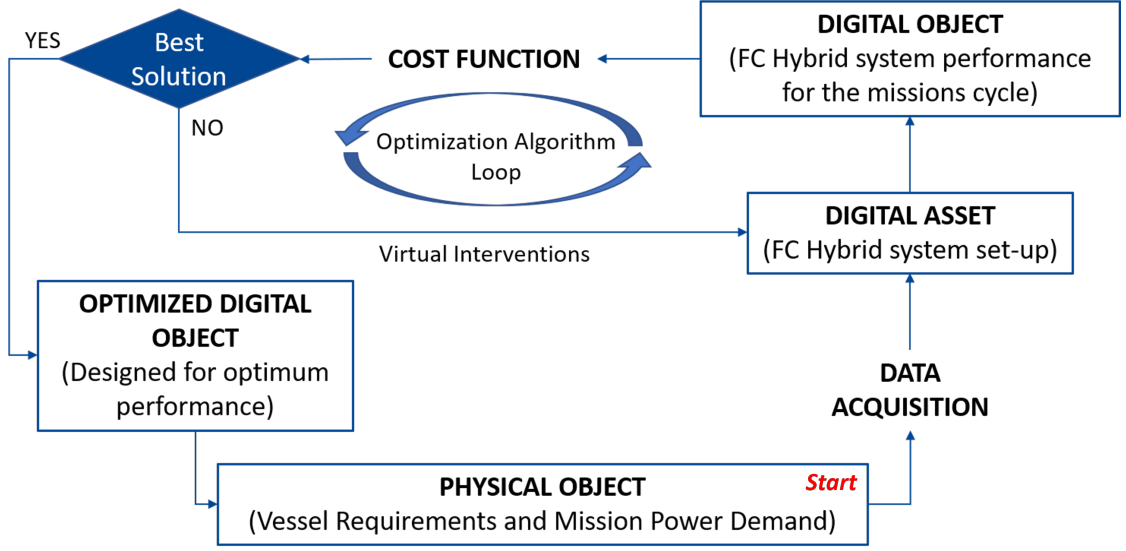
Figure 6.3: Prescriptive digital twin control framework.

$$
\begin{cases}
N_{FC}, N_b \text{ are integer} \\
3 \leq N_{FC} \leq 15 \\
1 \leq N_b \leq 4 \\
0.947 \leq \tau_{FC} \leq 50 \\
N_{FC} \; P^{max}_{Stack,Net} + 0.8 \; N_b \; P^{max}_{pack} > P^{max}_d \\
N_{FC} \; P^{max}_{Stack,Net} - N_b \; P^{max}_{pack} > 0
\end{cases}
\tag{6.1}
$$

The simulation results as power system configuration and performance determine the Digital Object. The Matlab GA optimization algorithm evaluates the best solution, referred to as the Optimized Digital Object. The prescriptive digital twin's output provides recommendations for the sizing and preliminary design of the ferry's hybrid power system. The objective function that aims to reduce this work is the PEM fuel cell stack degradation, which is fundamental for all the design aspects, from sizing to evaluating the operational costs.

Tab.6.1 lists the genetic algorithm options selected for this project.

Table 6.1: Matlab GA selected options

Options	Values
Constraints tolerance	1E-3
Crossover fraction	0.2
Elite count	5
Max generations	300

6.3 Results and Discussion

The optimization algorithm found the best energy source sizing and fuel cell time constant that minimize the stack degradation. The proposed solution consists of 8 PEMFC Ballard FCvelocity™ HD6 ($150kW$), 3 Corvus Orca Energy packs ($124kWh$ per pack) and set the low pass filter time constant τ_{FC} equal to the natural FC system time constant 0.947.

A sensitivity analysis was performed on the effect of τ_{FC} on different feasible plant solutions. For a balanced plant, such as the one obtained from the GA where the battery and fuel cell power ratings are similar, higher values of τ_{FC} are irrelevant or detrimental to stack degradation. Indeed, the PEMFC system had to meet a significantly more stable load than a solution where most of the power is delivered by the fuel cell, and thus higher τ_{FC} values (20-50) can have a positive impact on reducing degradation.

The first proposed results are related to the individual mission carried out over a 8.5 hour period, in order to provide a clear benchmark for assessing the effects of degradation on the system. Fig. 6.4 shows the power output of the hybrid system, where the negative values of battery power corresponds to storage charging. Moreover, the same figure reports that the EMS chooses to not recharge from the shore grid. Indeed, the bottom part of Fig. 6.4 shows the trend of SOC_{act}, which ends the mission by storing energy from the FC excess power output and not from the grid. The same picture shows the efficiency of the PEMFC system, which along the mission profile remains stable between 43.7% and 53.7%.

In Fig. 6.5 part of the first mission is shown in detail, in particular between 2.6-3.5h, to explain the proposed operation. This route, during the first mission, is traveled in "Default Navigation Mode". The power demand and navigation phases are described at the top: navigation, maneuvering, and stop at the port. At the bottom, the trend of consumed hydrogen and battery SOC are depicted. The rapid increase in power demand, going from stop to sailing and during navigation, is met by using both power resources, where the battery serves the "peak-shaving" function. Energy storage during the other phases is minimally exploited allowing the required load to be coupled with the fuel cell dynamics. During the second sailing period, the power demand exceeds the available power of the fuel cell. In this case, the battery provides power for an extended period while the fuel cell operates at the maximum available load.

Fig. 6.6 depicts the effect of the degradation on the battery SOC and the PEMFC efficiency during the 600 missions simulation. The efficiency of the fuel cell system never drops under 38.7%. The energy storage capacity trend describes better how the EMS changes its approach to the mission taking into account the potential lost by the FC.

The energy required by the battery increases with the number of missions completed because it must compensate for the loss of FC performance caused by the degradation of the cell. In Fig. 6.6, it can be seen how depending on the need, the EMS manages
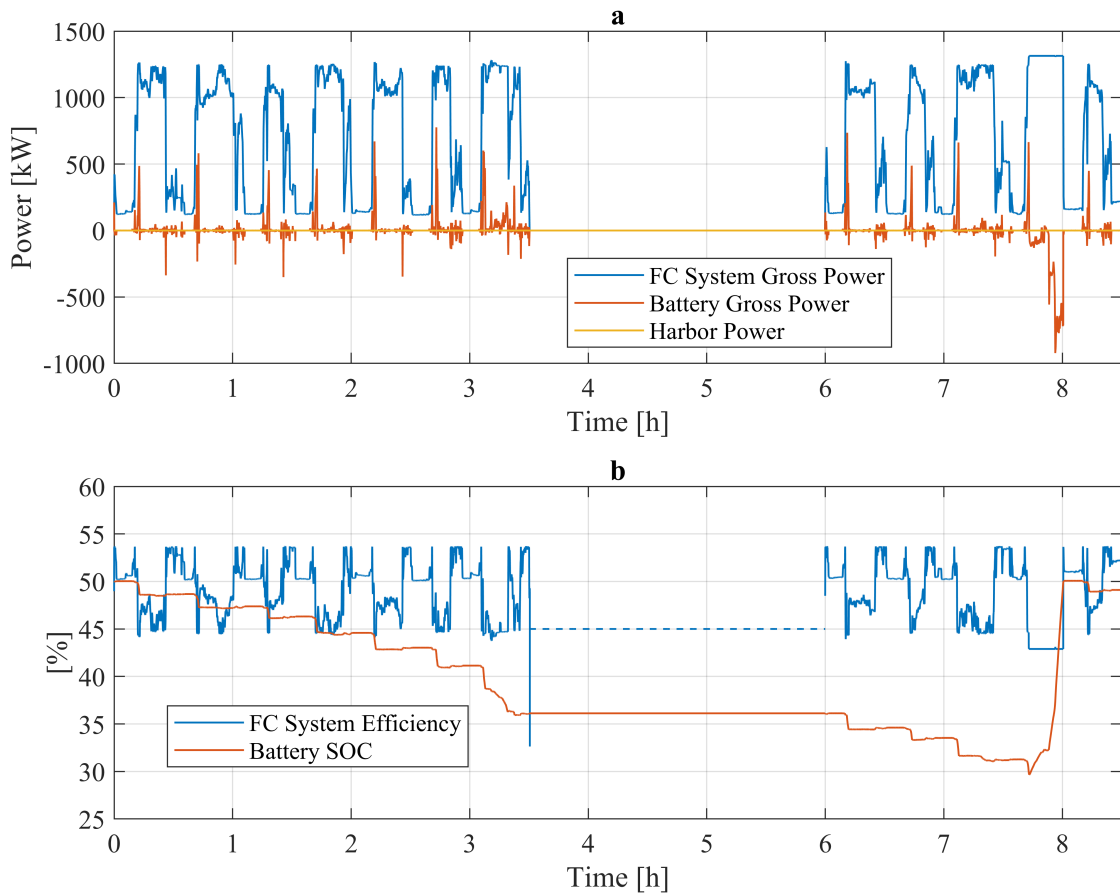
Figure 6.4: a - Mission power profiles of the FC system and battery gross power output and the amount of power taken from the harbour grid; b - Energy storage capacity and FC system efficiency along the first mission.

battery charging during different port stops.

In Fig. 6.7 it is evident how, since the 184th mission, the EMS has been using primary system energy and port energy more frequently to recharge the battery. The EMS from mission #393, and even more so from mission #547, mitigates battery utilization, stressing the fuel cell to recharge it. The next progress of this work intends to implement an optimisation in order to reduce the overall energy and monetary cost of the period under study.

Fig. 6.8 provides significant results on the strategy adopted by the EMS during the test cycle showing the percentage of effective navigation time spent in each EMS state.

The Single Direction Batt. mode was never triggered. Hence in every mission, the battery was able to store the excess power produced by the PEMFC improving its transient performance. Indeed, the Default Navigation mode is active most of the time, running both the energy sources in the desired set-up. The PEMFC degradation increases the energy storage exploitation, the reason why the time spent in Low SOC Mode and Cold Ironing increases after the 300th mission.

Figure 6.5: The power demand and navigation phases, for the mission between 2.6-3.5h, are described at the top. The trend of consumed hydrogen and battery SOC, during "Default Navigation Mode", are depicted at the bottom
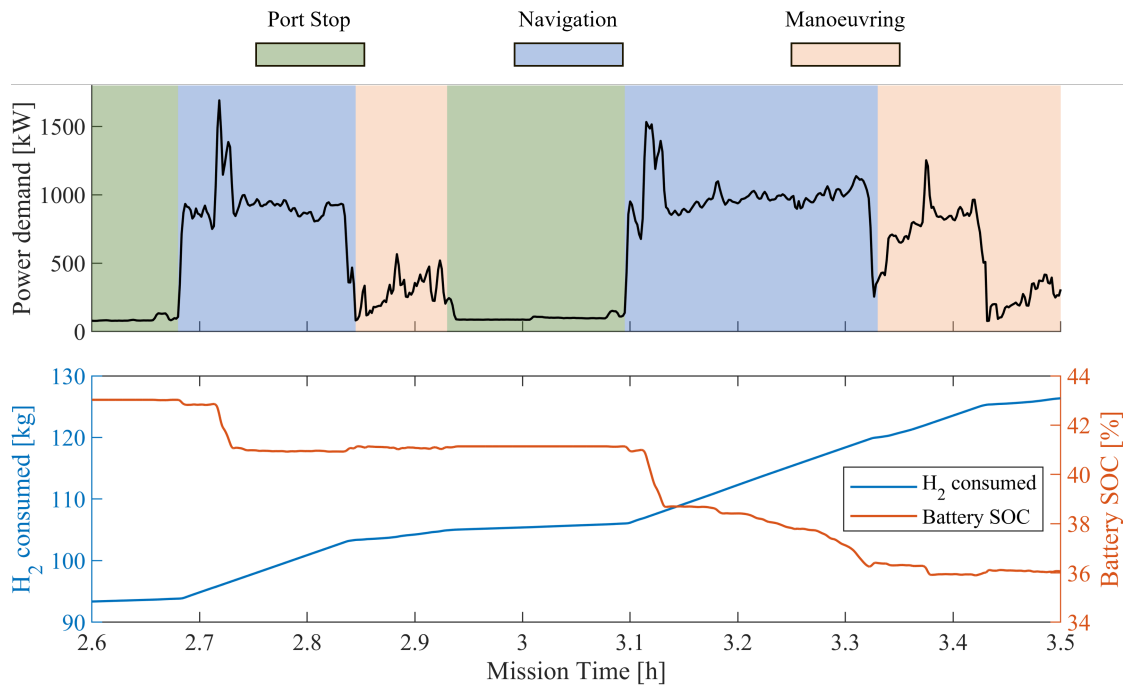
The Fig. 6.9 shows the degradation of the single PEMFC limit potential from the rated value of $730V$ to $679V$. The total H_2 consumption for a single mission increases from $198kg$, for the first mission, to the maximum value of $227kg$, during the 575th mission. Therefore, after 4887.5 operative hours, the fuel consumption increases by 14.65%. Obviously, it will be of future interest to analyze the behavior of EMS between mission 500 and 575, where consumption appears very high compared to the trend. Trend resumed in the last mission, after 5100 hours of navigation, a consumption of $217kg$ of H_2 is recorded, only 9.6% more than the hydrogen consumed during the first mission. The trend of the fuel consumption along the mission cycle gives important insights on the H_2 tank on board, resulting in a more efficient design of the power system and avoiding maintenance costs for the shipowner.

The simulated generation system performed the described mission 600 times in order to evaluate its performance during a total of 5100 operational hours. For each completed mission, we determined the relative degradation and updated the polarization curve for the next mission. As input to the degradation estimation function, the vector of the power produced by the single cell during the concluded mission, as the reference dataset, and the maximum power output of the cell ($215W$) were provided.

Fig. 6.10 shows the polarization curves after several missions conducted, up to #600. The effects of degradation are visible as they reduce the operating voltage of the stack for a given current. Analyzing the polarization curve obtained to perform the 600th
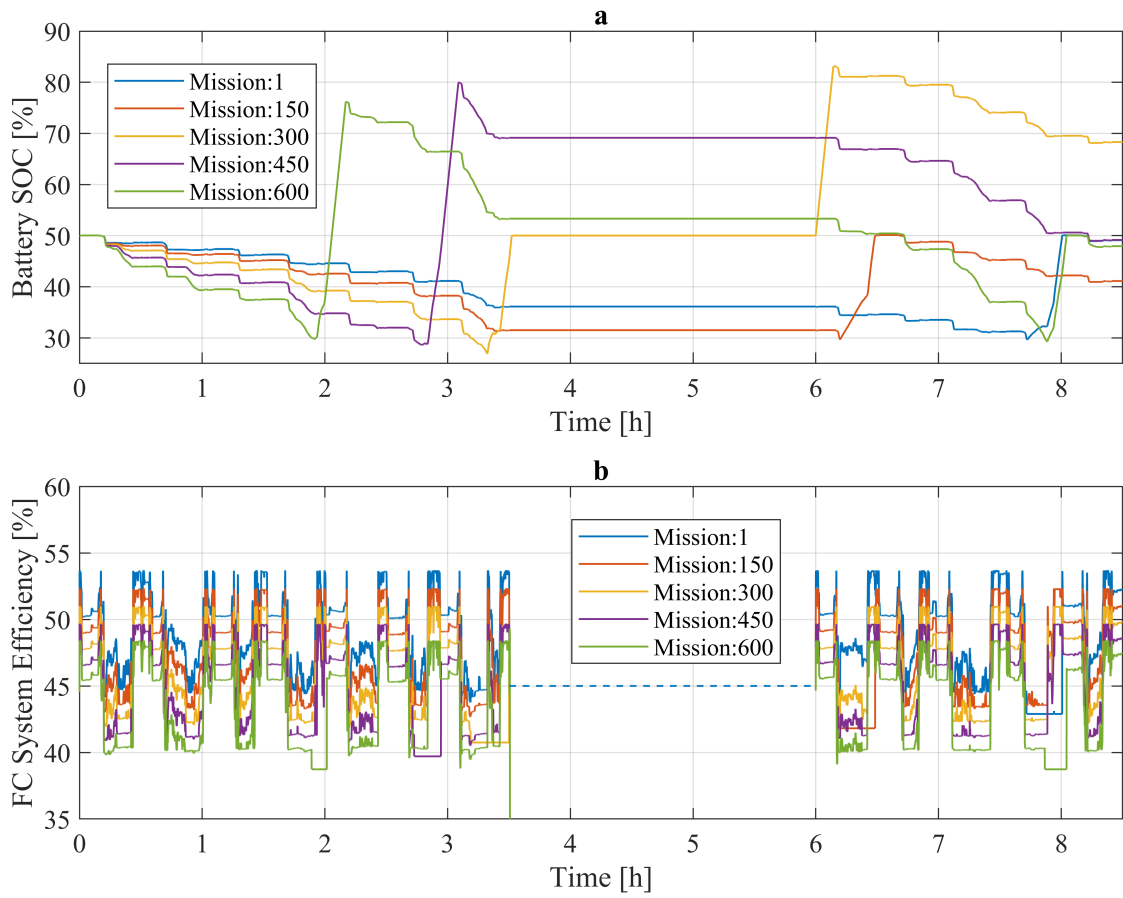
Figure 6.6: a - Effect of degradation on the battery *SOC* along the test simulated; b - Effect of degradation on the PEMFC efficiency along the test simulated.
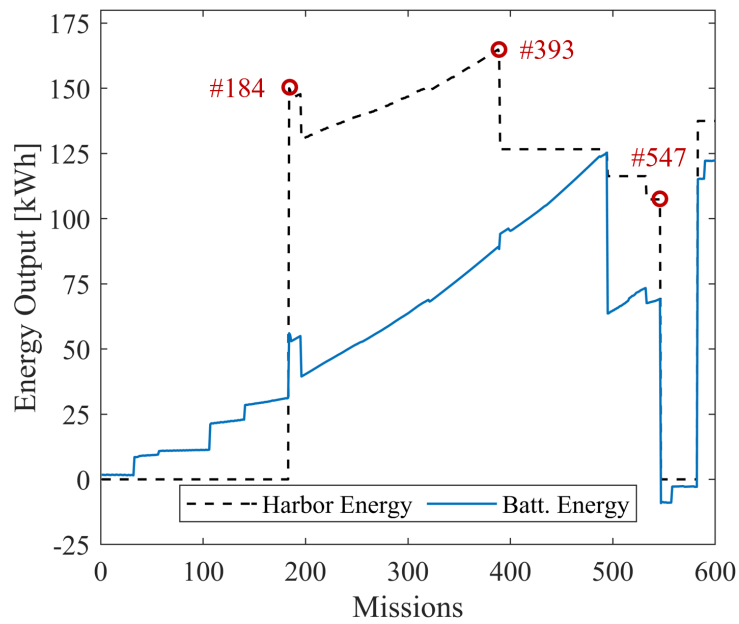
Figure 6.7: Total energy provided by the battery and the harbour for each mission.
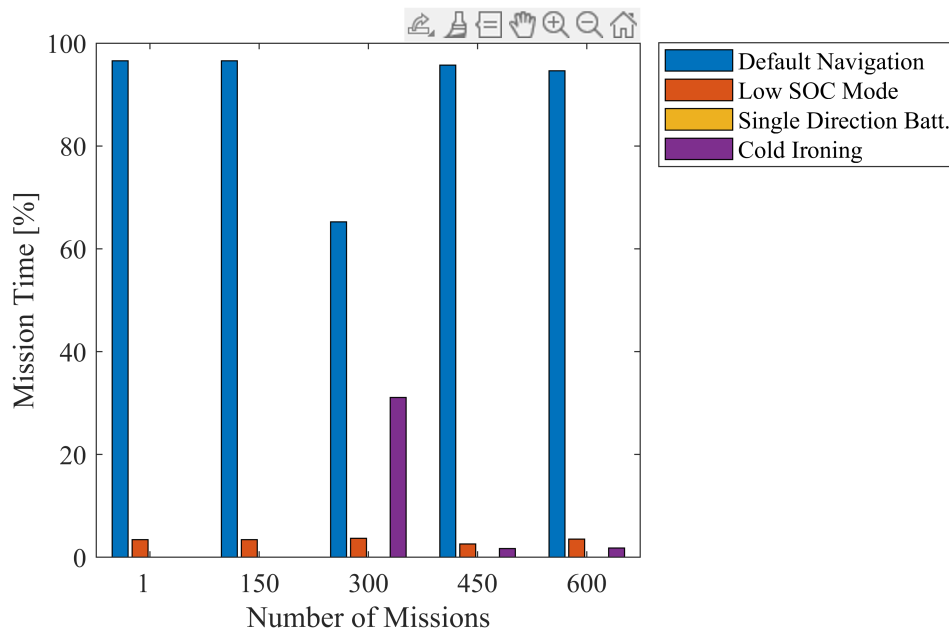
Figure 6.8: Effective navigation time for each of the EMS states.
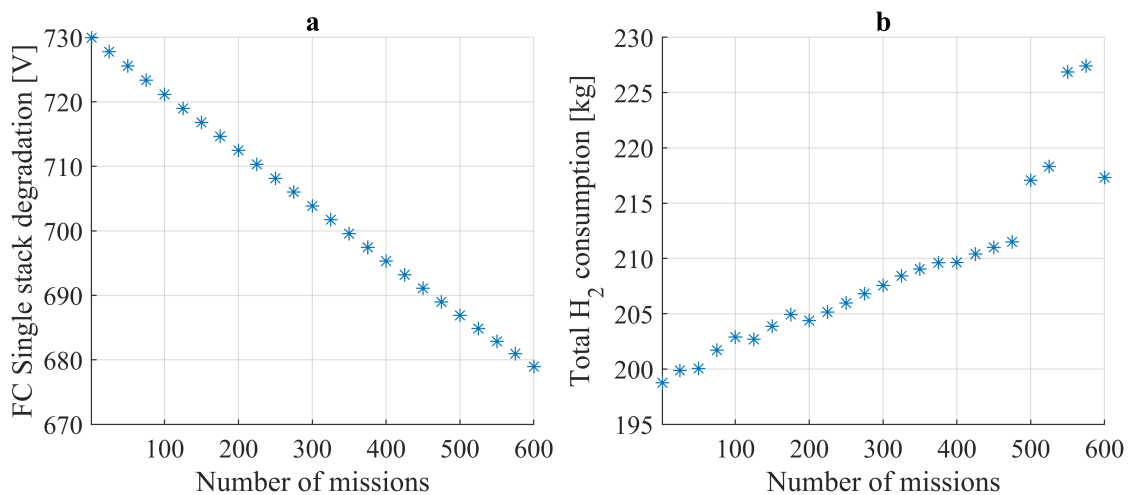
Figure 6.9: a - PEMFC Ballard FCvelocity™ HD6 limit potential degradation along the test cycle; b - Total hydrogen consumed in a single mission along the test cycle.

mission, it appears that over the entire operating current range ($I_{Lim} = 300A$) the voltage remains within the range provided by the manufacturer, not dropping below the lower limit of $465V$. The PEMFC system can work properly but delivers less power for the same operating current, as the voltage is decreased.

Fig. 6.11 describes the trend of the oxidant excess ratio (S_{O_2})) and the amount of water injected in the oxidant gas along the first mission and for all the operative cycles. I risultati mostrati sono fondamentali per comprendere come sta funzionando il sistema di thermal management della fuel cell. The excess oxidant never exceeds the value of 4.7, remaining in the range described in the literature [102]. Thus, the proposed strategy,
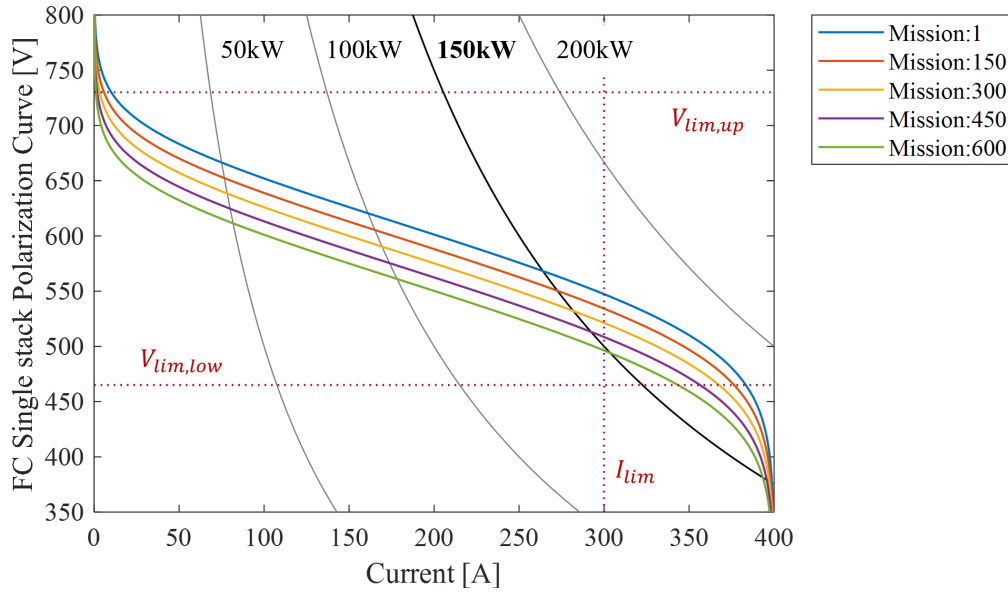
Figure 6.10: Single stack polarization curves after the degradation estimated through the proposed linear model.

although simple, turns out to be very effective and easily handled even considering the degradation of FC. The amount of water injected at the oxidant inlet helps to dispose of excess heat and allows the MEA to remain moist.

In conclusion, the results presented show that the designed PEMFC system succeeds in performing the 5100h of operation before cell degradation making the generation plant unable to supply the required power during the mission.

The last proposed result concerns the average efficiency of the plant thermal management system, illustrated in Fig. 6.12 as function of the number of missions completed. The cooling system is designed to dissipate more than 98% of the heat produced during the first mission, but this value drops to about 90% for the last mission. This result confirms the feasibility of the presented PEMFC thermal management strategy, working correctly up to the 600th mission.

More results related to different settings of battery SOC thresholds are reported and discussed in Appendix B.
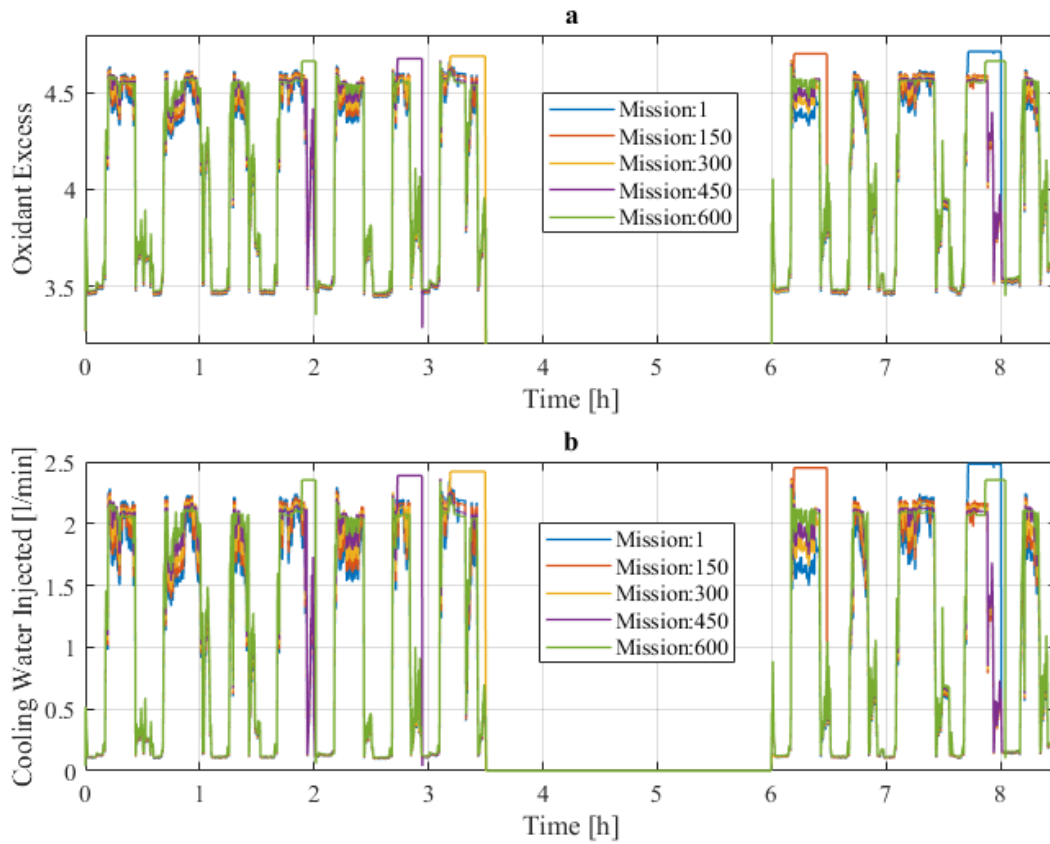
Figure 6.11: Trend of the main operating parameters of the thermal management of the single PEMFC stack along the mission cycle. (a) Shows the excess of oxidant required; (b) Shows the volumetric flow rate of water injected into the oxidant at the inlet.

Figure 6.12: Trend of thermal management system efficiency along the mission cycle.

Conclusions and future works

The maritime industry stands is facing substantial transformation, primarily driven by the need for sustainable and efficient energy solutions. In this context, the feasibility of integrating a Proton Exchange Membrane Fuel Cell (PEMFC) power system into long-haul ferry operations has been extensively studied.

A primary distinction of this research lies in its holistic approach to ship design. Instead of isolating the PEMFC from other systems, this methodology takes into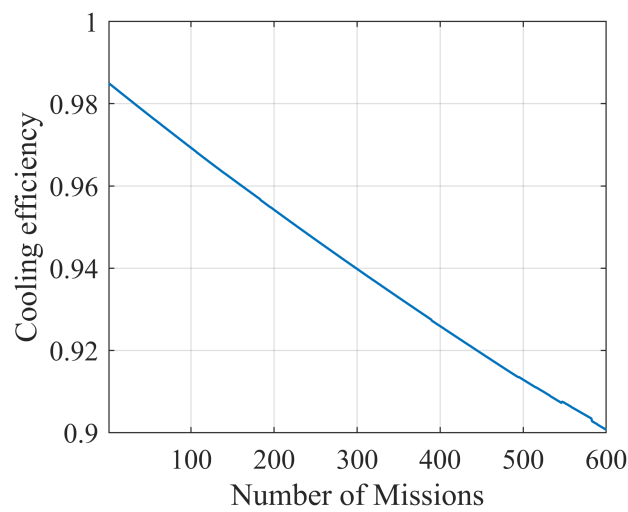 account the interconnections between the fuel cell and various other components on the vessel. This high level of interconnection necessitates an understanding that goes beyond individual component design, focusing instead on the synergetic optimization of the entire system. By doing so, it offers a comprehensive perspective, ensuring that any feasibility or design solution is not only technically sound but also practically viable in the real-world maritime setting. The chosen case study is a Norwegian ferry vessel of which data is available on the propulsive power demand, hotel loads and shore's power availability.

The simulation framework developed employs models with different complexity for each power system component, considering the level of interaction with the PEMFC. Through its detailed modeling of the PEMFC, battery storage, and the potential integration of a Variable Speed Diesel Engine Generator (VSDEG), it studies for 5100 operational hours (around one year of operation) considering how different components interact and influence each others. The fuel cell model's calibration and validation, using the characteristic curves of the PEMFC Ballard FCvelocity™ HD6 and reproducing experimental results, lends further reliability to the research.

Moreover, the research's adaptability, in considering both retrofit and new vessel designs, underscores its relevance to a broad spectrum of maritime applications. This flexibility ensures that the model remains pertinent regardless of whether one is working with historical power profile data or simulating from scratch.

The degradation estimation of the fuel cell system underscores the practical implications and the sizing critical issues of this technology. Recognizing that system degradation influences hydrogen consumption, energy efficiency, and ultimately operational costs, it becomes evident that the the proposed methodology aims to consider the feasibility study in terms of actual operational efficiency.

The hybrid PEM fuel cell and battery power generation system proposed to power

the case study ferry consists of 8 PEMFC Ballard FCvelocity™ HD6 (150kW), 3 Corvus Orca Energy packs (124kWh per pack). The optimization involved the sizing of power sources in order to obtain the solution that minimized fuel cell degradation. In addition, the optimization context was able to force the fuel cell to work with slower dynamics. Thus to reduce degradation due to unexpected load changes.

The first result to be discussed concerns fuel cell dynamics. Indeed, the sizing solutions where the fuel cell degraded the least were those where the FC could work with its natural dynamics. This is despite the fact that the fuel cell worked with less pronounced load variations. The fuel cell, when forced to slower dynamics, produces a higher average power that causes it to degrade faster than when working with its natural dynamics (τ_{FC} =0.947). This effect is reduced in solutions where energy is produced almost completely by FC.

The simulation, which lasts a few hours, records the performances of the power generation plant and of the energy management system for all 600 missions. The most important insight provided by the analysis is the increase in fuel consumption, which increases by 14.65% during the mission cycle. This result is critical for the sizing of the fuel tank.

The degraded fuel cell will be able to deliver the same power by working at higher currents, this means more fuel consumption, but also more oxidant flow rate to be delivered by the compressor. The excess oxidant used increases from 3.25 to 3.31 during the analysis. In addition, the average flow rate of injected water, which with air contributes to cell cooling and keeps the membrane moist, increases by 17.6%. In a non-holistic design, this information would have been neglected in sizing or empirical estimations for oversizing would have been adopted

Overall, the efficiency of the fuel cell system decreases by 5 percent. Variations in some parameters are minimal, but this is only due to the proper online energy management strategy adopted, which manages the on-board power sources and port energy.

The holistic approach allows this analysis to be repeated for different case studies and different optimisation objectives. This is performed by modifying the mission profile, vessel requirements and characteristic parameters of the expected fuel cell.

During the research activity carried out with the company Isotta Fraschini Motori SpA, the proposed methodology and the developed simulation framework were involved in different industrial projects. The first two projects dealt with proposed solutions for the vessels of an international port authority. The first project provided the estimation of propulsive loads in the case of a tugboat and the subsequent sizing of the hybrid propulsive layout. In addition, the sizing of the electric power generation system to meet the expected load of the electric motors was proposed. The analysis of the operational performance and cost of the fuel cell system on board of a port service vessel was studied in the second industrial application. In this case, the results produced revealed the underestimation of fuel tank size obtained through normal design methodology. In

addition, it was possible to provide the customer with a complete view of the system performance over a long operational period and when maintenance would be required. The third project focused on the preliminary design of a hybrid FC/Battery power generation system for stationary application. The latter highlighted the flexibility of the simulation and optimization environment for various applications where a large fuel cell is employed.

In conclusion, this research offers valuable insights into the potential and challenges of integrating fuel cell technology in the maritime industry. Employing a holistic approach lays the foundation for future studies that consider the broader implications of technology integration, moving beyond isolated evaluations. As the maritime industry continues its journey toward more sustainable horizons, such comprehensive methodologies will undoubtedly play a pivotal role in its future.

Possible future developments may involve both improvements to the model and experimental implications. The fuel cell model could be improved so as to provide results regarding the dynamics of the FC's membrane cooling and humidification system. The estimation of PEMFC degradation could complement recent advances in the literature. The relevance of this estimation for FC design promoted the experimental study of stress cycles and the study of analytical models to obtain the potential drops due to membrane degradation. An important development in this work concerns synergy with the experimental set-up. Indeed, experimentation on large-scale fuel cell plants, to study the performance of the stack and especially of the cooling system, is essential to obtain more reliable data on which to base simulations. Moreover, the proposed holistic approach is essential to provide the experimental set-up with the correct insights to study the fuel cell as part of a complex hybrid system. Thus, how it will work in the real application. Hence, integrating this simulation framework into a Hardware In the Loop (HIL) configuration could enable the achievement of important results on the most efficient solutions of integrating the fuel cell system, the future in terms of zero-emission power generation, within marine powertrains, especially those of ferries and other vessels operating on the coastal areas.

Chapter A

Integration for New Design Ships

This appendix describes the proposed approach to evaluate the propulsive power demand for a generic vessel, considering from the hull resistance to the propeller torque demand. The model is based on the definitions and approaches proposed in [135].

The Hull Resistance Model

The first design requirement is to define the user's drawn power curve, then estimate the resistance to motion as a function of the vessel's speed. A body moving in relative motion with respect to a fluid in which it is immersed is subject to a field of pressures normal to its surface and a set of stresses acting tangentially to the surface, as shown in Fig.A.1.

The next discussion takes into account the following assumptions:

- the ship advances through the water with constant velocity and directed horizontally according to the plane of symmetry (longitudinally); consequently, the resultant force is also longitudinal;

- there is a vertical component resulting from the actions applied by the fluid on the hull, which causes a vertical translation and a change in longitudinal trim; this component, for displacement ships, is of negligible magnitude;

- the ship moves at the separation surface between water and air, assumed to be at rest, and therefore perfectly flat;

- the ship's hull has a rough surface, the effect of which on the resistance to motion is treated by means of an additional term, compared with the smooth surface case;

- the resistances determined by water and air, respectively, are generally of very different orders of magnitude and can be treated separately.

Vessels can be classified with respect to the type of hull used, which radically changes the dynamics of the vehicle, planing and displacement, here proposed. The planing one receives a hydrodynamic buoyancy that lifts it out of the water by changing its weight relative to the mass of water it displaces, while the displacement one opens its course in the water and displaces an amount of water equal to its displacement.

The total resistance R_T of the hull is obtained from Eq(A.1), where R_F tangential or frictional resistance and R_P normal or pressure resistance. They are respectively defined in Eq.(A.2), where τ_x and p_x are the components according to the longitudinal direction, respectively, of the tangential stress and normal pressure acting on the wetted surface S of the hull, and dA the infinitesimal area on the latter, as shown in Fig.A.1.

$$R_T = R_F + R_P \tag{A.1}$$

$$R_F = \int_S \tau_x \, dA \,; \quad R_P = \int_S p_x \, dA \tag{A.2}$$
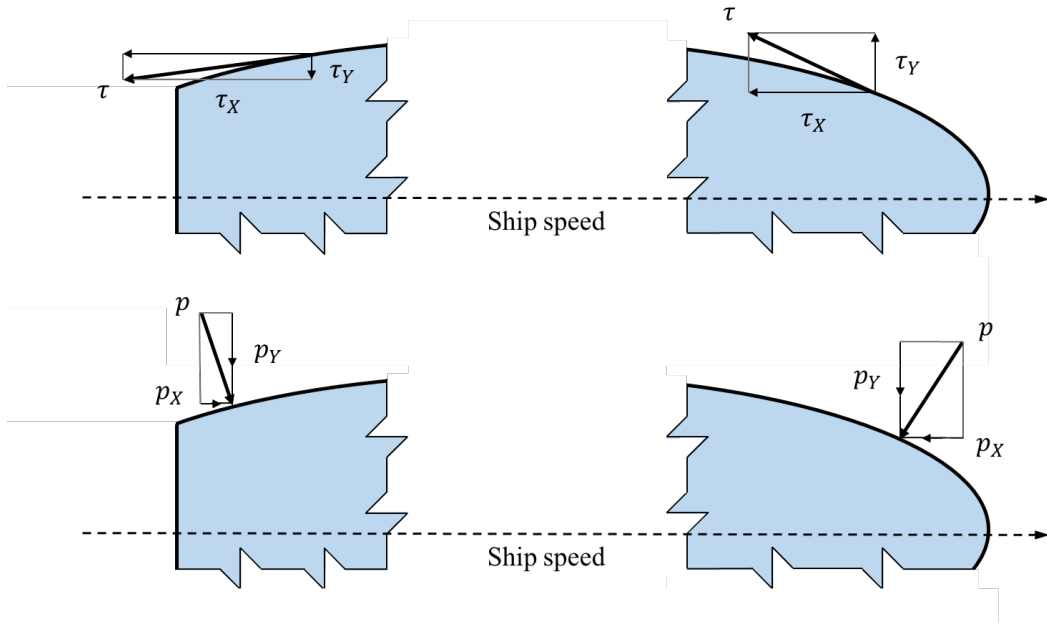
Figure A.1: Forces acting on the hull.

It is very important to note that while the τ_x component of the tangential stress is always oriented in the opposite direction to the speed with which the hull is advancing, the p_x component of the normal pressure has variable orientation; in particular, it is oriented in the opposite direction to the speed of the ship in the bow area, but is of the concordant sign with the speed of the ship in the aft part.

The friction resistance can be expressed as in Eq.(A.3), where R_F^0 is the frictional resistance of a flat plate of equal length and wetted area, k_F is an incremental form

factor of the tangential resistance.

$$R_F = (1 + k_F)R_F^0 \qquad (A.3)$$

The pressure resistance can be broken down as in Eq.(A.4).

$$R_P = R_{VP} + R_W \qquad (A.4)$$

R_{VP} is the viscous pressure resistance, due to the pressure fields that are generated in the viscous boundary layer due to the curvature of the current lines around the hull and any boundary layer detachments in the aft area; R_W, on the other hand, is the wave resistance, which is related to the energy required to create the wave formations that are generated around the surface-moving ship. Grouping the viscous origin components into a single term gives R_V, defined in Eq.(A.5), where k is the overall form factor. Thus the division of total resistance into viscous resistance and wave resistance results in Eq.(A.6)

$$R_F = (1 + k_F)R_F^0 + R_{VP} = R_F = (1 + k)R_F^0 \qquad (A.5)$$

$$R_T = R_V + R_W \qquad (A.6)$$

The first classification of resistance to motion is given by William Froude and is depicted in Eq.(A.7); the R_R component is called the residual resistance. Thus, as the Eq.(A.8) highlights, the residual resistance is the sum of all the resistance components that are present in the case of a ship hull, in addition to the resistance that would be exerted on an equivalent flat plate at the same speed.

$$R_T = R_F^0 + R_R \qquad (A.7)$$

$$R_R = k_F R_F^0 + R_{VP} + R_W \qquad (A.8)$$

Fig.A.2 provides a clear schematic of how the forces acting on the hull are divided.

TOTAL RESISTANCE					
Tangential (or frictional) resistance		Normal (or pressure) resistance			
Flat plate friction	Tangential shape effect	Boundary layer enlargement	Boundary layer separation	Wavy field	Breaking waves
Flat plate friction resistance	Residual resistance				
	Form resistance			Wave resistance	
Friction resistance		Viscous pressure resistance			
Viscous resistance					

Figure A.2: Diagram of the classification of forces acting on the hull.

Often, instead of resistances, it is preferred to use the dimensionless form of resistance coefficients, which have the structure of Newton numbers (C_i); Eq.(A.9) describes the application for the generic resistance R_i, where ρ is the density of water, S is the area of the hull surface and u is the speed of the ship.

$$C_i = \frac{R_i}{12\rho S u^2} \qquad (A.9)$$

it is necessary to state and explain the main hull parameters that influence the resistance to motion in calm water, before presenting the methods used for the purpose of estimating these resistances.

Geometric parameters, Fig.A.3:

- $\bigtriangledown = V[m^3]$: Volume of the submerged hull;

- $L_{wl}[m]$: Length of the immersed hull;

- $B_{wl}[m]$: Maximum width of the immersed cross section;

- $T[m]$: Hull immersion;

- $S[m^2]$: Wetted surface area of the hull;

- $A_x[m^2]$: Surface area of the immersed cross section at the centerline.
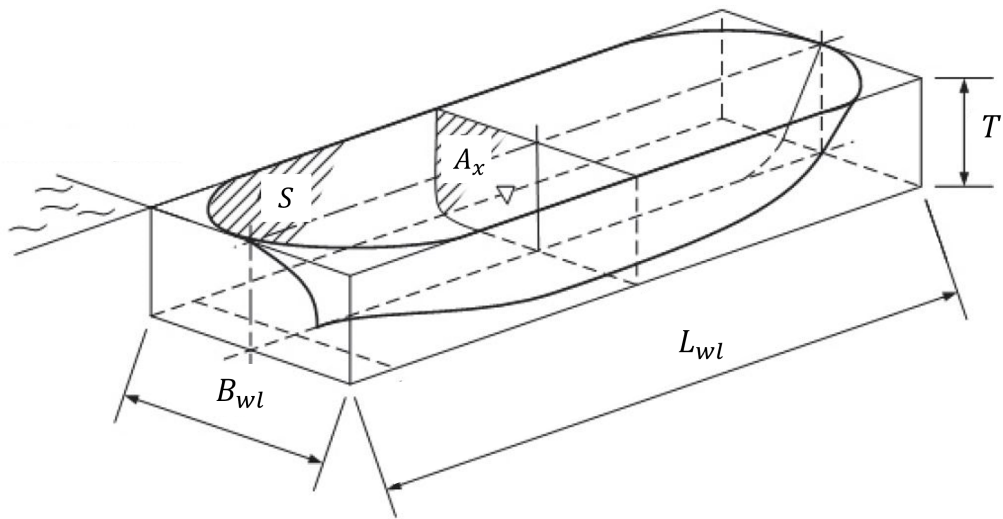

Figure A.3: Diagram of the classification of forces acting on the hull.

Fluid characteristic properties considered:

- $\rho[kg/m^3]$: Density of seawater;

- $\nu[m^2/s]$: Kinematic viscosity of seawater;

- T_h $[°C]$: Temperature of the water.

Parameters and coefficients of resistance:

- Re: Reynolds number $\frac{uL_{wl}}{\nu}$;

- Fr: Froude number $\frac{u}{(gL_{wl})^{0.5}}$;

- LV: Slenderness coefficient of Froude $\frac{L_{wl}}{V^{1/3}}$;

- Tq: Taylor quotient peer relative velocity, calculated with imperial units (u $[kn]$, L_{wl} $[ft]$) $\frac{u}{\sqrt{L_{wl}}}$;

- C_s: Coefficient of submerged surface area $\frac{S}{\sqrt{VL_{wl}}}$;

- C_t: Total resistance coefficient $\frac{R_T}{\sqrt{1/2\rho Su^2}}$;

- C_v: Volume coefficient $\frac{V}{L_{wl}^3}$;

- C_p: Prismatic coefficient, which allows the hull shapes to be evaluated numerically, is defined as the ratio of the actual immersed volume of the hull to the volume of the theoretical (prismoidal) solid, which is obtained by multiplying by the length at the waterline the area of the maximum section of the immersed volume of the hull $\frac{V}{L_{wl}A_x}$;

Fig.A.4 shows the prismatic coefficient C_p trend as a function of the Taylor quotient, Froude number and other geometric parameters.

Systematic series are part of empirical prediction methods, based on analysis of model-measured and/or experimental data, which can be coded easily. Using statistical analysis techniques, called multiple regression, a finite amount of experimental test results or experimental measurements can be reduced into a numerical expression, using a number of hull parameters as independent variables. These expressions can be used to predict the performance of new hull designs based on what has been measured on a group of existing ships.

To keep the accuracy of these equations as high as possible, the empirical data set has often been grouped into sets of similar hulls, so-called systematic hull sets. In generating a systematic series, the main shape parameters, enunciated above, are varied in a systematic way in order to be able to determine their effect on the resistance in still water. The accuracy of the resistance value that can be calculated for a generic hull can be more than satisfactory if the hull under consideration is very similar to the mother hull of the series.

Over the years, several systematic series have been created for as many fields of use. These have been chosen by following geometrical and kinematic criteria that could simulate the widest range of hulls among displacement-hulled and double-propeller ships.
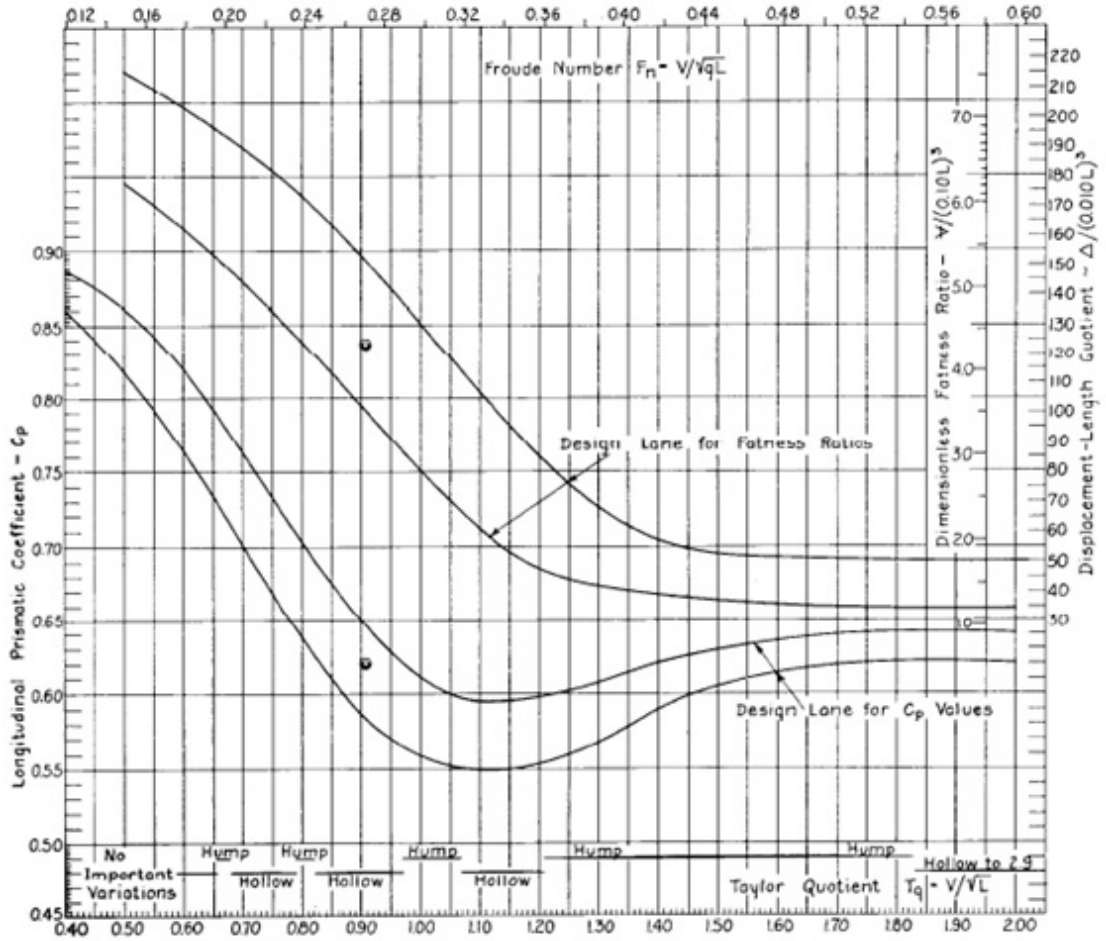
Figure A.4: Graph of the dependence between the Taylor quotient and the prismatic coefficient.

The Taylor-Gertler method is definitely the systematic series with the largest fields of application. These are summarized in the Tab.A.1.

The output provided by the systematic series is the parameter C_r, the coefficient of residual strength defined in Eq.(A.10). Fig.A.5 shows the trend of C_r tracked in Taylor-Gertler systematic series.

$$C_r = \frac{R_R}{1/2\rho S u^2} \tag{A.10}$$

Because of what was said above, once the residual drag coefficient is obtained, an estimate of the friction forces is needed to calculate the total resistance to hull motion. Taylor's proposed formulation assumes the friction coefficient C_f to be C_f^0, the friction coefficient for the flat plate of length L_{wl}.

The coefficient C_f^0 is estimated according to the ITTC'57 formulation in Eq.(A.11).

Table A.1: Taylor-Gertler systematic series constrains.

	Min	Max
T_q	0.30	2.00
F_r	0.09	0.60
B/T	2.25	3.75
C_p	0.48	0.86
C_v	1.00E-03	7.00E-3
LV	5.00	10.00
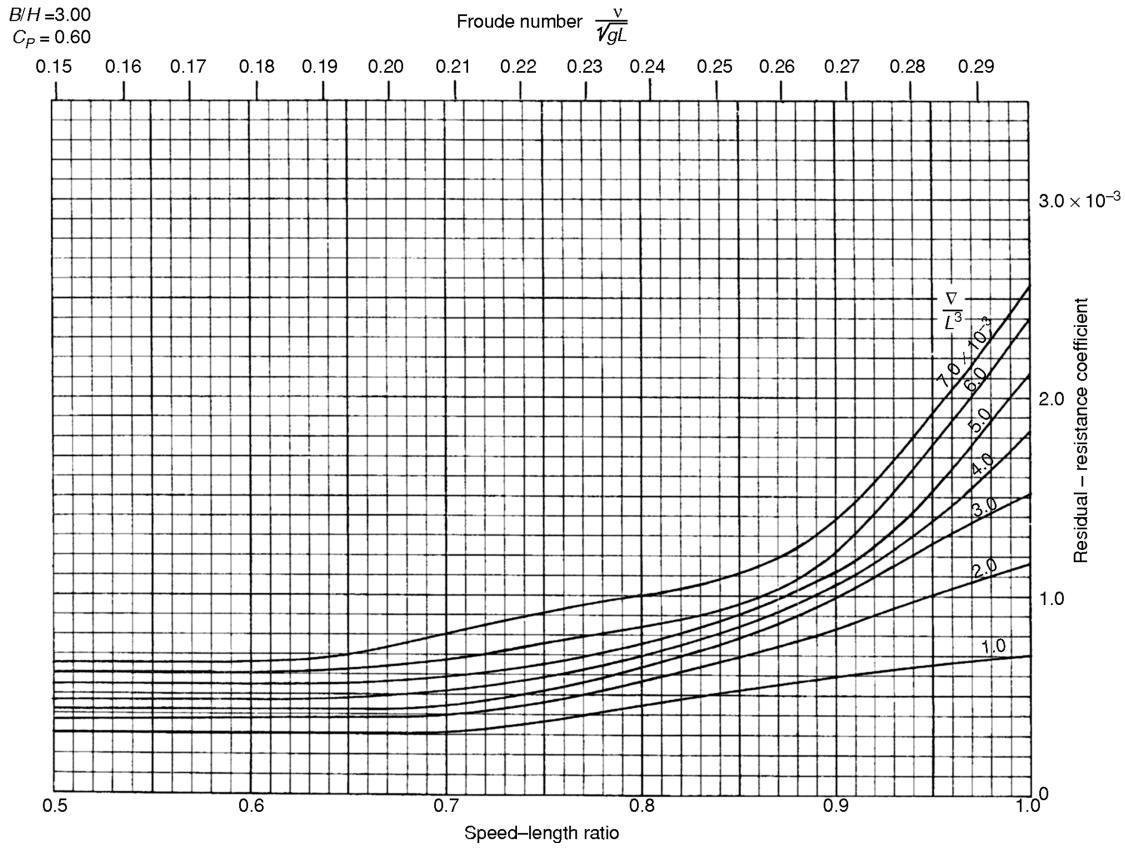
Figure A.5: Example of C_r trend in Taylor-Gertler systematic series.

$$C_f^0 = \frac{0.075}{(\log(Re) - 2)^2} \tag{A.11}$$

The coefficient of friction represents the dependence of drag on the relative velocity between hull and water. Thus C_f will be a function of the Reynolds number, as in Eq.(A.12).

$$C_f^0 = \frac{R_F}{1/2\rho S u^2} = f(\frac{uL}{\nu}) \tag{A.12}$$

The residual resistance coefficient represents, in Eq.(A.13), the dependence of the resistance of forces of gravitational nature, such as wave phenomena, considered in Froud's number.

$$C_r = \frac{R_R}{1/2\rho S u^2} = f(\frac{u}{\sqrt{gL}}) \tag{A.13}$$

For the calculation of R_T at velocities represented by a lower Froude number than that considered in the systematic series used, the residual drag appears negligible compared with the C_f^0 contribution. Therefore, the resistance for velocities corresponding to a Froude number less than 0.09 will be estimated by considering only the C_f^0 contribution.

The resultant of the resisting forces due to friction with air was formulated by Hughes from a series of systematic tests. This formulation, already carried over to the international system of measurement is described in Eq.(A.14).

$$R_A = 0.734 A_V u^2 \tag{A.14}$$

The evaluation of the cross-sectional area must take into account the shape diversity of the surfaces involved and is conventionally assumed as in Eq.(A.15).

$$A_V = 0.3 A_1 + A_2 \tag{A.15}$$

where A_1 represents the maximum cross-sectional area of the non-immersed hull, while A_2 takes into account the maximum cross-sectional area, of the ship, exposed to the wind current minus the hull, as clear in Fig.A.6.
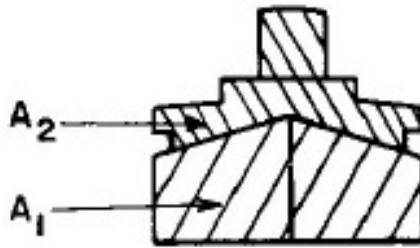
Figure A.6: Vessel's transverse projected area.

In the event that reference data for air-exposed surfaces are not available, the air resistance can be estimated as a percentage of that of the hull (about 4%). A similar argument can be made regarding the resistance of appendages. Typical appendages found on ships include rudders, outriggers, overhangs, masts, brackets, bilge keels, and water intakes, and all of these elements give rise to additional resistance. These can be summarized in the Tab.A.2.

The code provides tables , which schematize the resistance coefficients for the sys-

Table A.2: Value of appendage resistances as a percentage of hull resistance.

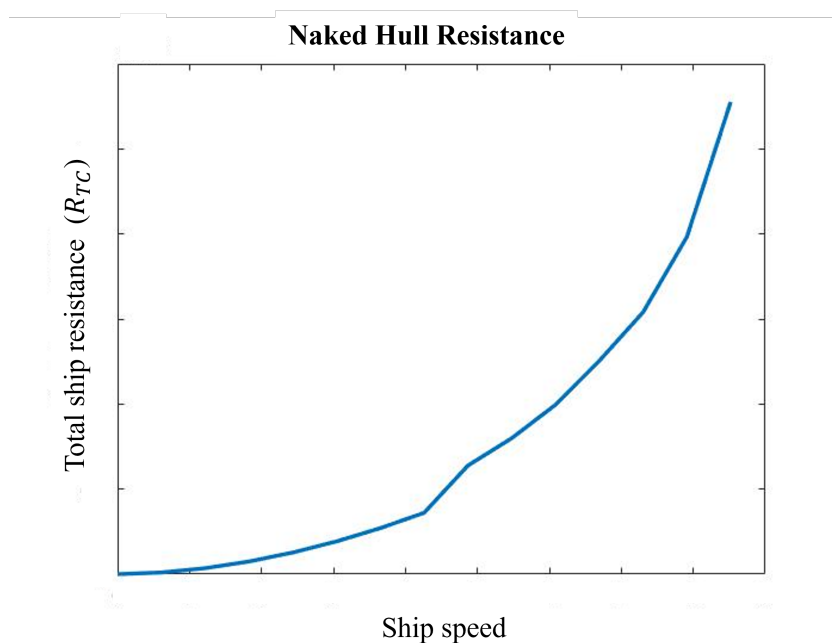| Vessel Type	% of naked resistance
Single screw	2-5
Large fast twin screw	8-14
Small fast twin screw	up to 25
Item	**% of naked resistance**
Bilge keels	2-3
Rudder	up to 5
Stabiliser fins	3
Shafting and brackets, or bossing	6-7
Condenser scoops	1

Naked Hull Resistance

Figure A.7: Total resistance force on the hull for a generic ship as function of the vessel's speed.

tematic Taylor-Gertler series, suitably digitized into Matlab matrices. Four matrices corresponding to the prismatic coefficients ranging from $C_p = 0.5$ to $C_p = 0.8$ were created.

The results produced by this approach are shown in Fig.A.7 and Fig.A.8 for a generic ship designed with a displacement hull.

Fig.A.7 shows the total resistance corrected by appendices and air friction resistances (R_{TC}). Fig.A.8 describes the total power demand (PE) related to the vessel's speed to meet the resistance forces on the hull. The PE was obtained by Eq.(A.16), where u_m is the longitudinal vessel's speed.
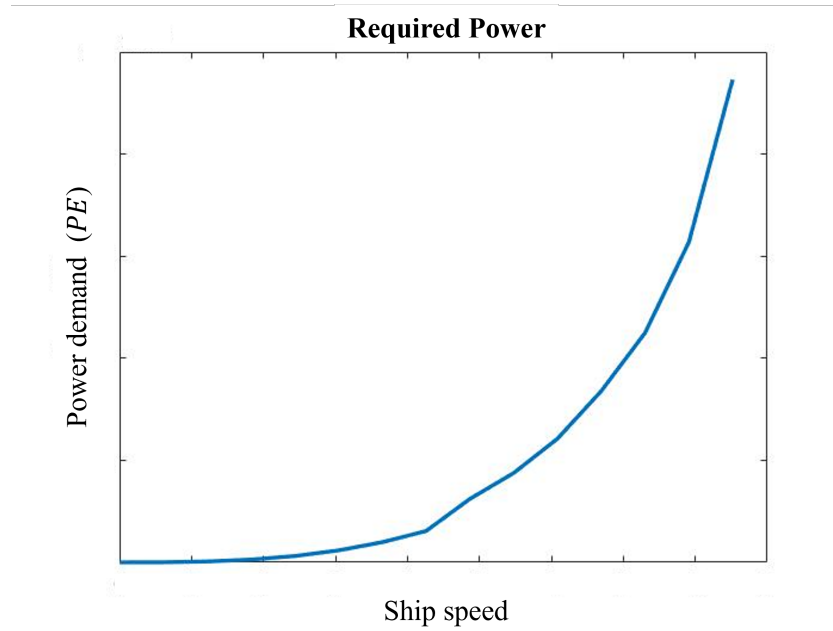
Figure A.8: Total power required from the hull for a generic ship as function of the vessel's speed.

$$PE = R_{TC}u_m \tag{A.16}$$

The Propeller Performance & Characteristics

All propulsion devices operate on the principle of providing work to a fluid according to Newton's laws. The acting force equals the rate of change of the produced momentum. Thus the thrust force TH can be written as in Eq.(A.17), where $\dot{m}$ is the mass flow rate passing through the propeller and V_a and V_2 are the forward velocity and fluid velocity downstream of the propeller, respectively, as shown in Fig.A.9.

$$TH = \dot{m}(V_2 - V_a) \tag{A.17}$$

The thrust and efficiency characteristics of a generic propeller is shown in Fig.A.10. From the Eq.A.17 it can be deduced that if the forward velocity tended toward the same value as the jet exit velocity, the thrust provided by the propeller would be zero. It is therefore important to define the speed advance ratio V_a/V_2.

Obviously, as the ratio of velocities increases, the thrust decreases. With regard to efficiency, there are two limiting situations:

- $V_a = V_2$: In this case the thrust is zero as is the power output ($P_p = TH\ V_a$). In this condition the losses due to viscous friction imply, in any case, a small power input. Therefore the efficiency will be $\eta_p = 0$;
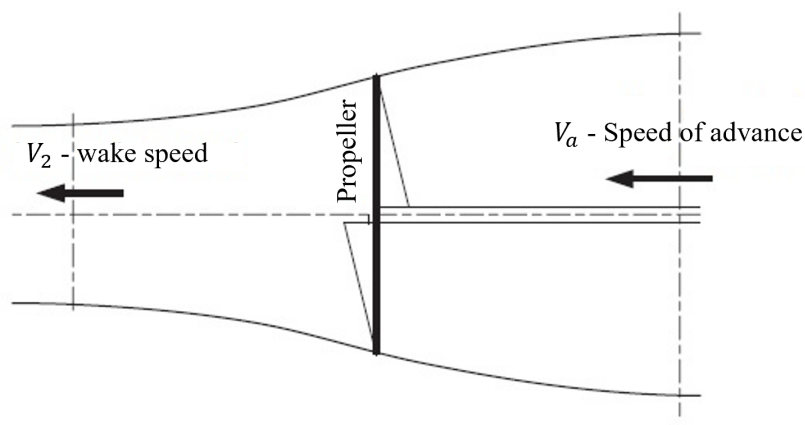
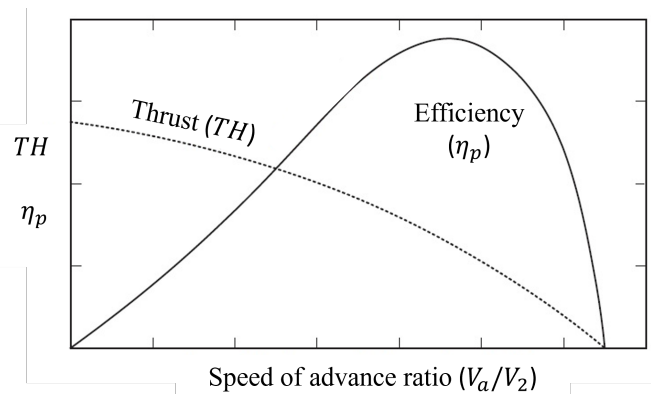Figure A.9: Schematic of the interaction between propeller and water.

Figure A.10: Propeller characteristics curve related to the speed advance ratio.

- $V_a = 0$: The ratio of velocities, in this case, is zero and thus the thruster provides maximum thrust. However, the power $P_p = TH \ V_a = 0$, so we will have $\eta_p = 0$.

The main parameters used in propeller design and performance prvision are listed below:

- P/D: Pitch to diameter ratio (face pitch ratio), used as a measure of propeller load, is usually constant along the blade radius. In reality, for reasons of harmonization of local hydrodynamic loading, in most naval propellers the pitch is not kept constant along the radius, but is generally reduced in the sections adjacent to the hub and at the end, since they are particularly critical for cavitation phenomena. In shipbuilding, the propeller pitch is conventionally defined at the section at a distance from the axis equal to 70% of the propeller radius, the area where the blade usually generates the greatest thrust;

- Blade area ratio: The values of the areas are represented in dimensionless form, relating them to the value of the helix disk area $A_0 = \frac{\pi D^2}{4}$.

Projected blade area ratio: A_p/A_0, B-C in Fig.A.11;

Developed blade area ratio (DAR): A_D/A_0, A-D in Fig.A.11;

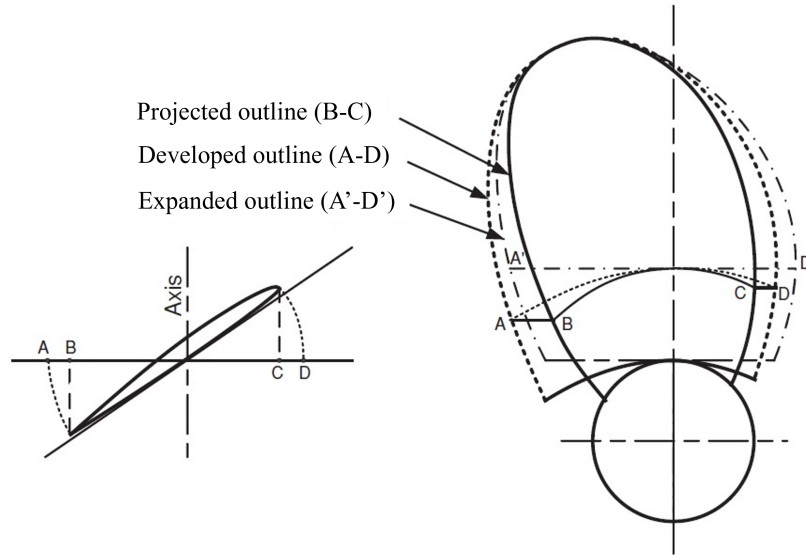Expanded blade area ratio (EAR): A_E/A_0, A'-D' in Fig.A.11.

Figure A.11: Projected, developed and expanded blade outline.

- D: The diameter of the propeller is that of the circumference bounded by the blade ends. It is convenient to take the maximum possible diameter value as a function of the aft shapes since propeller performance tends to improve proportionally as the diameter increases. However, it is necessary to provide a minimum clearance between the propeller end and the stern vault of not less than $0.2D$ to avoid harmful noise and vibration phenomena;

- z: The number of blades influences the amplitude and frequency of the pulsating forces caused by the propeller. In fact, all other factors being equal, an increase in the number of blades, dividing the total thrust over a greater number of components results in a reduction in the intensity of the exciting force and an increase in the frequency of the pulsations induced on the structure. In opposite, a greater number of blades generally causes a drop in propeller efficiency;

- t/D: Ratio of blade thickness to propeller diameter. The thickness considered is normally measured at the point where the generating line cuts the hub. Typical values, for fixed-pitch propellers, are between 0.18 and 0.20, while for variable-pitch propellers we can go up to about 0.25.

Propeller performance is defined by the thrust it delivers, the resistant torque, and the open water performance. These three quantities are evaluated by varying the coefficient of advance J, defined in Eq.(A.18).

$$J = \frac{V_a}{nD} \tag{A.18}$$

where n is the propeller speed in RPS, D is the propeller diameter, and V_a is the speed of advance of the thruster. The latter is derived from the product of the ship speed (V) and the wave factor (w) as in Eq.(A.19).

$$V_a = V(1 - w) \tag{A.19}$$

By dimensional analysis, it is possible to write the thrust (TH) and the resistant torque (Q) as a function of the parameters stated above, as in Eq.(A.20).

$$TH = f(D, V_a, n, \rho) Q = f(D, V_a, n, \rho) \tag{A.20}$$

The thrust and torque coefficients, respectively K_T and K_Q, are defined by the Eqs.(A.21) and (A.22).

$$K_T = \frac{TH}{\rho n^2 D^4} \tag{A.21}$$

$$K_Q = \frac{Q}{\rho n^2 D^5} \tag{A.22}$$

So, now it is possible to formulate the propeller efficiency in open water as in Eq.(A.23)

$$\eta_0 = \frac{THV_a}{2\pi nQ} = \frac{JK_T}{2\pi K_Q} \tag{A.23}$$

Fig.A.12 shows the trend of these coefficients and yield as a function of J for a given P/D ratio.

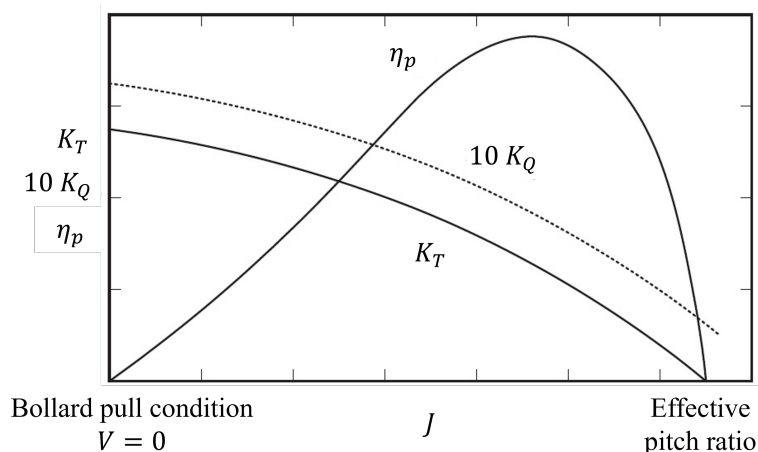

Figure A.12: Open water K_T and K_Q chart, for one pitch ratio.

Eqs.(A.24) and (A.25) describe the estimation, through polynomial regression, of K_T
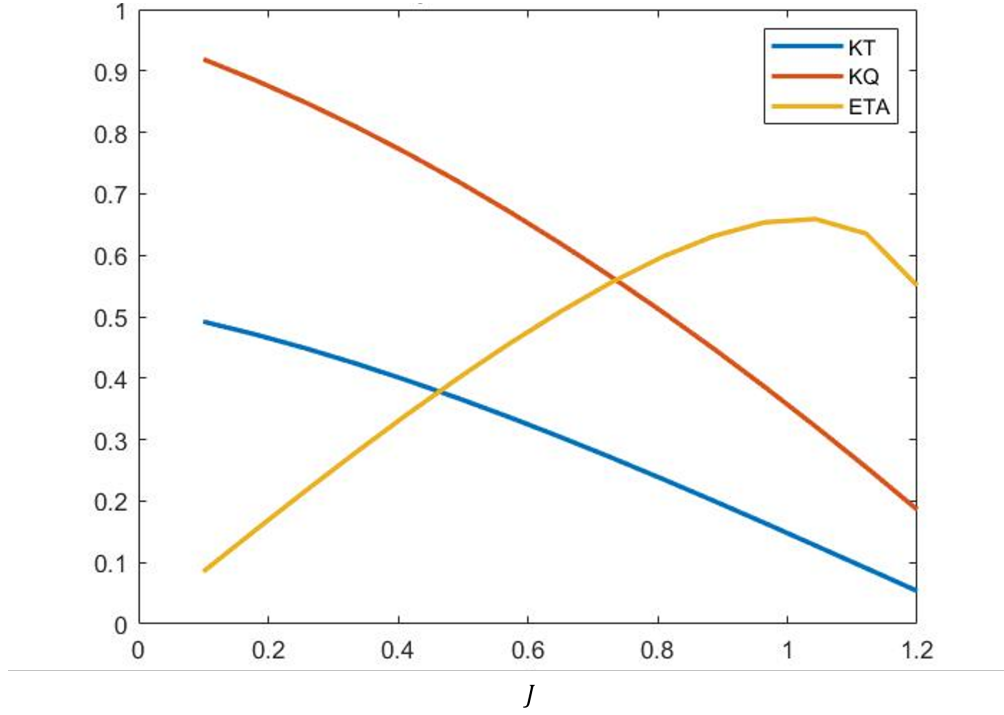
Figure A.13:   The characteristic curves, on normalized reference axe, for a generic propeller obtained by Wageningen's systematic series.

and K_Q in the Wageningen's method.

$$K_T = \sum (C_{s,t,u,v} J^s (P/D)^t (A_E/A_0)^u z^v) \tag{A.24}$$

$$K_Q = \sum (C_{s,t,u,v} J^s (P/D)^t (A_E/A_0)^u z^v) \tag{A.25}$$

The results of the proposed methodology are shown in Fig.A.13.

In addition, the weight and moment of inertia of the propeller are calculated through the code using the empirical formulas proposed by Schonherr.

- The total weight of the propeller by Eq.(A.26), where W_p is given in kilograms, the specific gravity of the material is given in kg/m^3, the radius R in meters, and t is the theoretical thickness of the blade on the axis of rotation:

$$W_p = 1.982\gamma \frac{t}{D} \frac{A_D}{A_0} R^3 \tag{A.26}$$

- The moment of inertia of the propeller, expressed in kgm^2 by Eq.(A.27):

$$I_p = 0.2745 W_p R^2 \tag{A.27}$$

Chapter B

Extra Results

This section describes the results obtained from simulating the same case study, but imposing different settings on the EMS. The following outcomes were presented in [136] in occasion of the 2023 IEEE Energy Conversion Conference and Expo.

In this work SOC_0 is set to 0.4, SOC_M is 0.8 and SOC_m is equal to 0.2. These parameters were chosen based on the limits of battery usage reported in the technical literature. Full pack storage was not allowed, as shown in Chapter 6, but the EMS, once the battery reaches 80% of its capacity, does not allow further energy harvesting.

Fig.B.1 shows the power output of the hybrid system, where the negative values of battery power corresponds to storage charging. Moreover, the same figure describes the energy that the EMS chooses to take from the shore grid. The bottom part of Fig.B.1 shows the trend of SOC_{act}, which ends the mission by storing energy, and the efficiency of the PEMFC system, which along the mission profile remains stable between 43.7% and 53.7%.

Fig.B.2 depicts the effect of the degradation on the battery SOC and the PEMFC efficiency during the 600 missions simulation. The efficiency of the fuel cell system never drops under 38.7%. The energy storage capacity trend describes better how the EMS changes its approach to the mission taking into account the FC potential lost.

Fig.B.3 provides a significant results on the strategy adopted by the EMS during the test cycle showing the percentage of effective navigation time spent in each EMS state. SOC_{act} never drops under 20%, thus the Low SOC Mode was never triggered. Indeed, the Single Direction Batt. is active for the most of the time. The PEMFC degradation increments the energy storage exploitation, reason why the time spent in Default Navigation and Cold Ironing significantly increases after the 400th mission.

Finally, Fig.B.4 shows the degradation of the single PEMFC limit potential from the rated value of $730V$ to $677V$. The total H_2 consumption for a single mission increase from $0.1918kg$ to $0.2071kg$. An immediate effect of choosing the project solution that minimizes degradation is the capability to operate for 5100 hours, experiencing an increase in consumption of only 7.4%. In contrast, the energy storage, working in Single
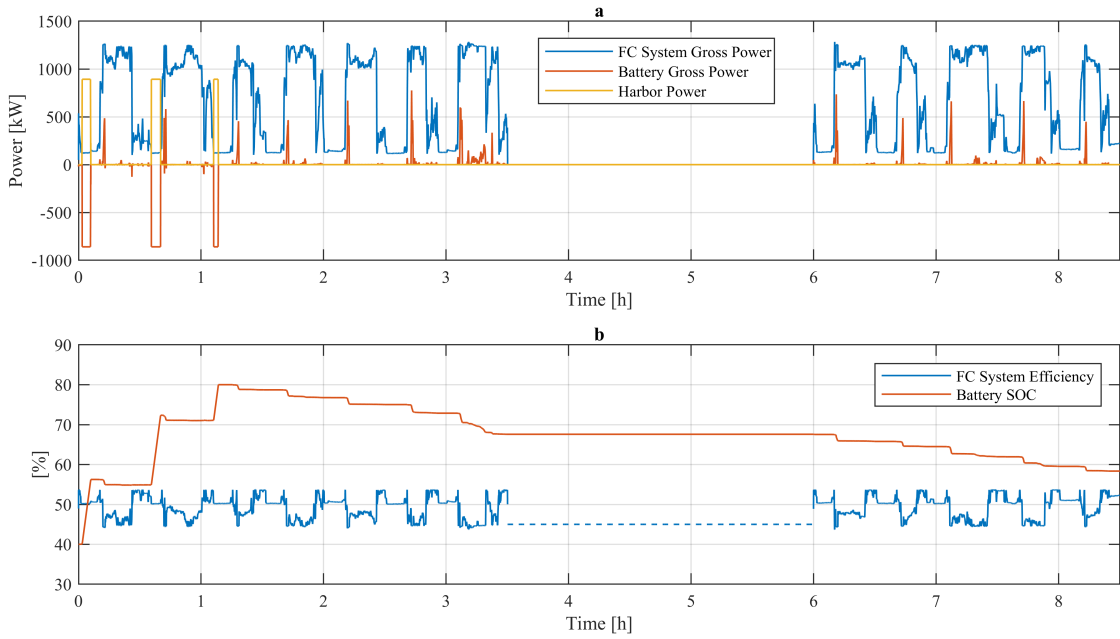
Figure B.1: a - Mission power profiles of the FC system and battery gross power output and the amount of power taken from the harbour grid; b - Energy storage capacity and FC system efficiency along the first mission.
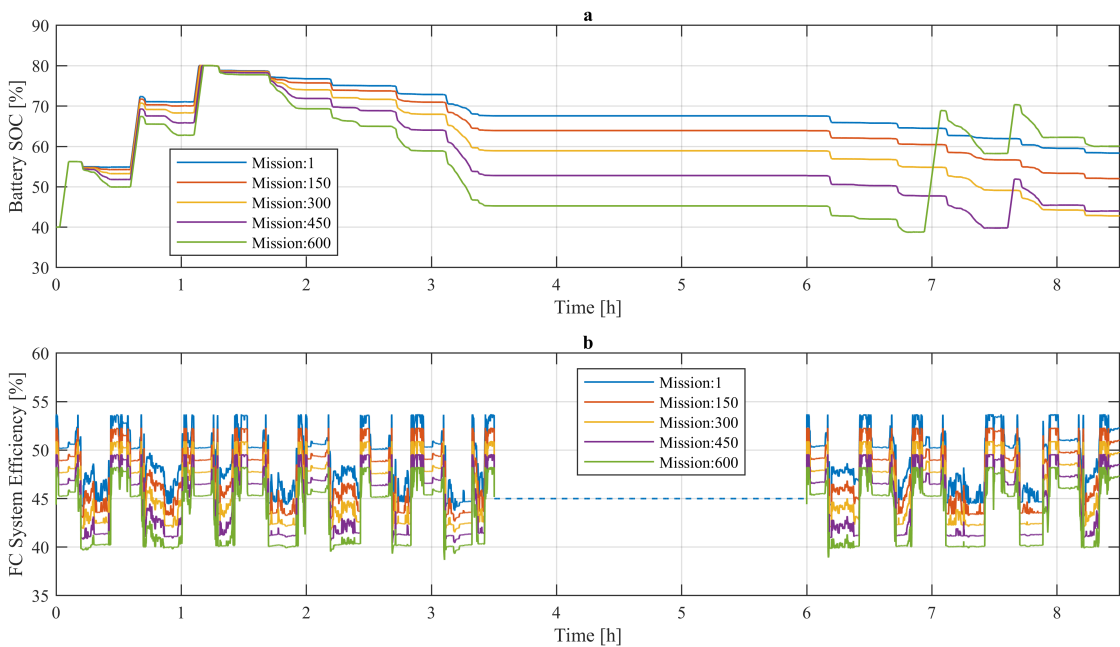
Figure B.2: a - Effect of degradation on the battery SOC along the test simulated; b - Effect of degradation on the PEMFC efficiency along the test simulated.
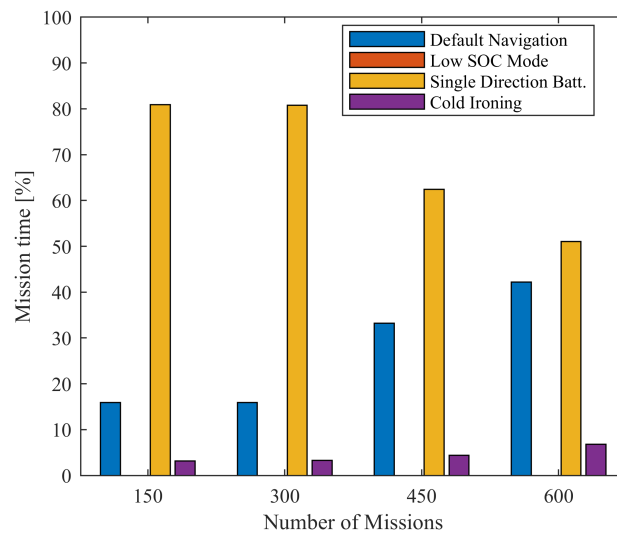
Figure B.3: Effective navigation time for each of the EMS states.

Direction Batt. mode for most of the operation time, help in peak shaving compensating the difference between the FC output power and the actual demand, but can not store the energy in excess as in Default Navigation mode. The PEMFC degradaton, in this case, is slightly worse relate to the results presented in Chapter 6.
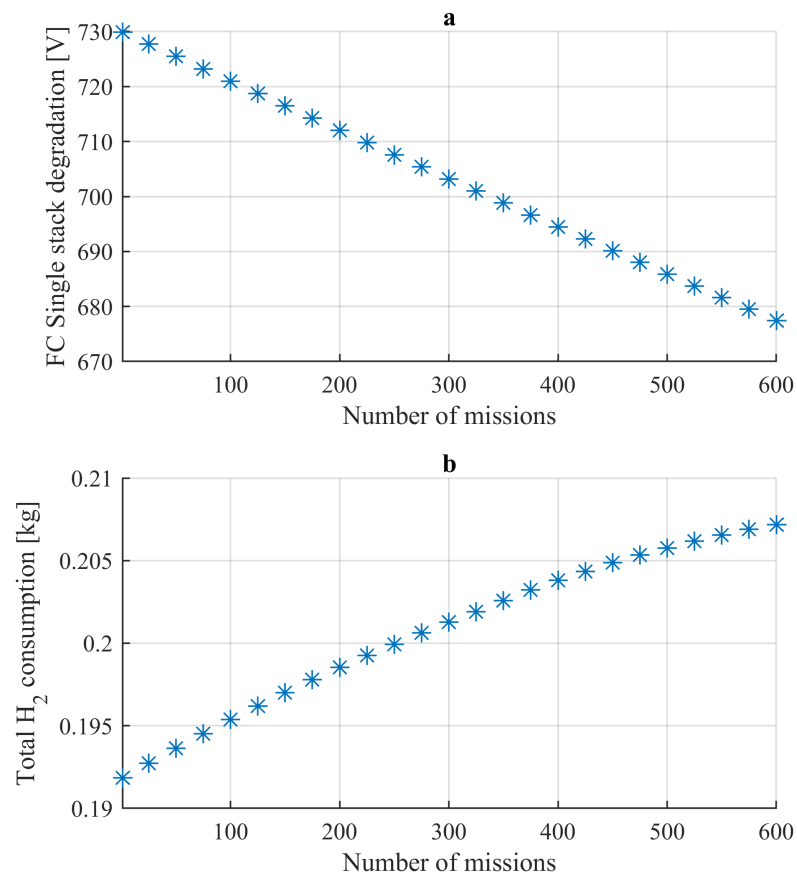
Figure B.4: a - PEMFC Ballard FCvelocity™ HD6 limit potential degradation along the test cycle; b - Total hydrogen consumed in a single mission along the test cycle.

References

[1] K. Calvin, et. al, IPCC, 2023: Climate Change 2023: Synthesis Report. Contribution of Working Groups I, II and III to the Sixth Assessment Report of the Intergovernmental Panel on Climate Change [Core Writing Team, H. Lee and J. Romero (eds.)]. IPCC, Geneva, Switzerland., Tech. rep., Intergovernmental Panel on Climate Change (IPCC), edition: First (2023). doi:10.59327/IPCC/AR6-9789291691647.
URL https://www.ipcc.ch/report/ar6/syr/

[2] W. L. Hare, W. Cramer, M. Schaeffer, A. Battaglini, C. C. Jaeger, Climate hotspots: key vulnerable regions, climate change and limits to warming (2011). doi:https://doi.org/10.1007/s10113-010-0195-4.

[3] A. Méjean, C. Guivarch, J. Lefèvre, M. Hamdi-Cherif, The transition in energy demand sectors to limit global warming to 1.5 c, Energy Efficiency 12 (2019) 441–462. doi:https://doi.org/10.1007/s12053-018-9682-0.

[4] J. Rogelj, G. Luderer, R. C. Pietzcker, E. Kriegler, M. Schaeffer, V. Krey, K. Riahi, Energy system transformations for limiting end-of-century warming to below 1.5 c, Nature Climate Change 5 (6) (2015) 519–527. doi:https://doi.org/10.1038/nclimate2572.

[5] L. Nastase, C. Negru, F. Pop, Understanding and Making Sense of Maritime Navigation Datasets, in: 2018 IEEE 14th International Conference on Intelligent Computer Communication and Processing (ICCP), IEEE, Cluj-Napoca, 2018, pp. 357–364. doi:10.1109/ICCP.2018.8516607.
URL https://ieeexplore.ieee.org/document/8516607/

[6] D. Kramel, H. Muri, Y. Kim, R. Lonka, J. B. Nielsen, A. L. Ringvold, E. A. Bouman, S. Steen, A. H. Strømman, Global Shipping Emissions from a Well-to-Wake Perspective: The MariTEAM Model, Environmental Science & Technology 55 (22) (2021) 15040–15050. doi:10.1021/acs.est.1c03937.
URL https://pubs.acs.org/doi/10.1021/acs.est.1c03937

[7] Y. Yuan, J. Wang, X. Yan, B. Shen, T. Long, A review of multi-energy hybrid power system for ships, Renewable and Sustainable Energy Reviews 132 (2020) 110081. doi:10.1016/j.rser.2020.110081.
URL https://linkinghub.elsevier.com/retrieve/pii/S1364032120303725

[8] E. Czermański, G. T. Cirella, Energy transition in maritime transport: Solutions and costs, in: Human Settlements: Urbanization, Smart Sector Development, and Future Outlook, Springer, 2021, pp. 79–88.

[9] M. Ram, D. Bogdanov, A. Aghahosseini, S. Khalili, M. Child, M. Fasihi, T. Traber, C. Breyer, European energy system based on 100% renewable energy–transport sector, Mobilität der Zukunft: Intermodale Verkehrskonzepte (2021) 519–562.

[10] T.-H. Joung, S.-G. Kang, J.-K. Lee, J. Ahn, The IMO initial strategy for reducing Greenhouse Gas(GHG) emissions, and its follow-up actions towards 2050, Journal of International Maritime Safety, Environmental Affairs, and Shipping 4 (1) (2020) 1–7. doi:10.1080/25725084.2019.1707938.
URL   https://www.tandfonline.com/doi/full/10.1080/25725084.2019.1707938

[11] DNV, Achieving the imo decarbonization goals, accessed on 09 26, 2023 (2020).
URL   https://www.dnv.com/expert-story/maritime-impact/How-newbuilds-can-comply-with-IMOs-2030-CO2-reduction-targets.html

[12] INTERFERRY, Interferry study reveals ferry industry's huge economic impact, accessed on 09 26, 2023 (2021).
URL https://interferry.com/2021/10/12/interferry-study-reveals-ferry-industrys-h

[13] Siemens, decarbonizing-marine-transport.pdf, Tech. rep., Siemens (2022).

[14] P. Wu, R. Bucknall, Hybrid fuel cell and battery propulsion system modelling and multi-objective optimisation for a coastal ferry, International Journal of Hydrogen Energy 45 (4) (2020) 3193–3208. doi:10.1016/j.ijhydene.2019.11.152.
URL https://linkinghub.elsevier.com/retrieve/pii/S0360319919343757

[15] Z. G. Ayalke, A. Şişman, K. Akpinar, Shoreline extraction and analyzing the effect of coastal structures on shoreline changing with remote sensing and geographic information system: Case of Samsun, Turkey, Regional Studies in Marine Science 61 (2023) 102883. doi:https://doi.org/10.1016/j.rsma.2023.102883.
URL   https://www.sciencedirect.com/science/article/pii/S2352485523000725

[16] E. Commission, Third Annual Report from the European Commission on CO2 Emissions from Maritime Transport, Tech. rep., European Commission (2022).

URL https://climate.ec.europa.eu/system/files/2022-08/swd_2022_214_en_0.pdf

[17] A. Papanikolaou, Ship design: methodologies of preliminary design, Springer, 2014.

[18] G. Anaclerio, T. Capurso, M. Torresi, S. Camporeale, Influence of the injection timing on the mixture formation process in a spark-ignition hydrogen fuelled ice, SAE Technical Paper (2023). doi:https://doi.org/10.4271/2023-24-0079.

[19] V. Ceglie, M. Stefanizzi, T. Capurso, F. Fornarelli, S. M. Camporeale, Thermoacoustic combustion stability analysis of a bluff body-stabilized burner fueled by methane–air and hydrogen–air mixtures, Energies 16 (7) (2023) 3272.

[20] I. Karakitsos, G. Theotokatos, Modelling of diesel electric propulsion, in: Energy Efficient Ships, Royal Institution of Naval Architects, GBR, 2016, pp. 93–101. URL https://strathprints.strath.ac.uk/60124/

[21] H. P. Nguyen, A. T. Hoang, S. Nizetic, X. P. Nguyen, A. T. Le, C. N. Luong, V. D. Chu, V. V. Pham, The electric propulsion system as a green solution for management strategy of co2 emission in ocean shipping: A comprehensive review, International Transactions on Electrical Energy Systems 31 (11) (2021). doi:10.1002/2050-7038.12580.
URL https://onlinelibrary.wiley.com/doi/10.1002/2050-7038.12580

[22] R. Geertsma, R. Negenborn, K. Visser, J. Hopman, Design and control of hybrid power and propulsion systems for smart ships: A review of developments, Applied Energy 194 (2017) 30–54. doi:10.1016/j.apenergy.2017.02.060.
URL https://linkinghub.elsevier.com/retrieve/pii/S0306261917301940

[23] G. Sulligoi, A. Vicenzutti, V. Arcidiacono, Y. Khersonsky, Voltage stability in large marine integrated electrical and electronic power systems, in: 2015 IEEE Petroleum and Chemical Industry Committee Conference (PCIC), 2015, pp. 1–10. doi:10.1109/PCICON.2015.7435102.

[24] K. N. Topaloglou S, Paplambrou G, Energy management controller design for hybrid ship propulsion during transient operation, in: 28th CIMAC congress, Vol. 5, 2016, pp. 1–9. doi:10.1109/PCICON.2015.7435102.

[25] G. Sulligoi, S. Castellan, M. Aizza, D. Bosich, L. Piva, G. Lipardi, Active front-end for shaft power generation and voltage control in fremm frigates integrated power system: Modeling and validation, in: International Symposium on Power Electronics Power Electronics, Electrical Drives, Automation and Motion, 2012, pp. 452–457. doi:10.1109/SPEEDAM.2012.6264570.

[26] E. Ovrum, T. F. Bergh, Modelling lithium-ion battery hybrid ship crane operation, Applied Energy 152 (2015) 162–172. doi:https://doi.org/10.1016/j.apenergy.2015.01.066.
URL https://www.sciencedirect.com/science/article/pii/S0306261915001026

[27] A. Breijs, E. E. Amam, Energy management–adapt your engine to every mission., in: 13th International Naval Engineering Conference, 2016, p. 9.

[28] B. Zahedi, L. E. Norum, K. B. Ludvigsen, Optimized efficiency of all-electric ships by dc hybrid power systems, Journal of Power Sources 255 (2014) 341–354. doi:https://doi.org/10.1016/j.jpowsour.2014.01.031.
URL https://www.sciencedirect.com/science/article/pii/S0378775314000469

[29] X. P. N. e. a. A. T. Hoang, Power generation characteristics of a thermoelectric modules-based power generator assisted by fishbone-shaped fins: Part ii – effects of cooling water parameters, Energy Sources, Part A: Recovery, Utilization, and Environmental Effects 43 (3) (2021) 381–393. doi:10.1080/15567036.2019.1624891.

[30] E. K. Dedes, D. A. Hudson, S. R. Turnock, Assessing the potential of hybrid energy technology to reduce exhaust emissions from global shipping, Energy Policy 40 (2012) 204–218. doi:https://doi.org/10.1016/j.enpol.2011.09.046.
URL https://www.sciencedirect.com/science/article/pii/S030142151100735X

[31] A. Sciarretta, L. Serrao, P. C. Dewangan, P. Tona, E. N. D. Bergshoeff, C. Bordons, L. Charmpa, P. Elbert, L. Eriksson, T. Hofman, M. Hubacher, P. Isenegger, F. Lacandia, A. Laveau, H. Li, D. Marcos, T. Nüesch, S. Onori, P. Pisu, J. Rios, E. Silvas, M. Sivertsson, L. Tribioli, A.-J. v. d. Hoeven, M. Wu, A control benchmark on the energy management of a plug-in hybrid electric vehicle, Control Engineering Practice 29 (2014). doi:https://doi.org/10.1016/j.conengprac.2013.11.020.
URL https://www.sciencedirect.com/science/article/pii/S0967066113002323

[32] F. Wang, Z. Zhang, T. Ericsen, R. Raju, R. Burgos, D. Boroyevich, Advances in power conversion and drives for shipboard systems, Proceedings of the IEEE 103 (12) (2015) 2285–2311. doi:10.1109/JPROC.2015.2495331.

[33] A. A. Ayu, Modeling power distribution system of an electric ship for design and control, Ph.D. thesis, Nanyang Technological University (2015). doi:10.32657/10356/65669.

[34] M. Huang, W. He, A. Incecik, A. Cichon, G. Królczyk, Z. Li, Renewable energy storage and sustainable design of hybrid energy powered ships: A case study, Journal of Energy Storage 43 (2021) 103266. doi:10.1016/j.est.2021.103266. URL https://linkinghub.elsevier.com/retrieve/pii/S2352152X21009610

[35] Z. Q. Zhu, W. Q. Chu, Y. Guan, Quantitative comparison of electromagnetic performance of electrical machines for hevs/evs, CES Transactions on Electrical Machines and Systems 1 (1) (2017) 37–47. doi:10.23919/TEMS.2017.7911107.

[36] P. Cheetham, C. Kim, L. Graber, S. Pamidi, Implementation of superconducting cables in medium voltage dc integrated power systems on all electric ships, in: IECON 2018 - 44th Annual Conference of the IEEE Industrial Electronics Society, 2018, pp. 3425–3430. doi:10.1109/IECON.2018.8591335.

[37] M. Butcher, R. Maltby, P. S. Parvin, Compact dc power and propulsion systems - the definitive solution?, in: 2009 IEEE Electric Ship Technologies Symposium, 2009, pp. 521–528. doi:10.1109/ESTS.2009.4906561.

[38] F. D. Kanellos, G. J. Tsekouras, J. Prousalidis, Onboard dc grid employing smart grid technology: challenges, state of the art and future prospects, IET Electrical Systems in Transportation 5 (1) (2015) 1–11. doi:https://doi.org/10.1049/iet-est.2013.0056.

[39] B. M. Huhman, J. M. Neri, D. A. Wetz, Design of a battery intermediate storage system for rep-rated pulsed power loads, in: 2013 IEEE Electric Ship Technologies Symposium (ESTS), 2013, pp. 1–5. doi:10.1109/ESTS.2013.6523703.

[40] M. Djibo, P. Moses, I. Flory, Fault protection considerations for mvdc shipboard power systems operating with pulsed-power loads, WSEAS Transactions on Power Systems 16 (2021). doi:https://doi.org/10.37394/232016.2021.16.14.

[41] N. Bayati, M. Savaghebi, Protection systems for dc shipboard microgrids, Energies 14 (17) (2021) 5319. doi:https://doi.org/10.3390/en14175319.

[42] G. Karthikeyan, D. P. Winston, A. Bhuvanesh, K. Gangatharan, Evaluation of faults in a dc grid-connected solar systems of ships, Marine Technology Society Journal 54 (4) (2020) 93–99. doi:https://doi.org/10.4031/MTSJ.54.4.8.

[43] V. C. Pham, H. Kim, J.-H. Choi, A. J. Nyongesa, J. Kim, H. Jeon, W.-J. Lee, Effectiveness of the speed reduction strategy on exhaust emissions and fuel oil consumption of a marine generator engine for dc grid ships, Journal of Marine Science and Engineering 10 (7) (2022) 979. doi:https://doi.org/10.4031/MTSJ.54.4.8.

[44] D. Bosich, A. Vicenzutti, R. Pelaschiar, R. Menis, G. Sulligoi, Toward the future: The mvdc large ship research program, in: 2015 AEIT International Annual Conference (AEIT), 2015, pp. 1–6. doi:10.1109/AEIT.2015.7415251.

[45] J. Hamilton, M. Negnevitsky, X. Wang, The potential of variable speed diesel application in increasing renewable energy source penetration, Energy Procedia 160 (2019) 558–565. doi:https://doi.org/10.1016/j.egypro.2019.02.206.
URL https://www.sciencedirect.com/science/article/pii/S1876610219312986

[46] J. F. Manwell, W. A. Stein, A. Rogers, J. G. McGowan, An investigation of variable speed operation of diesel generators in hybrid energy systems, Renewable Energy 2 (6) (1992) 563–571. doi:https://doi.org/10.1016/0960-1481(92)90019-Y.
URL https://www.sciencedirect.com/science/article/pii/096014819290019Y

[47] K. E. Holmefjord, L. Husdal, M. de Jongh, S. Torben, Variable-speed engines on wind farm support vessels, Journal of Marine Science and Engineering 8 (3) (2020). doi:10.3390/jmse8030229.
URL https://www.mdpi.com/2077-1312/8/3/229

[48] M. Mobarra, M. Rezkallah, A. Ilinca, Variable speed diesel generators: Performance and characteristic comparison, Energies 15 (2) (2022). doi:10.3390/en15020592.
URL https://www.mdpi.com/1996-1073/15/2/592

[49] R. Barbosa, M. Issa, S. Silva, A. Ilinca, Variable speed diesel electric generators: Technologies, benefits, limitations, impact on greenhouse gases emissions and fuel efficiency, Journal of Energy and Power Technology 4 (1) (2022) 1–21. doi:10.21926/jept.2201003.

[50] J. Habermaas, J. Thurner, Variable speed generator sets offer advantages for commercial ships, Retrieved November 28 (2020) 2022.
URL https://www.mtu-solutions.com/cn/en/technical-articles/2020/variable-speed-generator-sets-offer-advantages-for-commercial-sh.html

[51] O. B. Inal, J.-F. Charpentier, C. Deniz, Hybrid power and propulsion systems for ships: Current status and future challenges, Renewable and Sustainable Energy Reviews 156 (2022) 111965. doi:10.1016/j.rser.2021.111965.
URL https://linkinghub.elsevier.com/retrieve/pii/S1364032121012302

[52] C. A. Reusser, J. R. Pérez Osses, Challenges for zero-emissions ship, Journal of Marine Science and Engineering 9 (10) (2021) 1042. doi:10.3390/jmse9101042. URL https://www.mdpi.com/2077-1312/9/10/1042

[53] C. Karatuğ, Y. Durmuşoğlu, Design of a solar photovoltaic system for a ro-ro ship and estimation of performance analysis: A case study, Solar Energy 207 (2020) 1259–1268. doi:https://doi.org/10.1016/j.solener.2020.07.037. URL https://www.sciencedirect.com/science/article/pii/S0038092X20307696

[54] H. Wang, E. Oguz, B. Jeong, P. Zhou, Life cycle and economic assessment of a solar panel array applied to a short route ferry, Journal of Cleaner Production 219 (2019) 471–484. doi:https://doi.org/10.1016/j.jclepro.2019.02.124. URL https://www.sciencedirect.com/science/article/pii/S095965261930513X

[55] J. Kim, C. Park, Wind power generation with a parawing on ships, a proposal, Energy 35 (3) (2010) 1425–1432. doi:https://doi.org/10.1016/j.energy.2009.11.027. URL https://www.sciencedirect.com/science/article/pii/S0360544209005167

[56] L. Fagiano, M. Milanese, V. Razza, M. Bonansone, High-altitude wind energy for sustainable marine transportation, IEEE Transactions on Intelligent Transportation Systems 13 (2) (2012) 781–791. doi:10.1109/TITS.2011.2180715.

[57] N. Alujević, I. Ćatipović, S. Malenica, I. Senjanović, N. Vladimir, Ship roll control and power absorption using a u-tube anti-roll tank, Ocean Engineering 172 (2019) 857–870. doi:https://doi.org/10.1016/j.oceaneng.2018.12.007. URL https://www.sciencedirect.com/science/article/pii/S0029801818306450

[58] J. Hansson, S. Månsson, S. Brynolf, M. Grahn, Alternative marine fuels: Prospects based on multi-criteria decision analysis involving swedish stakeholders, Biomass and Bioenergy 126 (2019) 159–173. doi:https://doi.org/10.1016/j.biombioe.2019.05.008. URL https://www.sciencedirect.com/science/article/pii/S0961953419301710

[59] R. Tang, Z. Wu, X. Li, Optimal operation of photovoltaic/battery/diesel/cold-ironing hybrid energy system for maritime application, Energy 162 (2018) 697–714. doi:https://doi.org/10.1016/j.energy.2018.08.048.

URL   https://www.sciencedirect.com/science/article/pii/
S0360544218315688

[60] D. Strušnik, D. Brandl, H. Schober, J. Ferčec, J. Avsec, A simulation
model of the application of the solar STAF panel heat transfer and noise
reduction with and without a transparent plate: A renewable energy re-
view, Renewable and Sustainable Energy Reviews 134 (2020) 110149.
doi:https://doi.org/10.1016/j.rser.2020.110149.
URL   https://www.sciencedirect.com/science/article/pii/
S1364032120304408

[61] H. Lan, S. Wen, Y.-Y. Hong, D. C. Yu, L. Zhang, Optimal sizing of hybrid
PV/diesel/battery in ship power system, Applied Energy 158 (2015) 26–34.
doi:https://doi.org/10.1016/j.apenergy.2015.08.031.
URL   https://www.sciencedirect.com/science/article/pii/
S0306261915009575

[62] S. Wen, H. Lan, Y.-Y. Hong, D. C. Yu, L. Zhang, P. Cheng, Allocation of
ESS by interval optimization method considering impact of ship swinging on
hybrid PV/diesel ship power system, Applied Energy 175 (2016) 158–167.
doi:https://doi.org/10.1016/j.apenergy.2016.05.003.
URL   https://www.sciencedirect.com/science/article/pii/
S0306261916305852

[63] Y. Zhang, C. Yuan, Effects of marine environment on electrical output characteris-
tics of PV module, Journal of Renewable and Sustainable Energy 13 (5) (2021-09)
053701. doi:10.1063/5.0060201.
URL https://doi.org/10.1063/5.0060201

[64] A. De Marco, S. Mancini, C. Pensa, G. Calise, F. De Luca, et al., Flettner rotor
concept for marine applications: A systematic study, International Journal of Ro-
tating Machinery 2016 (2016). doi:https://doi.org/10.1155/2016/3458750.

[65] L. Talluri, D. K. Nalianda, K. G. Kyprianidis, T. Nikolaidis, P. Pi-
lidis, Techno economic and environmental assessment of wind assisted
marine propulsion systems, Ocean Engineering 121 (2016) 301–311.
doi:https://doi.org/10.1016/j.oceaneng.2016.05.047.
URL   https://www.sciencedirect.com/science/article/pii/
S0029801816301718

[66] R. Lu, J. W. Ringsberg, Ship energy performance study of three wind-assisted
ship propulsion technologies including a parametric study of the flettner rotor

technology, Ships and Offshore Structures 15 (3) (2020) 249–258. doi:10.1080/17445302.2019.1612544.

[67] R. Leloup, K. Roncin, M. Behrel, G. Bles, J.-B. Leroux, C. Jochum, Y. Parlier, A continuous and analytical modeling for kites as auxiliary propulsion devoted to merchant ships, including fuel saving estimation, Renewable Energy 86 (2016) 483–496. doi:https://doi.org/10.1016/j.renene.2015.08.036.
URL https://www.sciencedirect.com/science/article/pii/S0960148115302366

[68] R. Mo, H. Li, Hybrid energy storage system with active filter function for shipboard mvdc system applications based on isolated modular multilevel dc/dc converter, IEEE Journal of Emerging and Selected Topics in Power Electronics 5 (1) (2017) 79–87. doi:10.1109/JESTPE.2016.2642831.

[69] E. C. H. L. G. for Hydrogen, F. C. Technologies, Hydrogen energy and fuel cells: a vision of our future, Office for Official Publications of the European Communities, 2003.

[70] M.-J. Kim, H. Peng, Power management and design optimization of fuel cell/battery hybrid vehicles, Journal of Power Sources 165 (2) (2007) 819–832. doi:https://doi.org/10.1016/j.jpowsour.2006.12.038.
URL https://www.sciencedirect.com/science/article/pii/S0378775306025523

[71] T. Fletcher, R. Thring, M. Watkinson, An energy management strategy to concurrently optimise fuel consumption & PEM fuel cell lifetime in a hybrid vehicle, International Journal of Hydrogen Energy 41 (46) (2016) 21503–21515. doi:10.1016/j.ijhydene.2016.08.157.
URL https://linkinghub.elsevier.com/retrieve/pii/S0360319916325435

[72] R. K. Ahluwalia, X. Wang, A. G. Star, D. D. Papadias, Performance and cost of fuel cells for off-road heavy-duty vehicles, International Journal of Hydrogen Energy 47 (20) (2022) 10990–11006. doi:https://doi.org/10.1016/j.ijhydene.2022.01.144.
URL https://www.sciencedirect.com/science/article/pii/S0360319922002841

[73] L. Zheng, Y. Hou, W. Li, D. Hao, A data driven fuel cell life-prediction model for a fuel cell electric city bus, SAE International Journal of Advances and Current Practices in Mobility 3 (4) (2021) 1976–1984. doi:10.4271/2021-01-0739.
URL https://www.sae.org/content/2021-01-0739

[74] F. Cutrignelli, G. Saponaro, M. Stefanizzi, M. Torresi, S. M. Camporeale, Study of the effects of regenerative braking system on a hybrid diagnostic train, Energies 16 (2) (2023). doi:10.3390/en16020874.
URL https://www.mdpi.com/1996-1073/16/2/874

[75] Q. Li, W. Chen, Z. Liu, M. Li, L. Ma, Development of energy management system based on a power sharing strategy for a fuel cell-battery-supercapacitor hybrid tramway, Journal of Power Sources 279 (2015) 267–280. doi:10.1016/j.jpowsour.2014.12.042.
URL https://linkinghub.elsevier.com/retrieve/pii/S0378775314020709

[76] F. G. Aarskog, J. Danebergs, T. Strømgren, O. Ulleberg, Energy and cost analysis of a hydrogen driven high speed passenger ferry, International Shipbuilding Progress 67 (1) (2020) 97–123. doi:10.3233/ISP-190273.
URL https://www.medra.org/servlet/aliasResolver?alias=iospress&doi=10.3233/ISP-190273

[77] A. Letafat, M. Rafiei, M. Sheikh, M. Afshari-Igder, M. Banaei, J. Boudjadar, M. H. Khooban, Simultaneous energy management and optimal components sizing of a zero-emission ferry boat, Journal of Energy Storage 28 (2020) 101215. doi:10.1016/j.est.2020.101215.
URL https://linkinghub.elsevier.com/retrieve/pii/S2352152X19317177

[78] F. Ning, X. He, Y. Shen, H. Jin, Q. Li, D. Li, S. Li, Y. Zhan, Y. Du, J. Jiang, H. Yang, X. Zhou, Flexible and lightweight fuel cell with high specific power density, ACS Nano 11 (6) (2017) 5982–5991. doi:10.1021/acsnano.7b01880.
URL https://doi.org/10.1021/acsnano.7b01880

[79] S. J. Moura, J. B. Siegel, D. J. Siegel, H. K. Fathy, A. G. Stefanopoulou, Education on vehicle electrification: Battery systems, fuel cells, and hydrogen, in: 2010 IEEE Vehicle Power and Propulsion Conference, 2010, pp. 1–6. doi:10.1109/VPPC.2010.5729150.

[80] M. Stefanizzi, T. Capurso, G. Filomeno, M. Torresi, G. Pascazio, Recent combustion strategies in gas turbines for propulsion and power generation toward a zero-emissions future: Fuels, burners, and combustion techniques, Energies 14 (20) (2021) 6694. doi:https://doi.org/10.3390/en14206694.

[81] G. Anaclerio, T. Capurso, M. Torresi, S. M. Camporeale, Numerical characterization of hydrogen under-expanded jets with a focus on internal combustion engines applications, International Journal of Engine Research 24 (8) (2023) 3342–3358. doi:10.1177/14680874221148789.

[82] F. Anaclerio, G. Saponaro, E. Mancaruso, C. Mazzarella, F. Fornarelli, V. Magi, S. Camporeale, An experimental characterization of gasoline/ozone/air mixtures in spark ignition engines, SAE Technical Paper (2023). doi:https://doi.org/10.4271/2023-24-0039.

[83] L. Van Biert, M. Godjevac, K. Visser, P. Aravind, A review of fuel cell systems for maritime applications, Journal of Power Sources 327 (2016) 345–364. doi:10.1016/j.jpowsour.2016.07.007.
URL https://linkinghub.elsevier.com/retrieve/pii/S0378775316308631

[84] S. Dirkes, J. Leidig, P. Fisch, S. Pischinger, Prescriptive lifetime management for PEM fuel cell systems in transportation applications, part i: State of the art and conceptual design, Energy Conversion and Management 277 (2023) 116598. doi:10.1016/j.enconman.2022.116598.
URL https://linkinghub.elsevier.com/retrieve/pii/S0196890422013760

[85] Statista, Forecast breakdown of renewable hydrogen production costs worldwide from 2020 to 2030, Tech. rep., Statista (2021).
URL https://www.statista.com/statistics/1220812/global-hydrogen-production-cost-forecast-by-scenario/

[86] V. Cigolotti, M. Genovese, P. Fragiacomo, Comprehensive review on fuel cell technology for stationary applications as sustainable and efficient poly-generation energy systems, Energies 14 (16) (2021). doi:10.3390/en14164963.
URL https://www.mdpi.com/1996-1073/14/16/4963

[87] H. Chen, P. Pei, M. Song, Lifetime prediction and the economic lifetime of proton exchange membrane fuel cells, Applied Energy 142 (2015) 154–163. doi:10.1016/j.apenergy.2014.12.062.
URL https://linkinghub.elsevier.com/retrieve/pii/S0306261914013191

[88] P. Pei, Y. Meng, D. Chen, P. Ren, M. Wang, X. Wang, Lifetime prediction method of proton exchange membrane fuel cells based on current degradation law, Energy 265 (2023) 126341. doi:10.1016/j.energy.2022.126341.
URL https://linkinghub.elsevier.com/retrieve/pii/S0360544222032273

[89] T. Jahnke, G. Futter, A. Latz, T. Malkow, G. Papakonstantinou, G. Tsotridis, P. Schott, M. Gérard, M. Quinaud, M. Quiroga, A. Franco, K. Malek, F. Calle-Vallejo, R. Ferreira De Morais, T. Kerber, P. Sautet, D. Loffreda, S. Strahl, M. Serra, P. Polverino, C. Pianese, M. Mayur, W. Bessler, C. Kompis, Performance and degradation of proton exchange membrane fuel cells: State of the art in modeling from atomistic to system scale, Journal of Power Sources 304 (2016)

207–233. doi:10.1016/j.jpowsour.2015.11.041.
URL https://linkinghub.elsevier.com/retrieve/pii/S0378775315305395

[90] P. H. A. Nóbrega, A review of physics-based low-temperature proton-exchange membrane fuel cell models for system-level water and thermal management studies, Journal of Power Sources 558 (2023) 232585. doi:https://doi.org/10.1016/j.jpowsour.2022.232585.
URL https://www.sciencedirect.com/science/article/pii/S0378775322015622

[91] Y. Pan, H. Wang, N. P. Brandon, A fast two-phase non-isothermal reduced-order model for accelerating PEM fuel cell design development, International Journal of Hydrogen Energy 47 (91) (2022) 38774–38792. doi:10.1016/j.ijhydene.2022.09.044.
URL https://linkinghub.elsevier.com/retrieve/pii/S0360319922041210

[92] Z. Abdin, C. Webb, E. Gray, Pem fuel cell model and simulation in matlab–simulink based on physical parameters, Energy 116 (2016) 1131–1144. doi:10.1016/j.energy.2016.10.033.
URL https://linkinghub.elsevier.com/retrieve/pii/S0360544216314542

[93] F. Musio, F. Tacchi, L. Omati, P. Gallo Stampino, G. Dotelli, S. Limonta, D. Brivio, P. Grassini, PEMFC system simulation in MATLAB-simulink® environment, International Journal of Hydrogen Energy 36 (13) (2011) 8045–8052. doi:10.1016/j.ijhydene.2011.01.093.
URL https://linkinghub.elsevier.com/retrieve/pii/S0360319911001388

[94] E. Gadducci, T. Lamberti, M. Rivarolo, L. Magistri, Experimental campaign and assessment of a complete 240-kW proton exchange membrane fuel cell power system for maritime applications, International Journal of Hydrogen Energy 47 (53) (2022) 22545–22558. doi:https://doi.org/10.1016/j.ijhydene.2022.05.061.
URL https://www.sciencedirect.com/science/article/pii/S036031992202078X

[95] L. Yin, Q. Li, W. Chen, T. Wang, H. Liu, Experimental analysis of optimal performance for a 5 kW PEMFC system, International Journal of Hydrogen Energy 44 (11) (2019) 5499–5506. doi:https://doi.org/10.1016/j.ijhydene.2018.08.157.
URL https://www.sciencedirect.com/science/article/pii/S0360319918327320

[96] I. S. Lim, J. Y. Park, E. J. Choi, M. S. Kim, Efficient fault diagnosis method of PEMFC thermal management system for various current densities, International

Journal of Hydrogen Energy 46 (2) (2021) 2543–2554. doi:10.1016/j.ijhydene.2020.10.085.
URL https://linkinghub.elsevier.com/retrieve/pii/S0360319920338878

[97] J. Xu, C. Zhang, R. Fan, H. Bao, Y. Wang, S. Huang, C. S. Chin, C. Li, Modelling and control of vehicle integrated thermal management system of PEM fuel cell vehicle, Energy 199 (2020) 117495. doi:10.1016/j.energy.2020.117495.
URL https://linkinghub.elsevier.com/retrieve/pii/S0360544220306022

[98] W.-M. Yan, M.-S. Zeng, T.-F. Yang, C.-Y. Chen, M. Amani, P. Amani, Performance improvement of air-breathing proton exchange membrane fuel cell stacks by thermal management, International Journal of Hydrogen Energy 45 (42) (2020) 22324–22339. doi:10.1016/j.ijhydene.2019.08.146.
URL https://linkinghub.elsevier.com/retrieve/pii/S0360319919331647

[99] P. S. Oruganti, Q. Ahmed, D. Jung, Effects of thermal and auxiliary dynamics on a fuel cell based range extender, in: WCX World Congress Experience, 2018, pp. 2018–01–1311. doi:10.4271/2018-01-1311.
URL https://www.sae.org/content/2018-01-1311/

[100] L. Xing, W. Xiang, R. Zhu, Z. Tu, Modeling and thermal management of proton exchange membrane fuel cell for fuel cell/battery hybrid automotive vehicle, International Journal of Hydrogen Energy 47 (3) (2022) 1888–1900. doi:10.1016/j.ijhydene.2021.10.146.
URL https://linkinghub.elsevier.com/retrieve/pii/S036031992104177X

[101] J. Hoeflinger, P. Hofmann, Air mass flow and pressure optimisation of a pem fuel cell range extender system, International Journal of Hydrogen Energy 45 (53) (2020) 29246–29258. doi:10.1016/j.ijhydene.2020.07.176.
URL https://linkinghub.elsevier.com/retrieve/pii/S0360319920327841

[102] R. O'Hayre, S.-W. Cha, Fuel Cell Fundamentals, Wiley, 2016. doi:https://doi.org/10.1002/9781119191766.biblio.

[103] C. O'Brien, Materials for pem fuel cells 2023-2033, Tech. rep., IDTechEx (2023).

[104] X. Wei, R.-Z. Wang, W. Zhao, G. Chen, M.-R. Chai, L. Zhang, J. Zhang, Recent research progress in pem fuel cell electrocatalyst degradation and mitigation strategies, EnergyChem 3 (5) (2021) 100061. doi:https://doi.org/10.1016/j.enchem.2021.100061.
URL https://www.sciencedirect.com/science/article/pii/S2589778021000117

[105] H. C. Lau, Decarbonization of asean's power sector: A holistic approach, Energy
      Reports 9 (2023) 676–702. doi:https://doi.org/10.1016/j.egyr.2022.11.
      209.
      URL   https://www.sciencedirect.com/science/article/pii/
      S2352484722025963

[106] A. Papanikolaou, Holistic ship design optimization, Computer-Aided De-
      sign 42 (11) (2010) 1028–1044, computer aided ship design: Some re-
      cent results and steps ahead in theory, methodology and practice.
      doi:https://doi.org/10.1016/j.cad.2009.07.002.
      URL   https://www.sciencedirect.com/science/article/pii/
      S0010448509001973

[107] HOLIstic optimisation of SHIP design and operation for life cycle.
      URL https://cordis.europa.eu/project/id/689074

[108] HOLISHIP.
      URL http://www.holiship.eu/

[109] A. D. Papanikolaou, Holistic approach to ship design, Journal of Marine Science
      and Engineering 10 (11) (2022). doi:10.3390/jmse10111717.
      URL https://www.mdpi.com/2077-1312/10/11/1717

[110] J. Marzi, A. Papanikolaou, P. Corrignan, G. Zaraphonitis, S. Harries, Holistic ship
      design for future waterborne transport, 7th Transport Research Arena TRA 2018
      (TRA 2018) (2018).

[111] A. D. Papanikolaou, A Holistic Approach to Ship Design, Springer Cham, 2019.
      doi:https://doi.org/10.1007/978-3-030-02810-7.

[112] S. Skoupas, G. Zaraphonitis, A. Papanikolaou, Parametric design and optimisa-
      tion of high-speed ro-ro passenger ships, Ocean Engineering 189 (2019) 106346.
      doi:https://doi.org/10.1016/j.oceaneng.2019.106346.
      URL   https://www.sciencedirect.com/science/article/pii/
      S0029801819305098

[113] M. Harenbrock, A. Korn, A. Weber, E. Hallbauer, Holistic design of innovative
      cathode air supply for automotive pem fuel cells, in: 21. Internationales Stuttgarter
      Symposium: Automobil-und Motorentechnik, Springer, 2021, pp. 121–136. doi:
      https://doi.org/10.1007/978-3-658-30995-4_25.

[114] C. Spiegel, PEM fuel cell modeling and simulation using MATLAB, Elsevier, 2011.
      doi:https://doi.org/10.1016/B978-0-12-374259-9.X5001-0.

[115] M. Yue, Z. Li, R. Roche, S. Jemei, N. Zerhouni, Degradation identification and prognostics of proton exchange membrane fuel cell under dynamic load, Control Engineering Practice 118 (2022) 104959. doi:https://doi.org/10.1016/j.conengprac.2021.104959.
URL https://www.sciencedirect.com/science/article/pii/S0967066121002367

[116] J. P. Sabawa, A. S. Bandarenka, Investigation of degradation mechanisms in pem fuel cells caused by low-temperature cycles, International Journal of Hydrogen Energy 46 (29) (2021) 15951–15964. doi:https://doi.org/10.1016/j.ijhydene.2021.02.088.
URL https://www.sciencedirect.com/science/article/pii/S0360319921005917

[117] L. Fan, J. Zhao, X. Luo, Z. Tu, Comparison of the performance and degradation mechanism of pemfc with pt/c and pt black catalyst, International Journal of Hydrogen Energy 47 (8) (2022) 5418–5428. doi:https://doi.org/10.1016/j.ijhydene.2021.11.135.
URL https://www.sciencedirect.com/science/article/pii/S0360319921045225

[118] M. Fang, X. Wan, J. Zou, Development of a fuel cell humidification system and dynamic control of humidity, International Journal of Energy Research 46 (15) (2022) 22421–22438. doi:https://doi.org/10.1002/er.8547.

[119] S. A. Nelson, Z. S. Filipi, D. N. Assanis, The use of neural nets for matching fixed or variable geometry compressors with diesel engines, Journal of Engineering for Gas Turbines and Power 125 (2) (2003) 572–579. doi:10.1115/1.1563239.
URL https://asmedigitalcollection.asme.org/gasturbinespower/article/125/2/572/447136/The-Use-of-Neural-Nets-for-Matching-Fixed-or

[120] J. Kang, F. Yan, P. Zhang, C. Du, A novel way to calculate energy efficiency for rechargeable batteries, Journal of Power Sources 206 (2012) 310–314. doi:https://doi.org/10.1016/j.jpowsour.2012.01.105.
URL https://www.sciencedirect.com/science/article/pii/S0378775312002066

[121] R. Vepa, Dynamic modeling, simulation and control of energy generation, Vol. 20, Springer, 2013.

[122] N. Xiros, Robust control of diesel ship propulsion, Springer Science & Business Media, 2002.

[123] T. I. Fossen, Guidance and control of ocean vehicles, John Wiley & Sons, Chichester, England, 1994.

[124] M. Blanke, Ship propulsion losses related to automatic steering and prime mover control, Technical University of Denmark, 1981.

[125] G. Iwanski, Ł. Bigorajski, W. Koczara, Speed control with incremental algorithm of minimum fuel consumption tracking for variable speed diesel generator, Energy Conversion and Management 161 (2018) 182–192. `doi:https://doi.org/10.1016/j.enconman.2018.01.053`.

[126] R. Izadi-Zamanabadi, M. Blanke, A ship propulsion system as a benchmark for fault-tolerant control, Control Engineering Practice 7 (2) (1999) 227–239. `doi:https://doi.org/10.1016/S0967-0661(98)00149-X`.

[127] J. Jeon, Hyeonmin Kim, Application of reference voltage control method of the generator using a neural network in variable speed synchronous generation system of dc distribution for ships, Journal of Marine Science and Engineering 8 (10) (2020) 802. `doi:https://doi.org/10.3390/jmse8100802`.

[128] K. E. Holmefjord, L. Husdal, M. de Jongh, S. Torben, Variable-speed engines on wind farm support vessels, Journal of Marine Science and Engineering 8 (3) (2020) 229. `doi:https://doi.org/10.3390/jmse8030229`.

[129] H. Farhadi Gharibeh, M. Farrokhifar, Online multi-level energy management strategy based on rule-based and optimization-based approaches for fuel cell hybrid electric vehicles, Applied Sciences 11 (9) (2021) 3849. `doi:https://doi.org/10.3390/app11093849`.

[130] D. Kler, A. Z. Hosseini, S. Varghese, C. Sun, G. Joos, A rule based ems for fast charging station with chil implementation, in: 2020 IEEE Energy Conversion Congress and Exposition (ECCE), IEEE, 2020, pp. 1319–1324. `doi:10.1109/ECCE44975.2020.9235380`.

[131] G. Ejebe, C. Jing, J. Waight, V. Vittal, G. Pieper, F. Jamshidian, P. Hirsch, D. Sobajic, Online dynamic security assessment in an ems, IEEE computer Applications in Power 11 (1) (1998) 43–47. `doi:10.1109/67.648499`.

[132] T. Capurso, M. Stefanizzi, M. Torresi, S. Camporeale, Perspective of the role of hydrogen in the 21st century energy transition, Energy Conversion and Management 251 (2022) 114898. `doi:10.1016/j.enconman.2021.114898`.
URL `https://linkinghub.elsevier.com/retrieve/pii/S0196890421010748`

[133] I. Glosten, Ferry fuel & propulsion feasibility study final report, Tech. rep., NYC Department of Transportation (2022).

[134] C. Verdouw, B. Tekinerdogan, A. Beulens, S. Wolfert, Digital twins in smart farming, Agricultural Systems 189 (2021) 103046. `doi:https://doi.org/10.1016/j.agsy.2020.103046`.
URL `https://www.sciencedirect.com/science/article/pii/S0308521X20309070`

[135] A. F. Molland, S. R. Turnock, D. A. Hudson, Ship Resistance and Propulsion: Practical Estimation of Ship Propulsive Power, 2nd Edition, Cambridge University Press, 2017. `doi:10.1017/9781316494196`.

[136] G. Saponaro, D. D'Amato, M. Stefanizzi, E. Franchini, O. Osen, A. Hasan, S. M. Camporeale, V. G. Monopoli, Fuel-cell hybrid power system preliminary design optimization for ferry application, IEEE Energy Conversion Conference and Expo (2023).

Publications

Journal paper:

- Cutrignelli F, Saponaro G, Stefanizzi M, Torresi M, Camporeale S.M. (2023). Study of the Effects of Regenerative Braking System on a Hybrid Diagnostic Train. Energies. 16(2):874. https://doi.org/10.3390/en16020874.

Conferences paper:

- Saponaro, G., Stefanizzi, M., D'Amato, D., Franchini, E., Fornarelli, F., Torresi, M., & Camporeale, S. M. (2022, December). Modeling and design optimization of a hybrid power generator for full-electric naval propulsion. In Journal of Physics: Conference Series (Vol. 2385, No. 1, p. 012087). IOP Publishing. DOI 10.1088/1742-6596/2385/1/012087.

- Saponaro, G., Stefanizzi, M., Franchini, E., Torresi, M., & Camporeale, S. (2023). Modeling and Design of a PEM Fuel Cell System for Ferry Applications (No. 2023-24-0145). SAE Technical Paper. DOI: https://doi.org/10.4271/2023-24-0145.

- Anaclerio, F., Saponaro, G., Mancaruso, E., Mazzarella, C., Fornarelli, F., Magi, V., & Camporeale, S.M. (2023). An Experimental Characterization of Gasoline/Ozone/Air Mixtures in Spark Ignition Engines (No. 2023-24-0039). SAE Technical Paper. DOI: https://doi.org/10.4271/2023-24-0039.

- Saponaro, G., D'Amato, D., Stefanizzi, M., Franchini, E., Osen, O., Hasan, A., Camporeale, S.M., & Monopoli, V.G. (2023). Fuel-Cell Hybrid Power System Preliminary Design Optimization for Fe0rry Application. 2023 IEEE Energy Conversion Congress and Exposition October 29-November 2, 2023 Nashville, Tennessee

Acknowledgments